Surface Decoration of Graphene with All-Inorganic Perovskite Nanocrystals

Nathan Denby Cottam

Thesis submitted to the University of Nottingham
for the degree of Doctor of Philosophy

October 2022

Abstract

Recent progress in the synthesis of high stability inorganic caesium lead halide perovskite nanocrystals (NCs) with unique optical and electronic properties has led to their increasing use in optoelectronic applications, such as broadband photodetectors. These NCs are of particular interest for the UV range as they have the potential to extend the wavelength range of photodetectors based on traditional materials. The physical properties of these nanostructures, such as the dynamics of charge carriers on different timescales and their effect on the optical recombination of carriers, are crucial for functional applications, but not yet fully understood.

This work reports on a slow (> 1 s) reversible quenching of the NC photoluminescence due to a light-induced Stark effect involving defects on the surface of the NCs and the redistribution of photoexcited carriers onto the NC surface.

We also demonstrate a defect-assisted high photoconductive gain (10^6 A/W) in the UV–Visible range for graphene transistors decorated with perovskite NCs, resulting from the charge transfer between the NCs and graphene. This is accompanied by a giant hysteresis of the graphene resistance that is strongly dependent on electrostatic gating and temperature. We summarise the properties of the perovskite/graphene transistor with 3 characteristic response times: optical (~ 10 s); electrical (~ 100 s); and magnetic (~ 500 s). Our data are well described by a phenomenological macroscopic 'two-capacitor' model of the charge transfer from bound states in the NCs into the graphene layer, providing a useful tool for the design of high-photoresponsivity perovskite/graphene transistors.

Finally, we investigate the prospects of using scalable additive manufacturing, specifically inkjet printing, of graphene (iGraphene) and other low-dimensional materials for development of fully printed optoelectronic devices compatible with a range of flexible and wearable substrates. We demonstrate a hybrid perovskite/iGraphene photodetector with responsivity ~ 15 A/W and use iGraphene as Ohmic contacts to other 2D materials.

I

Publications, conferences and talks

First author publications

- *Light-Induced Stark Effect and Reversible Photoluminescence Quenching in Inorganic Perovskite Nanocrystals*, **N. D. Cottam**, C. Zhang, J. L. Wildman, A. Patanè, L. Turyanska and O. Makarovsky, *Adv. Opt. Mater.*, 2021, **9**, 13, 2100104.

- *Defect-Assisted High Photoconductive UV–Visible Gain in Perovskite-Decorated Graphene Transistors*, **N. D. Cottam**, C. Zhang, L. Turyanska, L. Eaves, A. Patanè and O. Makarovsky, *ACS Appl. Electron. Mater.*, 2020, **2**, 1, 147–154.

- *Magnetic and electric field dependent charge transfer in perovskite/graphene field effect transistors*, **N. D. Cottam**, J. S. Austin, C. Zhang, A. Patanè, W. Escoffier, M. Goiran, M. Pierre, C. Coletti, V. Mišeikis, L. Turyanska and O. Makarovsky, manuscript submitted in August 2022.

- *Photosensitisation of Inkjet-Printed Graphene with Stable All-Inorganic Perovskite Nanocrystals*, J. S. Austin and **N. D. Cottam**, C. Zhang, F. Wang, J. H. Gosling, O. Makarovsky and L. Turyanska, manuscript in preparation to submit in 2022.

Named author publications

- *Inter-flake quantum transport of electrons and holes in inkjet-printed graphene devices*, F. Wang, J. H. Gosling, G. F. Trindade, G. Rance, O. Makarovsky, **N. D. Cottam**, Z. Kudrynskyi, A. Balanov, M. Greenaway, R. Wildman, R. Hague, L. Turyanska, C. Tuck and T. M. Fromhold, *Adv. Funct. Mater.*, 2021, **31**, 5, 2007478.

- *Universal mobility characteristics of graphene originating from charge scattering by ionised impurities*, J. H. Gosling, O. Makarovsky, F. Wang, **N. D Cottam**, C. J. Tuck, L. Turyanska and T. M. Fromhold, *Commun. Phys*, 2021, **4**, 30.

Conference presentations and seminars

- EP2DS conference, Tokyo (31 Oct - 5 Nov 2021). Online poster presentation. *Perovskite based heterostructures: from fundamental studies to optoelectronic applications*, **N. D. Cottam**, J. S. Austin, J. Wildman, F. Wang, C. Zhang, A. Patanè, C. Tuck, O. Makarovsky, and L. Turyanska.

- Beacon Propulsion Futures seminar, Nottingham (17 Feb 2021). Online oral presentation. *Novel Low-Dimensional Materials for UV Detection*, **N. D.**

Cottam, O. Makarovsky, Z. Kudrynskyi, A. Patané, L. Eaves, L. Turyanska, C. Zhang, Y. Huang, W. Luan, H. Cao, Z. Ma, L. Zhao and K. Wang.

- QD2020 conference, Munich (7-11 Dec 2020). Online poster presentation. *Perovskite based heterostructures for optoelectronic applications*, **N. D. Cottam**, C. Zhang, L. Turyanska, A. Patané, L. Eaves and O. Makarovsky.

- Defence Science and Technology Laboratory phase 2 meeting (Dec 2019). Oral presentation. *Blue perovskite/graphene hybrid photodetectors.*

- Graphene Week 2019 conference, Helsinki (23-27 Sep 2019). Oral presentation. *Hybrid 0D/2D Perovskite/Graphene UV-Vis Detector*, **N. D. Cottam**, C. Zhang, O. Makarovsky, L. Turyanska, A. Patanè and L. Eaves.

- Defence Science and Technology Laboratory phase 1 meeting (Jun 2019). Oral presentation. *0D/2D hybrid planar photodetectors.*

Acknowledgements

First and foremost, I give my utmost thanks to my supervisor, Dr. Oleg Makarovsky. His support, guidance and wealth of knowledge have been invaluable throughout my PhD and he has been the main driving force behind all of the successful research that I have carried out. I am truly grateful for the time and effort he has invested in developing my research skills and for the wisdom he has bestowed on me. He has not only been a great mentor, but a great friend, which has made working together these past few years an absolute pleasure.

I want to express my deepest gratitude to my co-supervisor, Dr. Lyudmila Turyanska, who gave me the opportunity to study for a PhD. I am extremely grateful for her faith in me and unwavering support throughout our time together, from my undergraduate studies to my PhD. Despite my stubbornness, I truly have appreciated her continuous help and feedback and have finally accepted that her way is (almost) always right.

My sincere thanks go to my co-supervisor, Prof. Amalia Patanè, for her continued support and guidance. Amalia's breadth of experience and knowledge has been very helpful to me throughout my studies. Her restless work ethic is an inspiration, and yet she would always find the time to help when asked.

I am grateful to Prof. Laurence Eaves for his useful insight and fruitful discussions on theoretical aspects of my work. His expertise never ceases to amaze me.

I am thankful for my friends, colleagues and visitors of the Wendy house: Dr. Jake D. G. Greener for his help and support in starting my PhD and unrivalled footy goalscoring abilities that have seen us win a few trophies over the years; Dr. Debarati Mazumder for her help and advice in the lab and her ever optimistic attitude; Dr. Zakhar R. Kudrynskyi for his help in device fabrication

and experimental techniques, his tireless efforts are appreciated; Dr. Davide Maria Di Paolo, Dr. Nilanthy Balakrishnan, Dr. Mahabub Alam Bhuiyan, Dr. Natalia Alexeeva, Dr. Evgenii Vdovin, Jas Chauhan, Viktoriya Kernytska, Shihong Xie, Anuhbab Dey, Jonathan Austin, Jonathan Gosling, Feiran Wang, Joni Wildman, James Felton and Mustaqeem Shiffa. I have enjoyed working with everyone and have many fond memories of our friendships and time spent together.

Finally, I would like to thank my friends and family. I raise a VK to my friends and housemates that I have shared my PhD life with; it has been a blast. My deepest thanks go to my parents for their continued support and encouragement. Without their sacrifices I would not be in the position I am today and for that I am eternally grateful. I would like to acknowledge my little brother for being awesome: never change. Lastly, I want to thank Annabel for her patience and support through my PhD, the coronavirus lockdowns and especially during my grumpy thesis writing phase.

Contents

1 Introduction

The ever-increasing demand for new and improved digital technology requires the development of faster and smaller devices and ultimately, the miniaturisation of transistors, but efforts to maintain Moore's law are faltering [1]. Traditional three-dimensional (3D) semiconductors based on silicon (Si) or germanium (Ge) are limited in their size scalability due to enhanced carrier scattering from surface imperfections [2]. Quantum well heterostructures consisting of III-V semiconductor compounds such as gallium arsenide (GaAs) sandwiched between aluminium gallium arsenide (AlGaAs) were amongst the first examples of two-dimensional (2D) quantum well (QW) systems [3]. However, performance of semiconductor QWs depends strongly on the thickness of the well and quality of interfaces, which is constrained by the growth techniques and lattice matching between the materials [4].

The successful isolation of graphene [5], the first 'true' 2D material, sent shock waves rippling through the scientific community and the race to discover similar materials began. This class of materials consists of layered crystal structures with strong in-plane covalent bonds and weak van der Waals (vdW) forces between layers. Since graphene, the library of similar atomically thin vdW materials has been expanded considerably [6] and now includes the wide-gap insulator hexagonal boron nitride (hBN), metal chalcogenides (e.g. InSe, In_2Se_3), transition metal dichalcogenides (TMDCs, e.g. MoS_2, WSe_2) and black phosphorus, to name a few [7]. The combination of these vdW materials in multi-layer heterostructures [8] and their compatibility with other low-dimensional materials such as quantum dots (QDs) [9] is of great interest for electronic and optoelectronic applications [10, 11].

In the past decade, halide perovskites have emerged as a new class of materials with exciting prospects for the optoelectronic community [12, 13]. Recent

synthesis of all-inorganic lead halide perovskite nanocrystals (NCs) [14] has attracted considerable attention due to their high optical quantum yield (QY), optical spectrum tunable from the visible (Vis) to the ultraviolet (UV) range, and enhanced stability compared to organic based NCs [15–18]. Integration of these NCs into novel 2D heterostructures based on graphene [19, 20] and other vdW materials [21] has enabled a number of advances in optoelectronics, ranging from improved solar cells [15, 22] and LEDs [23, 24] to ultrasensitive photodetectors [20].

In this thesis I present how graphene and other low dimensional materials, particularly perovskite NCs, can be combined for use in novel device applications and explore the fundamental charge transfer dynamics in these hybrid systems using a variety of perturbations and newly developed experimental techniques.

1.1   Thesis overview

Chapter 1 is the introduction and overview of the content of subsequent chapters contained in this thesis.

Chapter 2 provides an introduction and literature review on low-dimensional materials used in this project, particularly on graphene, how it is produced and its unique transport properties. This is followed by a literature review of perovskite NCs and their interesting optical properties, including temporal and temperature dependent photoluminescence and blinking. Finally, this chapter describes the functionalisation of graphene with perovskite NCs for use as UV-Vis photodetectors with an overview of photon detection and key parameters of photodetectors followed by a brief review of current photodetectors and their limitations.

Chapter 3 gives an overview of some of the key theory that is used and developed throughout the thesis. This includes characterisation of graphene properties through the parallel plate capacitor field effect model, a more advanced

two-capacitor model for describing functionalised graphene, and the classical and quantum Hall effect for direct measurement of graphene carrier concentration and mobility.

Chapter 4 describes the methods and experimental procedures involved in fabrication and characterisation of graphene-based field effect transistors functionalised with perovskite NCs. This includes details on the electrical, optical, optoelectronic and magneto-transport measurement techniques used throughout the studies within this thesis.

Chapter 5 reports on the novel transport and optoelectronic properties of hybrid planar graphene/perovskite NC photodetectors and their prospects for ultrasensitive detection in the UV-Vis range.

Chapter 6 presents an investigation into the properties of perovskite NCs under continuous optical excitation resulting in a quenching of the photoluminescence accompanied by a red shift in the emission energy due to a light-induced Stark effect.

Chapter 7 discusses a perovskite/graphene system subject to an externally applied magnetic field. The UV-specific (blue) perovskite NCs are also presented in this chapter.

Chapter 8 investigates the incorporation of inkjet-printed graphene technology into device applications for photodetection and electrical contacts, including a discussion of the transport and magneto-transport properties of graphene inks and their applicability for printable electronics and optoelectronics.

Chapter 9 concludes the thesis, providing an overview of the key findings followed by remarks on the future prospects for work beyond this thesis.

2 Low-dimensional materials for graphene-based functional applications

2.1 Introduction to low-dimensional materials

In low-dimensional materials the electronic state wavefunction is confined in one or more spatial dimensions. Dimensionality strongly affects electronic properties of a material, such as the energy band structure and density of states (DoS). The DoS is defined as the number of available states for a charge carrier per unit energy, $D(E)$. With increasing number of confined dimensions the density of states becomes more quantised: from a bulk (3D) system where continuous DoS is observed; to a quantum dot (0D), which has discrete allowed energy levels (**Figure 2.1**). In particular, for a conventional two-dimensional (2D) semiconductor with a band gap energy, E_g, the electrons and holes are confined in one dimension and the conduction and valence bands are described by a parabolic energy dispersion in the other 2 dimensions. The resulting expression for $D(E)$ is independent of energy and so the energy levels become quantised in a step-like function (**Figure 2.1**). These low-dimensional systems and the phenomena resulting from the quantised energy states have played a key role in the advancement of modern day electronic
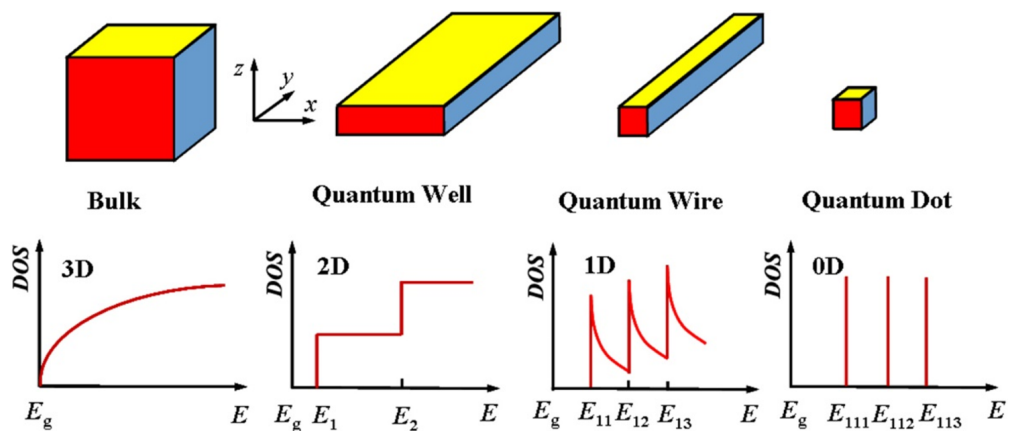
Figure 2.1. A diagram of the density of states for materials with different dimensionality. Figure reproduced from Ref. [25].

devices, including transistors [26, 27] and optoelectronics [28].

2.2 Graphene and other van der Waals materials

Of particular importance for the studies in this thesis are 2D materials with atomic-scale layer thickness, such as graphene, hexagonal boron nitride (hBN) and indium selenide (InSe) [10]. Typically, 2D materials are attained through mechanical exfoliation of the corresponding bulk material, in which the 2D layers are held together via weak van der Waals (vdW) forces. Interestingly, bespoke combinations of these single layer materials can be assembled by mechanical stamping to form multi-layer heterostructures with unique properties [10]. These heterostructures were used in devices from photovoltaics [29, 30] and light emitting diodes (LEDs) [31, 32] to resonant tunnelling transistors [33] and moiré superlattices [34, 35] and have facilitated observations of phenomena such as a giant quantum Hall plateau [36] and superconductivity [37].

Single layer graphene (SLG) is an allotrope of carbon in the form of a 2D, hexagonal (honeycomb) lattice of covalently bonded carbon atoms with carbon-carbon spacing of 0.142 nm (**Figure 2.2a**). Each carbon atom forms a strong, localised, in-plane σ-bond with its three nearest neighbours through sp^2 hybridisa-
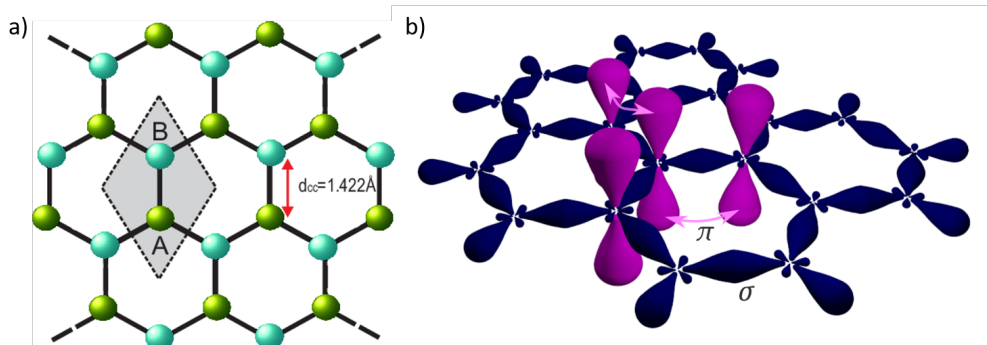
Figure 2.2. a) Schematic of the carbon honeycomb lattice with A and B interlinked sublattices and interatomic spacing $dcc = 0.142nm$. Figure reproduced from Ref. [38]. **b)** Illustration of the in-plane σ and out-of-plane π bonds in graphene that give rise to its unique properties. Figure reproduced from Ref. [39].

tion. However, this means that every carbon atom has one un-hybridised electron, which forms a delocalised π-bond oriented out of the plane of the graphene sheet (**Figure 2.2b**). These electrons form the π-bands above and below the sheet.

The conduction and valence bands of graphene meet in six single points (Dirac points) at the corners of the Brillouin zone **Figure 2.3a**. The peculiar band structure of graphene is different from any other material and makes it a zero band gap semiconductor. This unique band structure gives rise to many interesting properties in graphene such as ambipolar electric field effect [40], charge carrier tunability [41] and high carrier mobility [42].

The charge carriers in graphene mimic relativistic particles, namely massless Dirac fermions, as they are described by the Dirac equation [44]. Considering that electrons in graphene can hop to the nearest atoms, the tight-binding approximation predicts that the charge carriers follow a linear energy dispersion relation close to the Fermi level (**Figure 2.3a**):

$$E(p) = \pm v_F |p|, \tag{2.1}$$

where p is the electron momentum relative to the Dirac point and the Fermi
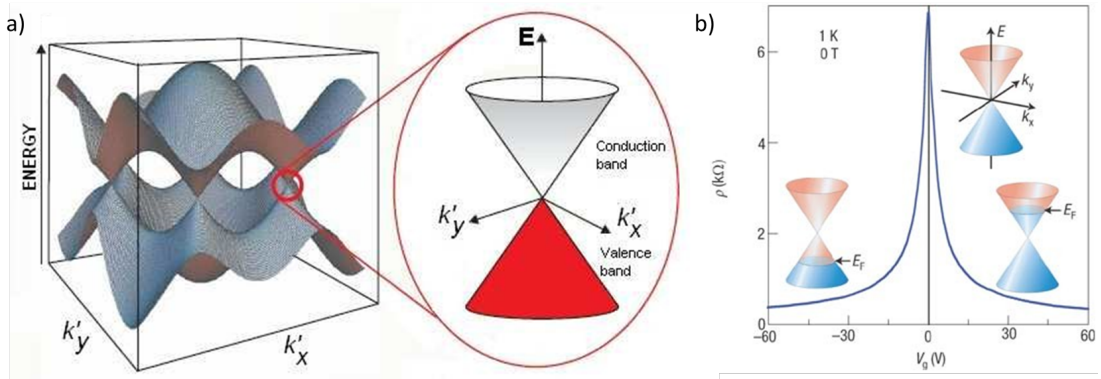
Figure 2.3. **a)** The electronic energy dispersion in the honeycomb lattice and zoomed in region showing the linear energy band structure close to the Dirac points. Figure reproduced from Ref. [38]. **b)** The resistivity of graphene as a function of gate voltage and corresponding position of the Fermi energy. Figure reproduced from Ref. [43].

velocity, $v_F \sim 10^6$ m/s ($0.003c$, where c is the speed of light in vacuum). The $\pm$ sign refers to the conduction band (positive energy states) and valence band (negative energy states), respectively.

2.3   Types of graphene

The properties of graphene can vary tremendously depending on the growth technique and substrate used. The main methods of producing graphene are mechanical exfoliation from bulk graphite [5, 45], thermal decomposition of silicon carbide (SiC) [46–48] and growth by either chemical vapour deposition (CVD) [49–51] or molecular beam epitaxy (MBE) [52, 53]. More recently, liquid exfoliation methods were developed to adapt graphene for inkjet printing [54–56].

Graphene was first mechanically isolated in 2004 using the 'Scotch tape' method [5], whereby a single layer of graphene is cleaved from a bulk graphite crystal using Scotch tape. This exfoliation technique yields flakes with the highest mobility ($\mu > 200,000$ cm^2/Vs [45, 57]), as the produced single layer graphene is not exposed to chemical processing or complex transfer processes. However, graphene flake size is relatively small ($< 10 \times 10$ μm^2 [5]) and requires bespoke device fabrication (**Figure 2.4a**), as electrical contacts must be custom made to suit each flake, which is a time consuming process. More advanced architectures produced on silicon/silicon dioxide (Si/SiO$_2$) substrates include additional layers of hexagonal boron nitride (hBN) above and below the graphene. The extra layers of hBN, which are relatively free of dangling bonds and charge traps, emulate free-standing graphene by isolating it from ionised defects in the SiO$_2$ substrate and from surface contamination [58]. Moreover, the atomically smooth surface of hBN suppresses rippling and mechanical corrugation of the graphene, which otherwise can limit carrier mobility through scattering [59, 60].

SiC growth method produces a more robust form of graphene, which is
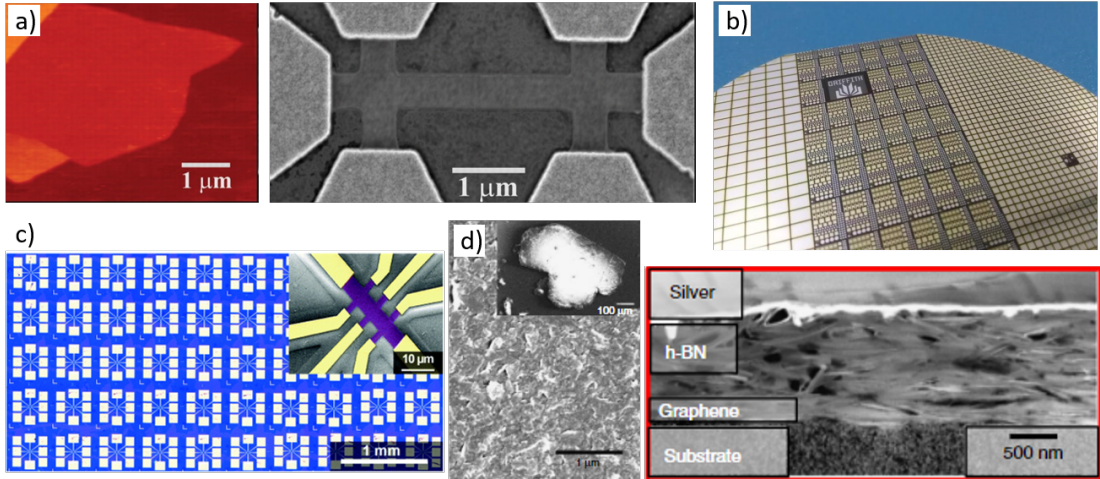
Figure 2.4. a) Left: atomic force microscope (AFM) image of mechanically exfoliated single-layer graphene. Colours: dark brown, SiO_2 surface; brown-red (central area), 0.8 nm height; yellow-brown (bottom left), 1.2 nm; orange (top left), 2.5 nm. Right: scanning electron microscope (SEM) image of an experimental device prepared from mechanically exfoliated graphene. Figures reproduced from Ref. [5]. **b)** A SiC wafer with fabricated Shottky diodes. Figure reproduced from Ref. [67]. **c)** Optical image of 50 CVD graphene Hall bars on Si/SiO_2. Inset: false-colour SEM image of a single Hall bar. Figure reproduced from Ref. [68]. **d)** Left: SEM images of LPE graphene flakes (~ 200 nm) and (inset) the starting graphite (~ 400 μm). Right: high angle annular dark-field-scanning transmission electron microscopy (HAADF-STEM) cross-sectional view of a fully inkjet-printed silver/hBN/graphene FET using LPE-formulated hBN and graphene inks. Figures reproduced from Ref. [69].

bonded to a crystalline structure consisting of silicon and carbon atoms only. The graphene layer is formed through thermal decomposition of the SiC crystal at high temperatures ($T > 800$ °C) in ultrahigh vacuum [46, 48]. Since the vapour pressure of carbon is negligible compared to silicon the high temperature causes desorption of silicon atoms from the surface leaving behind carbon atoms, which rearrange to form graphene layers [61]. This method can produce wafer-scale SLG (**Figure 2.4b**) with homogenous monolayer domains with sizes $> 50 \times 50$ μm^2 [62]. This type of graphene is typically heavy n-type ($n > 10^{12}$ cm^{-2}) and is difficult to gate as it requires top gating, which is a bespoke and time consuming fabrication process. Furthermore, the room temperature carrier mobility is relatively low in SiC based graphene, $\mu \sim 10^3$ cm^2/Vs [63, 64]. SiC-SLG is currently used for the most accurate quantum Hall resistance standard with an accuracy of 10^{-9} [65, 66].

Commercially available SLG is typically CVD grown [70, 71]. The layers are grown on a metal foil, such as copper or copper-nickel alloy [50] using a thermally decomposed hydrocarbon gas source at high temperatures ($T \sim 1000\,°\text{C}$ [49]). The foil is etched away after growth to transfer the graphene onto a dielectric substrate e.g. Si/SiO$_2$ [51]. The processes of wet etching and transfer require the use of polymethyl methacrylate (PMMA) and other substances that can leave residues on the graphene surface. CVD grown SLG is typically p-type and has lower mobility ($\mu \sim 10^3 - 10^4$ cm^2/Vs) than exfoliated graphene. On the other hand, this method of graphene growth can be scaled to wafer-size substrates (**Figure 2.4c**) and CVD technology is readily available in most commercial semiconductor laboratories.

MBE growth is a promising, and relatively new, route to large scale graphene production. This growth method typically uses hBN or sapphire substrates and requires high temperatures ($T \sim 1000 - 1500\,°\text{C}$ [52]). Since the graphene can be grown directly on a dielectric material in an ultra-clean MBE environment and it doesn't require any transfer processes, it is the most pure type of graphene ($n < 10^{10}$ cm^{-2}) besides mechanical exfoliation. However, growth is currently limited by the available hBN flake (substrate) size ($20 - 100\,\mu$m), the domain size is relatively small ($\sim 20\,\mu$m) and growth times can be very long (~ 4 h) [53].

Upscaling of the processing of devices has remained a key limitation in reaching the true commercial potential of graphene. Although CVD growth has demonstrated large-area graphene layers, their electronic properties are inferior to mechanically exfoliated SLG [72]. Liquid phase exfoliation (LPE) methods are also considered as an alternative route to large scale graphene fabrication. LPE is most commonly achieved through sonication [73], high-shear mixing [74, 75] or more recently via a microfluidization technique [76]. Whilst promising for commercialisation, the control over flake size and thickness produced using these methods is currently not ideal. Despite this, LPE graphene has attracted significant interest

as it allows integration of 2D materials with advanced manufacturing technologies (e.g. inkjet printing) for scalable device fabrication (**Figure 2.4d**). Commercial graphene inks (iGraphene) are already available and typically consist of lots of small ($\sim 50 \times 50$ nm^2 average size) flakes produced by LPE of graphite [77].

Whilst graphene of all forms boasts strong electrical properties, it is fundamentally limited by its intrinsic gapless nature. To truly accomplish the full potential of graphene in functional devices it must be combined with functional materials, such as other 2D vdW materials, QDs or NCs. An example of this is a 2D/2D InSe/SLG broad-band photodetector [78] formed through the mechanical exfoliation and combination of SLG and InSe 2D layers. It was also shown that graphene functionalised with lead sulphide (PbS) quantum dots could exploit the optical absorption capabilities of PbS along with the electrical properties of graphene to make a near infrared photodetector [79]. More recently, perovskite NCs were proposed for similar UV-Vis photodetector capabilities [20].

2.4 Perovskite nanocrystals and their optical properties

2.4.1 Overview of perovskite nanocrystals

Halide perovskites are compounds that have the general chemical formula ABX$_3$, where A denotes an organic (e.g. methylammonium (MA) or formamidinium (FA)) or inorganic (e.g. caesium or rubidium) cation, B is a divalent metal (e.g. lead or tin) cation and X is a monovalent halide (e.g. iodine, bromine, chlorine or a mixture) anion. Many studies have been carried out on organic-inorganic lead halide perovskite solar cells since their first demonstration in 2009 [80], with most studies focusing on MAPbI$_3$ [80–83] and FAPbI$_3$ [83–86]. A certified power conversion efficiency of $>25\%$ [84] was achieved and is already at a level comparable to silicon solar cells [87]. However, organic-inorganic perovskites are susceptible to degradation in ambient conditions such as moisture, heat, oxygen and light [88–
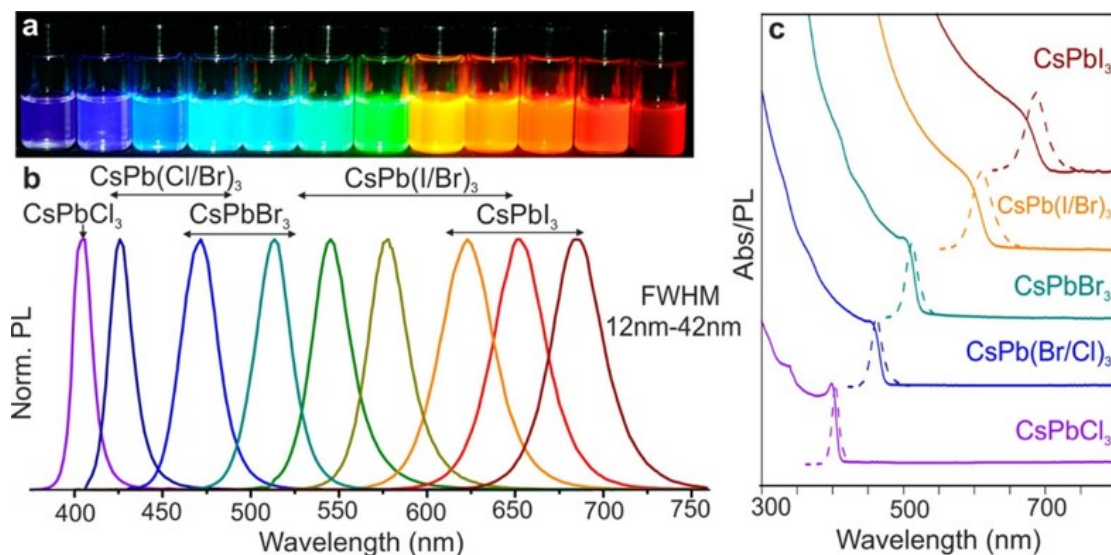
Figure 2.5. a) Optical image of colloidal CsPbX$_3$ NCs (X = Cl, Br, I) in toluene under UV lamp excitation (λ_{ex} = 365 nm). **b)** Representative PL spectra for each NC solution (λ_{ex} = 400 nm for all except 350 nm for CsPbCl$_3$). **c)** Typical optical absorption and PL spectra for these perovskite NCs. Figure reproduced from Ref. [14].

91]. Replacing the organic (MA or FA) molecule with an inorganic cation such as caesium (i.e. CsPbX$_3$) has led to significantly improved environmental stability [92] whilst maintaining reasonably high efficiency ($\sim$18% [93]).

First synthesised in 2015 [14], colloidal all-inorganic halide perovskite NCs have motivated a significant number of studies, as they offer several advantages over perovskite films, including higher thermal stability and higher resistance to photobleaching [94]. A solution synthesis technique allows for fast, controlled growth of the NCs using a mixture of oleylamine (OLA) and oleic acid (OA) as passivating ligands to enhance colloidal stability. In solution synthesis, the majority of the NC growth occurs in the first few seconds and the size of the NCs is controlled in the range $4 - 15$ nm by the reaction temperature [14].

The high temperature ($T = 140 - 200$ °C) reaction is used to form cubic NCs crystallised in the α-phase (cubic-phase). The band edge optical emission of these NCs can be tuned by the halogen content in the wavelength range from 400 nm for CsPbCl$_3$ to 700 nm for CsPbI$_3$ (**Figure 2.5a-c** [14]). In contrast to

colloidal QDs [95], the wavelength of PL emission, λ_{PL}, is not very sensitive to the NC size as it is typically larger than the exciton Bohr radius ($r_B = 3.6$ nm for CsPbBr$_3$ and $r_B = 6$ nm for CsPbI$_3$) [14, 24]. The large exciton binding energy of the perovskite NCs ($E_B > 50$ meV) [96, 97] and linear dependence of the PL emission intensity on the excitation power suggest an excitonic emission even at room temperature. The mixing of halides (e.g. I with Br) is used to tune the PL wavelength between the values observed for the individual halide NCs and a whole gamut of colours across the UV-Vis spectrum can be achieved. Furthermore, these NCs offer strong UV-Vis absorption, a narrow PL linewidth and high quantum yield (QY) ($>90\%$) [14, 24, 94, 98]. Thus, inorganic halide perovskite NCs have a considerable potential for applications in optoelectronics, including solar cells [15, 99], LEDs [24, 100], lasers [101] and photodetectors [20, 102–104].

However, as with perovskite films, the long-term stability of the NCs and chemical decomposition under exposure to harsh environmental conditions is still an issue that needs addressing. The stability of the NCs is strongly dependent on the strength of binding, surface density and stability of the capping ligands. The most common ligands, OA and OLA, fail to prevent degradation of the NCs over time. However, the more recent incorporation of bidentate ligands such as didodecyldimethylammonium bromide (DDAB) and iminodibenzoic acid (IDA) have been shown to improve the NC stability due to a stronger steric effect [24, 105]. Furthermore, the ligands are critical in determining optical properties of the NCs as unpassivated bonds on the surface of the NC can act as non-radiative recombination centres for charge carriers, thus reducing the QY. Hence, halogen containing ligands are currently being investigated, as halogens can be embedded into the NC lattice, enhancing defect passivation and improving stability [105].

2.4.2 Temporal and temperature dependent optical properties

Optical studies are widely used for characterisation of $CsPbX_3$ perovskite NCs. These include time resolved PL (TRPL), which uses a short pulse of light to excite the NCs and then measure the decay of the emission signal and thus the lifetime of the excited states. TRPL lifetimes for $CsPbX_3$ NCs are typically of the order of a few nanoseconds (**Figure 2.6a**) [14, 106]. There have also been a lot of long term (days to months) stability studies, assessing PL properties under different environmental storage conditions as an indicator of the shelf life of the perovskite NCs [24].

Temperature dependent PL phenomena is also commonly studied and all-inorganic perovskite $CsPbX_3$ NCs exhibit an unusual, strong blue shift in band gap and PL emission with increasing temperature (**Figure 2.6b**) [108, 109]. Typically in semiconductors an increasing temperature causes a lattice dilation that reduces the energy gap between the valence band maxima (VBM) and conduction band minima (CBM), and a red shift in PL is observed. However, in lead halide perovskites an increase in the lattice dilation causes the energy of the VBM to
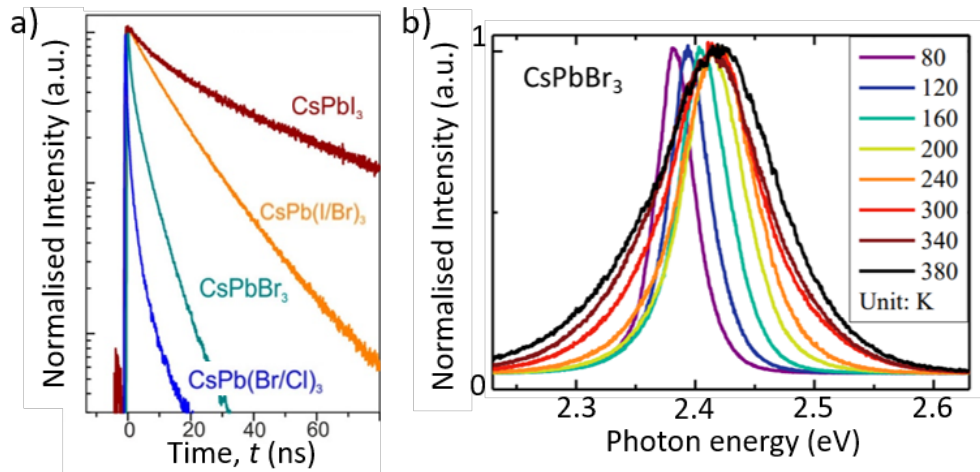
Figure 2.6. **a)** Time-resolved PL decays for different all-inorganic perovskite NCs. Figure reproduced from Ref. [14]. **b)** Temperature-dependent PL spectrum of $CsPbBr_3$ NCs normalised to clarify the peak shift. Figure reproduced from Ref. [107].

13

decrease whilst the CBM slightly increases, meaning a blue shift in the band gap with increasing temperature [109–111]. There have also been reports of instability under illumination in mixed halide perovskites NCs due to ion migration, which is the reversible light-induced segregation of iodine- and bromine-rich domains [112, 113]. In this case, a reduction in the initial PL peak over a time scale of a few minutes to hours was reported along with the growth of a second, shifted, PL peak. However, the mechanism involved is still under debate and it has been reported as both a blue shift [112] and a red shift [113]. Furthermore, this decrease of PL intensity is reversible only in bulk films and not in individual NCs [112] as it relies on halide ion migration to adjacent regions due to Coulomb repulsion when illuminated and then returning via concentration gradient diffusion in the dark [114]. Whilst there is a lot of literature on the stability (or instability) of perovskite NCs, the underlying mechanisms to explain the observed time dependent PL measurements are yet to be fully understood.

2.4.3   Photoluminescence blinking phenomena

Recent studies revealed a similarity in the properties of perovskite NCs and other semiconductor QDs, such as a NC size-dependent energy gap and room temperature PL blinking (or PL intermittency) in single $CsPbX_3$ (X = I, Br) NCs [115–117]. For a $CsPbI_3$ NC (**Figure 2.7a**) this was found to be accompanied by a decrease in PL intensity over time (**Figure 2.7b**) [115]. Blinking, or intermittency, is a phenomenon of a QD randomly switching between radiative and non-radiative states under constant excitation and is understood to be a result of light-induced charging and discharging of a NC [118, 119]. The charging of the NC causes further absorbed photons to trigger non-radiative Auger recombination during which the exciton energy is acquired by an extra electron or hole. The rate of Auger recombination is orders of magnitude faster than radiative recombination and so when the NC is in this state its PL emission is quenched.
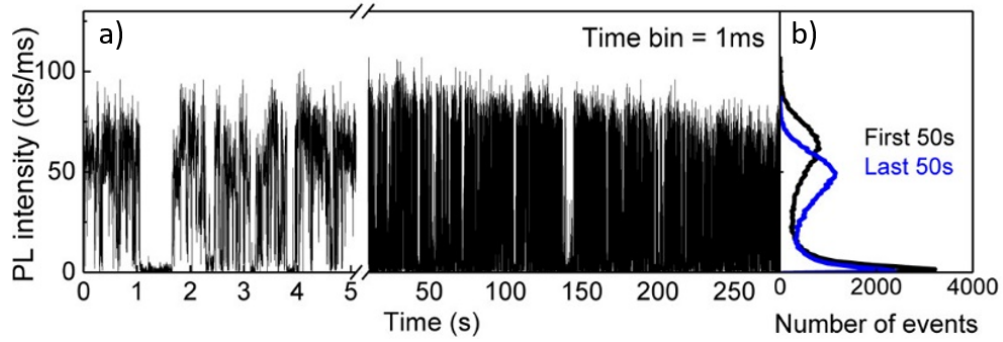
Figure 2.7. a) PL blinking observed in the temporal dependence of PL intensity recorded for a single CsPbI$_3$ NC with a 1 ms time bin ($\lambda_{ex} = 488$ nm excitation, $P = 7.9$ W/cm^2) and **b)** the corresponding probability histogram for the first 50 s (black curve) and the last 50 s (blue curve). Figures reproduced from Ref. [115].

Despite the similarities to traditional QDs, the behaviour of perovskite NCs in optoelectronic devices can be quite different [120]. This may partially arise from surface defects, typically halide vacancies, which play an important role in defining the electronic and optical properties of the NCs. Perovskite NCs are known to be highly defect tolerant due to the anti-bonding character of the conduction and valence bands [111, 121, 122], meaning that they can be optically active even with a high density of defects.

2.5 Functionalised graphene photodetectors

Surface functionalisation of graphene with photosensitive perovskite NCs is proposed as a route to engineering high sensitivity UV-Vis photodetectors [20]. Fundamentally, photon detection occurs when an optical signal incident on a material is converted into an electrical signal. Maximising the capability of a photodetector requires optimisation of the device architecture, materials and interfaces. The performance characteristics of a photodetector are typically defined by:

(i) The spectral response range of the detector, which is determined by the absorption spectra of the semiconductor materials used. For example, commercial silicon-based detectors work well in the range $\lambda = 400 - 1100$ nm, whereas stan-

dard InGaAs detectors work well at $\lambda = 900 - 1700$ nm [123].

(ii) The sensitivity of the detector, characterised by the photoresponsivity, R, which is defined as the ratio of the photocurrent produced under illumination, I_{ph}, to the power of the light incident on the detector, $P_{incident}$,

$$R = \frac{I_{ph}}{P_{incident}}.$$ (2.2)

The minimum optical power detectable, or maximum sensitivity of the detector, is referred to as the noise equivalent power (NEP) and is defined as the optical power at which the signal-to-noise ratio is unity.

(iii) The response time of the device, τ, is the time taken for the electrical signal to go from the OFF (dark) state to a stable ON (under illumination) state. Typically, response time is calculated as the time constant of an exponential fit of the photocurrent immediately after exposure to light for the 'rise' time and after the exposure is ceased for the 'fall' time. Another common method of calculating response time is the time taken for the photocurrent signal to rise from 10% to 90% or fall from 90% to 10% of the maximum value.

(iv) Specific detectivity, D^*, is another important parameter for photodetectors as it enables a direct comparison of photodetector devices with different configurations and geometries. Detectivity is typically expressed in units of cmHz$^{0.5}$W^{-1}, also known as Jones, and is given by,

$$D^* = \frac{\sqrt{A\Delta f}}{\text{NEP}},$$ (2.3)

where A is the active area of the photodetector and $\Delta f = 1/2\pi\tau$ is the frequency bandwidth.

There is a strong demand for photodetectors operational at a pre-defined spectral range, with high photoresponsivity and a fast response time for applications in imaging [124, 125], security [126] and advanced communications [102].

2.5.1 Advantages of low-dimensional materials for photodetectors

One of the most popular photodetectors is the *pn*-junction, which comprises of bulk $n-$ and $p-$type materials and utilises a built-in electric field at the *pn*-interface to separate photo-generated electron-hole pairs formed in the depletion region. Typically, detectors of this type have fast response times ($\tau < 1$ ms), but the responsivity is fundamentally limited to $R < 1$ A/W at maximum efficiency as only a single electron-hole pair can be created for each incident photon in an ideal *pn*-junction photon detector [127, 128].
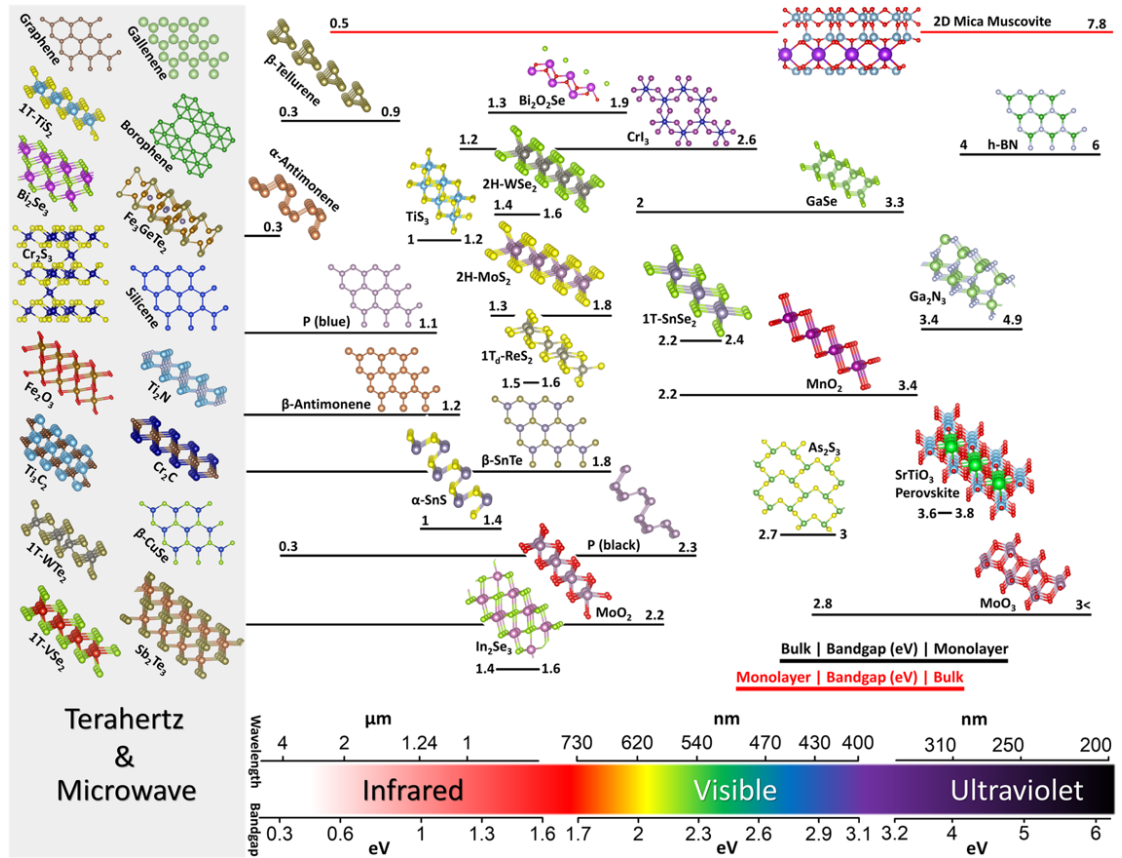
Figure 2.8. 2D materials offer a wide range of possible band gaps depending on their crystal structure. Arrangement is in accordance with their band gap (E_g), guided by the bottom wavelength/E_g scale, whereas the bar beneath each structure indicates E_g range from bulk to monolayer. Typically, the bulk E_g is smaller than that of its monolayer (black bars), but there are exceptions (red bars). 2D materials on the far left, indicated by a grey box, are zero or near-zero E_g, metallic, or semi-metallic. Figure reproduced from Ref. [129].

Conventional detectors using bulk semiconductor materials, such as Si and InGaAs, are well established and the technology and manufacture of these detectors is well advanced [130–133]. Detectors based on low-dimensional materials, although a relatively new technology, have several advantages. The first of which is that the sensitivity of low-dimensional materials can be tuned over a wide range of the electromagnetic spectrum by changing the band gap energy (E_g) [129] (**Figure 2.8**). In 2D semiconductors, such as transition metal dichalcogenides (TMDCs), E_g varies from ~ 1 eV to > 2.5 eV, corresponding to near infrared (NIR) and visible photodetection, respectively [134] and the E_g can be tuned further by the number of atomic layers e.g. InSe can be tuned in the range $1.3 - 1.9$ eV [135]. This is also true for QDs, where the band gap is strongly dependent on the NC size due to quantum confinement and can also be controlled by chemical composition [95, 136]. The second advantage of low-dimensional materials is that they can be readily combined in hybrid structures or vdW heterostructures, without the restrictions imposed by lattice matching of bulk materials [8]. Thus, allowing the fabrication of multi-layer vdW systems that combine the superior transport and optical properties of different individual components. Thirdly, low dimensional materials exhibit strong light-matter interactions [30]. For three single-layer semiconducting TMDCs this was found to be due to the combined density of states resulting in strong absorption peaks in the visible range [30]. Perovskite NCs also display high intrinsic absorption coefficients (of the order 10^5 cm^{-1} for CsPbBr$_3$ [137]).

2.5.2 Graphene-based photon detection

Single layer graphene (SLG) can absorb light across a wide range of wavelengths from UV to THz [138, 139] with ultrafast response time (~ 1 ps) [140], but it has very low absorption ($\sim 2\%$). Due to the extremely high sensitivity of graphene to external charges it is an ideal candidate for hybrid devices combining

Material	Responsivity [A W^{-1}]	Gain	Response time [s]	Detection range [µm]
Graphene	5×10^{-4}	–	$\approx 2.5 \times 10^{-11}$	1.55
Graphene/QDs (PbS)	10^7	10^8	10^{-2}	Visible–NIR
Graphene/QDs (HgSe)	10^7	–	0.26	NIR
Graphene/MoS$_2$	$10^{10c)}$	10^{10}	1	Visible
Graphene/Ti$_2$O$_5$/graphene	>1	–	–	NIR–MIR
Graphene/MoS$_2$	1.2×10^7	$\approx 10^8$	–	Visible
Perovskite/graphene	180	500	$\approx 10^{-1}$	Visible
Graphene/carbon nanotube	>100	10^5	10^{-4}	Visible–NIR
Graphene/SiO$_2$/light doped Si	1000	–	4×10^{-7}	0.514

Figure 2.9. Table showing figures of merit for some example graphene-based photodetectors. Figure reproduced from Ref. [152].

it with an adjacent layer of an optically active 0D, 2D, or 3D material (**Figure 2.9**) [141–144]. For example, a record high photoresponsivity (R up to 10^9 A/W) has been achieved by depositing photoresponsive 0D II–VI or IV–VI QDs (CdSe, CdS, PbS, etc.) on the surface of single layer graphene (SLG) [79, 144–146]. The high photoresponsivity is enabled by a strong photoconductive gain effect due to the relatively long lifetime of trapped photoexcited charges in the quantum dot, τ_{trap}, and the injection of carriers into graphene with a short transit time $\tau_{transit}$. The responsivity is proportional to the ratio of these times,

$$R = \frac{\tau_{trap}}{\tau_{transit}} \cdot \frac{\alpha e}{h\nu}, \tag{2.4}$$

where α is the absorbance, e is the electron charge, h is Planck's constant and ν is the frequency of light [79]. For a microscopic graphene device, with mobility ~ 1000 cm^2/Vs, a typical transit time is on the order $\tau_{transit} \sim 1$ ns and PbS QD trapping time is $\tau_{trap} \sim 1$ s, which gives a gain of 10^9 [79]. More recently, organic [147] and inorganic [20] perovskite NCs with high optical quantum yield (QY) have been used in combination with graphene [103, 148–150] to utilise this photoconductive gain effect, and have achieved responsivity of up to $\sim 10^8$ A/W [151]. Perovskite NCs were also proposed for extending the photoresponsivity of graphene devices into the UV region [20, 103].

Harnessing the potential of the perovskite NC/graphene heterostructures requires development of fundamental understanding of the charge transfer processes that occur at their interface. Despite a growing number of experimental reports on the application of perovskite NC/graphene in optoelectronic devices [20, 103, 147], the understanding and control of the charge transfer in these hybrid devices remains to be achieved [19].

2.5.3   UV detection and current limitations

UV light refers to electromagnetic radiation in the spectral range from 10 nm to 400 nm and accounts for just over 8% of the total solar radiation [153, 154]. UV radiation is split into the following three main sub-bands: UVA ($320 - 400$ nm), UVB ($280 - 320$ nm) and UVC ($10 - 280$ nm) [155, 156]. Most of the UV radiation from sunlight with a wavelength, $\lambda < 280$ nm does not reach the surface of the Earth as it is absorbed by the atmosphere [155]. For this reason, the spectral range from 200 nm to 280 nm is typically referred to as the solar-blind region [153], meaning that there is no interference from the Sun's radiation. UV radiation is utilised in various industries for its high ionisation properties in procedures such as water purification [157] and surface cleansing [158]. UV photodetectors, particularly in the solar blind regime, are of great interest for applications in flame detection, chemical analysis, defence missile warning systems and space-to-space communication [155, 159, 160].

Currently, UV photon detectors are mainly based on UV-enhanced silicon, silicon carbide (SiC) and III-nitride semiconductors (e.g. GaN) [161]. These types of detector typically have a very fast response time (few μs), however, they suffer from low responsivity (< 1 A/W). For example, current commercially available UV-enhanced silicon detectors have a fast response time of $\sim 1 - 3$ μs but a low responsivity of only $0.1 - 0.5$ A/W [162, 163]. Furthermore, any light of higher wavelengths is still detected in these devices and indistinguishable from

the UV response. Consequently, a filter (e.g. solar rejection filter) is required to block light with a wavelength > 400 nm for any UV-specific applications. SiC detectors offer a UV specific alternative, as their intrinsic spectral response is from $210 - 380$ nm, but they also have low responsivity (< 0.2 A/W) [164]. The III-nitride (In, Al, Ga)N direct band gap semiconductors are visible-blind materials. For example, GaN has an absorption edge at 365 nm and AlN at 200 nm [165] and the detection edge can be tuned by varying the molar fraction of aluminium. However, these detectors also have low responsivity (typically < 1 A/W) and require energy intensive growth processes (e.g. MBE), as well as substrate lattice matching [166].

UV sensitive devices with enhanced operational parameters can be enabled by exploring novel device concepts designed for greater sensitivity, faster response times, flexibility and self-powered detection. One of the promising routes to produce more sensitive devices is by the surface functionalisation of graphene with highly optically active materials such as perovskite NCs (e.g. $CsPbCl_3$) [20]. As discussed in **Section 2.4.1** the absorption band-edge can be tuned close to the UV via the halide content of the NCs down to chlorine. Thus, this graphene/$CsPbCl_3$ NC hybrid device is UV-specific and exhibits over 10^6 times higher responsivity ($R > 10^6$ A/W) than silicon with reasonably fast response times of 0.3 s [20].

The substrate used for photon detectors becomes very important in the UV range as it can also impact the photoresponsivity of a device, particularly in low-dimensional detectors. For planar graphene transistors on Si/SiO_2 a photogating effect was observed [167], whereby electron-hole pairs are separated by the electric field between graphene and Si and the accumulation of holes at the Si/SiO_2 interface results in an additional gating of the graphene. This effect corresponded to a parasitic responsivity of ~ 4 A/W at $\lambda_{ex} = 1064$ nm, which increased dramatically to ~ 500 A/W at $\lambda_{ex} = 450$ nm, with a cut-off wavelength ~ 1100 nm corresponding to the band gap of Si [167]. Furthermore, approaching higher pho-

ton energies (lower wavelengths) many materials tend to become more optically active, especially in the UV regime. For example, SiO_2 is shown to contain many defects [168] and UV irradiation can cause permanent bleaching or partial/fully reversible changes in Si/SiO_2-based graphene FETs [169, 170]. However, mechanisms for the bleaching effect are still unclear. These effects may restrict the use of conventional substrates, such as Si/SiO_2 in UV (particularly solar-blind UV) graphene detectors.

3 Modelling of carrier transport in graphene and functionalised graphene layers

This section outlines some of the key theory and charge transport models that we used to describe the properties of graphene and functionalised graphene devices. This includes an overview of field effect mobility and carrier concentration calculations using the parallel plate capacitor model, followed by a two-capacitor model that we developed to describe graphene functionalised with perovskite NCs. The Hall effect in graphene, Hall mobility and concentration are also presented.

3.1 Single parallel plate capacitor (1C) model

A field effect transistor can be described using a parallel plate capacitor (1C) model [45]. For a typical graphene FET, this model considers two parallel plates: the conductive channel (SLG) and the gate (Si), which are separated by a dielectric (SiO_2) and both plates are treated as metallic. To adhere to the conservation of charge in the parallel plate capacitor, any electric charge induced by an applied voltage in the silicon gate, Q_{gate}, must be equally compensated by an opposite charge in the top SLG plate, Q_{SLG}, such that

$$Q_{gate} = -Q_{SLG}. \tag{3.1}$$

The capacitance C of the two flat, parallel plates of area A and dielectric separation thickness d (**Figure 3.1a**) is defined as

$$C = \epsilon\epsilon_0 \frac{A}{d}. \tag{3.2}$$

Here $\epsilon_0 = 8.85 \times 10^{-12}$ F/m is the permittivity of free space and ϵ is the relative permittivity of the dielectric material, which is 3.9 for SiO_2. The definition of
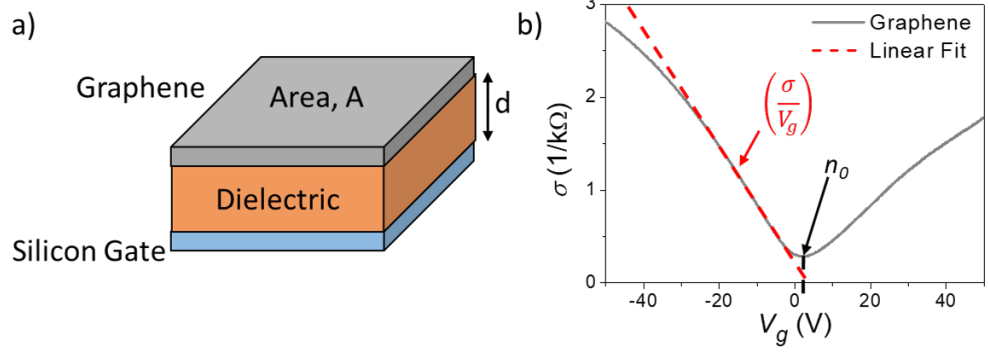
Figure 3.1. a) A layer structure diagram showing a parallel plate capacitor used in the model for calculating carrier mobility. **b)** Example graph of the conductivity, σ, of a pristine graphene FET plotted against the applied gate voltage, V_g, to illustrate how the carrier concentration and carrier mobility are calculated. The position of the Dirac point at $V_g = 0$ V is denoted by n_0.

capacitance is,

$$C = \frac{Q}{V},\tag{3.3}$$

where V is the voltage across the capacitor and Q is the total charge, which can be written as the product of the charge carrier density (per unit area) n, the electron (or hole) charge q and the area, such that

$$Q = qnA.\tag{3.4}$$

Substituting **Equation 3.4** into **Equation 3.3**, then equating this capacitance to **Equation 3.2** and re-arranging, gives the number density of charge carriers at an applied gate voltage $V = V_g$ for a FET,

$$n = \frac{\epsilon\epsilon_0}{qd}V_g.\tag{3.5}$$

For SLG, the minimum in the conductivity curve gives the 2D density of charge carriers, n_0, which is equivalent to the doping level at $V_g = 0$ (**Figure 3.1b**). Thus,

$$n(V_g) = n_0 + \frac{\epsilon\epsilon_0}{qd}V_g.\tag{3.6}$$

For a semiconductor with charge carrier density n the conductivity can be written as

$$\sigma = q n \mu_{FE}, \tag{3.7}$$

where μ_{FE} is the field effect mobility. Substituting **Equation 3.5** into **Equation 3.7** gives the field effect mobility of charge carriers,

$$\mu_{FE} = \frac{d}{\epsilon \epsilon_0} \frac{\sigma}{V_g}. \tag{3.8}$$

A direct linear fit of conductivity versus gate voltage (**Figure 3.1b**) gives a good estimate for the mobility of the device. Other methods include linearisation of the conductivity curve [45] or differentiation of the conductivity curve to find the maximum gradient ($\frac{d\sigma}{dV_g}$). However, all three techniques usually give similar results.

Hence, measuring the conductivity versus applied gate voltage of a graphene FET and applying the parallel plate model gives an indirect method of characterising the field effect mobility (**Equation 3.8**) and carrier concentration (**Equation 3.5**).

Note that the 1C model is based on the assumption that both SLG and the gate are metal plates of a parallel plate capacitor. Thus, all the electric field is confined in the SiO_2 layer. However, SLG is not a metal and the electric field can penetrate through it, as was shown in a double SLG vertical tunnelling FET device [171]. This effect does not alter the carrier concentration and field effect mobility in pristine SLG and SLG encapsulated by hBN. However, in graphene functionalised with NCs and other hybrid graphene devices with top dielectric layers [172] this electric field can lead to significant redistribution of charge. This behaviour can be explained by the two-capacitor (2C) model introduced in the next section.

3.2 The two-capacitor (2C) model

In the 2C model, the device is treated as a double capacitor: the first capacitor is that of the gate/dielectric/SLG layers (analogous to the 1C model, **Figure 3.2a**) and the second capacitor is the 'effective' capacitance of the top layer (**Figure 3.2b**).
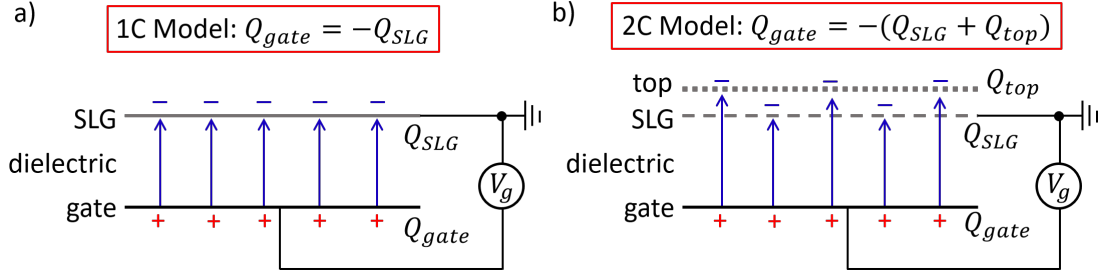
Figure 3.2. a) A diagram of the parallel plate capacitor (1C) model, where $Q_{gate} = -Q_{SLG}$. **b)** A diagram of the 2C model for functionalised graphene, where the electric field penetrates through the SLG and $Q_{gate} = -(Q_{SLG} + Q_{top})$.

The 2C model is based on three key assumptions:

(i) Graphene is a conductor with a low concentration of free carriers ($< 10^{12}$ cm^{-2}) and so it only weakly screens the electric field generated by the bottom gate electrode.

(ii) The top layer behaves effectively as an additional capacitor that can hold a high density of charges ($> 10^{12}$ cm^{-2}). This assumption is material dependent and limits the use of the 2C model to systems where the top layer has a high density of states at energy $E = E_F$ in SLG.

(iii) There is efficient charge transfer between the top layer and graphene due to the density of states in the top layer greatly exceeding that of graphene (assumption (ii)).

Using these assumptions, we model a system where the electric field from the gate can penetrate through the graphene layer inducing a charge in the top layer, Q_{top}. Thus, any charge induced in the gate by an applied gate voltage is

now compensated by both the SLG and the top layer, such that

$$Q_{gate} = -(Q_{SLG} + Q_{top}). \tag{3.9}$$

This charge can drain through the SLG layer following a change of V_g, but is limited by the charge transfer time associated with the top layer and so the charge in the top layer is a function of applied gate voltage and time, $Q_{top}(V_g, t)$.

The dynamics of the top layer charging is analogous to the charging of a conventional capacitor. The charge density per unit area on the gate electrode is,

$$Q_{gate} = V_g C_0, \tag{3.10}$$

where C_0 is the capacitance of the single gate/dielectric/SLG capacitor. The difference between the gate electrode charge, Q_{gate}, and the charge present in the top layer, Q_{top}, leads to a potential difference,

$$\Delta V_g = V_g - \left(\frac{Q_{top}}{C_0} \right), \tag{3.11}$$

which can be used to calculate the amount of charge stored/released by the top layer in a time interval Δt,

$$\Delta Q_{top} = \Delta V_g C_0 \left[1 - \exp \left(\frac{-\Delta t}{\tau_{top}} \right) \right]. \tag{3.12}$$

Here, τ_{top} is the only fitting parameter of our 2C model. **Equation 3.12** and the conservation of charge (**Equation 3.9**) can be used to calculate the magnitude of the charge in the SLG layer. Using small ($\Delta t = 10$ ms) time steps we can numerically model the dynamic change of charge distribution in the top/SLG/gate layers as a function of time, t, (**Figure 3.3a**) and applied gate voltage, $V_g(t)$, with a fixed V_g sweep rate (typically $0.1 - 0.3$ V/s), see **Figure 3.3b**.

The model was developed primarily to describe a graphene FET function-
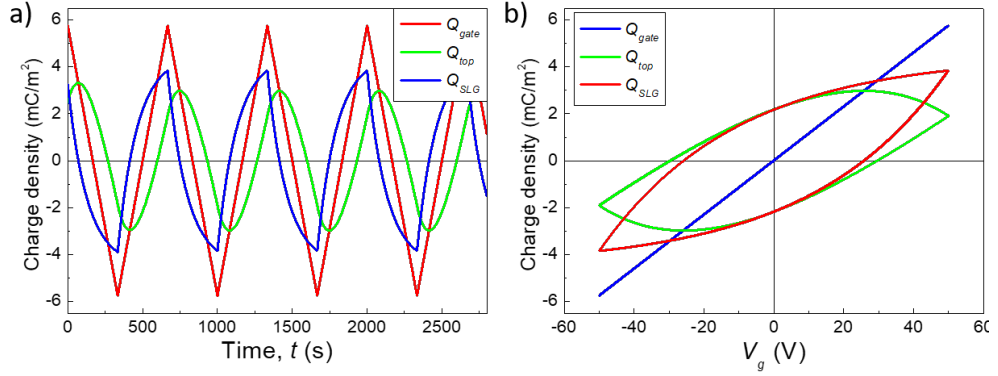
Figure 3.3. **a)** Dynamics of the charge density stored on the bottom gate electrode (Q_{gate}), top layer (Q_{top}) and single layer graphene (Q_{SLG}) with multiple gate voltage sweeps to ± 50 V and sweep rate = 0.3 V/s for a Si/SiO$_2$/SLG FET with 285 nm of SiO$_2$. **b)** Q_{gate}, Q_{top} and Q_{SLG} plotted as a function of the applied gate voltage V_g.

alised with perovskite NCs (see **Section 5.5.1**), but has since been used to describe the behaviour of a graphene FET with mechanically stamped ferroelectric CuInP$_2$S$_6$ (CIPS) flakes [172]. Despite being completely different materials, the model performs well for both systems and it is believed that the 2C model can be applied to any functionalised SLG system where the functional layer has a density of states much larger than the graphene coupled with efficient charge transfer between the two.

3.3 Magnetoresistance and Hall effect in 2D materials

The classical magnetoresistance of a device or material is a consequence of its electrical transport behaviour in the presence of externally applied magnetic fields. The Hall effect is a useful phenomenon for determining the carrier type and concentration in a material and allows direct measurements of the Hall mobility, μ_H, of charge carriers. Typically, for magneto-transport measurements a Hall bar device geometry is used (**Figure 3.4a**). In the Hall bar configuration a current, I_x, is applied across the conductive channel and the longitudinal voltage across the direction of current flow, V_{xx}, is measured. In the absence of a magnetic field, the transverse voltage, V_{xy}, that is the voltage measured perpendicular to the
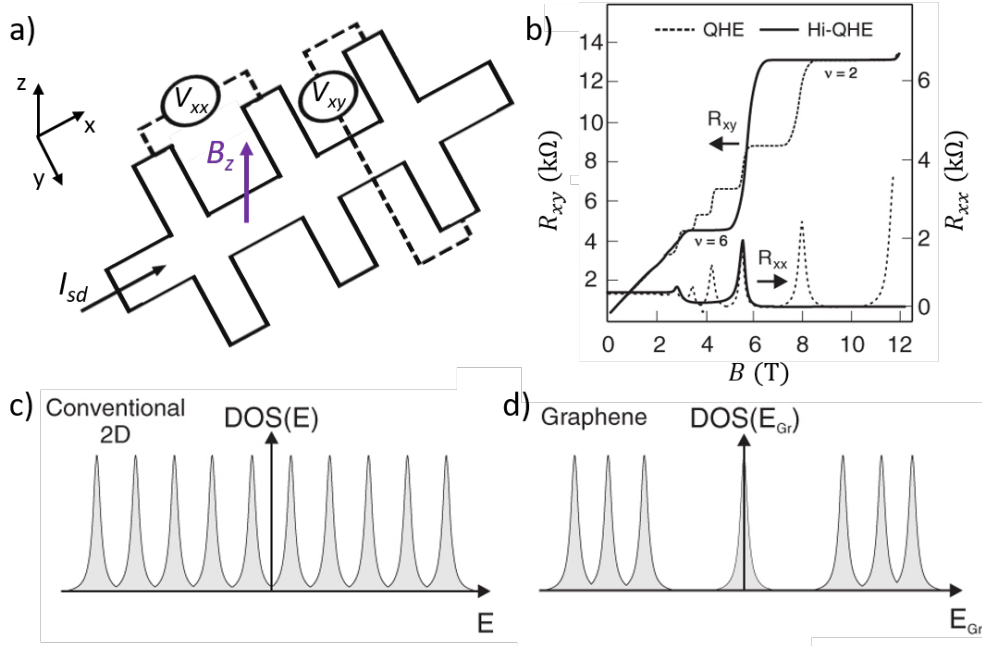
Figure 3.4. a) Schematic of the Hall bar configuration used for magneto-transport measurements. **b)** Comparison of QHE (dashed lines) in conventional 2D systems and the Hi-QHE (solid lines). For graphene, only $\nu = 2$ and $\nu = 6$ are shown for clarity. Figure reproduced from Ref. [173]. Sequence of Landau levels for **c)** conventional 2D systems and **d)** graphene. Figure reproduced from Ref. [173].

current, is zero. However, when a magnetic field is applied perpendicular to the device, $B_z \neq 0$, the charge carriers experience a Lorentz force perpendicular to the direction of current flow and magnetic field, resulting in a measurable Hall voltage, $V_H = V_{xy} \neq 0$. For a 2D system with a density of charge carriers n, the current density is

$$\mathbf{J} = nq\mathbf{v} = (J_x, 0, 0), \tag{3.13}$$

where q is the charge of carriers with velocity $\mathbf{v}$. The Hall voltage (V_H) and Hall coefficient (R_H) are defined as

$$V_H = V_{xy} = \frac{I_x B_z}{nq}, \tag{3.14}$$

and

$$R_H = \frac{E_y}{J_x B_z} = \frac{V_H}{I_x B_z} = \frac{1}{nq}, \tag{3.15}$$

where $I_x = I_{sd}$ is the current applied across the Hall bar and E_y is the electric field perpendicular to the current flow. For a semiconductor with 2D charge carrier density (per unit area) n the mobility of charge carriers is calculated as

$$\mu_H = \frac{\sigma}{qn} = \sigma R_H, \tag{3.16}$$

where σ is the conductivity. Measurements of graphene FETs in applied magnetic field and gate voltage can be used to compare Hall and field effect mobilities revealing interesting physical phenomena (see **Section 7.7**).

The classical Hall effect breaks down for high mobility 2D systems at low temperatures and high magnetic fields [174]. Under these conditions the Hall resistance, R_H, follows quantised steps forming plateaus in resistance, whilst the longitudinal resistance simultaneously vanishes ($R_{xx} = 0$, see **Figure 3.4b**); this is the quantum Hall effect (QHE). The QHE plateaus occur at quantised multiples of resistivity, $\rho_{xy} = h/\nu e^2$, where ν is an integer, understood through the Landau level (LL) quantisation of electron motion [3]. For conventional 2D semiconductors, where charge carriers are described by the Schrödinger equation, the energy spacing of Landau levels, $E_{LL} \propto B$ (**Figure 3.4c**). In graphene, where the charge carriers are instead described by the Dirac equation, the Landau level spacing is $E_{LL} \propto \sqrt{B}$ (**Figure 3.4d**). This gives rise to a unique formation of QHE plateaus in graphene, referred to as the half-integer QHE (Hi-QHE), with a sequence that is shifted with respect to the standard QHE sequence by $\frac{1}{2}$, so that $\rho_{xy} = \pm\frac{h}{4e^2(N+\frac{1}{2})}$, where N is the LL index ($N = 0, 1, 2, ...$) and factor 4 appears due to double valley and double spin degeneracy [40]. The LL filling factor, $\nu = 4(N + \frac{1}{2})$ results in QHE plateaus at $\nu = 2$, 6 and 10 for graphene (**Figure 3.4b**) and the expected value of the resistance of the Hall plateau for $\nu = 2$ is the resistance quantum, $h/2e^2 = 12.9$ kΩ, which is universal for all materials.

4 Device fabrication and experimental techniques

This section describes the techniques involved in processing graphene FETs, synthesising perovskite NCs and fabricating the different types of devices used in this project. Furthermore, the experimental techniques involved in characterising the transport, magneto-transport, optical and optoelectronic properties of the devices and/or materials are presented.

4.1 Processing of graphene devices

Graphene field effect transistors (FETs) are fabricated to study the electrical properties of graphene and graphene based devices. Graphene FET properties can vary depending on a variety of factors including the growth method and substrate type (**Section 2.3**). The main type of graphene used in this project is commercially grown CVD graphene on Si/SiO$_2$ with carrier mobility $\mu \sim 10^3 - 10^4$ cm^2/Vs at room temperature ($T \sim 300$ K) provided by Graphenea [70] or Graphene Supermarket [71], as well as a few other non-commercial sources that are stated throughout the work where relevant. Typical SiO$_2$ thickness is either 285 nm or 300 nm and is stated where relevant to specific devices. Fully processed commercial graphene FETs with 90 nm thick SiO$_2$ were also acquired from Graphenea [175]. Some devices were produced with a layer of hBN between the SiO$_2$ and graphene to improve the electrical properties of the graphene, as described in **Section 2.3**. The Si/SiO$_2$/graphene wafers were processed by Dr. Zakhar Kudrynski and Dr. Richard Cousins at the University of Nottingham, through access to electron beam lithography (EBL) facilities at the Nanoscale and Microscale Research Centre (nmRC).

The Si/SiO$_2$/graphene wafer is spin-coated with polymethyl methacrylate (PMMA) and patterned into two device architectures via EBL; short two-terminal diodes for photocurrent measurements and Hall bars for electrical and magneto-
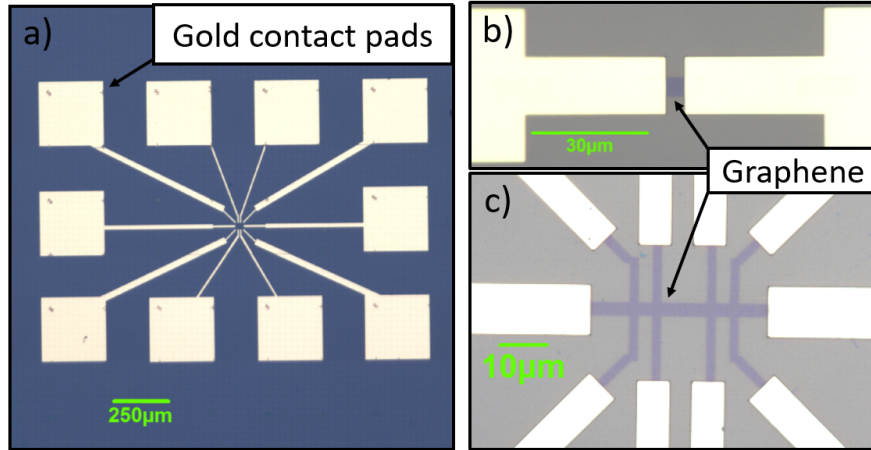
Figure 4.1. a) Optical image of an EBL processed 10-terminal graphene Hall bar device with gold contact pads. Optical images of the two main device architectures; **b)** 2-terminal short diode and **c)** 10-terminal Hall bar.

transport characterisation (**Figure 4.1a-c**). EBL uses an accelerated beam of electrons to break the long chain PMMA molecules outside of the device architecture into smaller, more soluble, chains, which are then removed by developing the wafer in an isopropyl alcohol (IPA) and deionised water solution. Next, plasma etching is utilised to remove the exposed graphene leaving behind the unexposed, PMMA-covered graphene in the desired device geometry. Finally, the Au/Ti contacts are deposited by metal deposition using a thermal evaporator and the wafer is cleaned in hot ($T \sim 65°$C) acetone for 1-3 h to remove the excess metal and unexposed PMMA. The wafer is rinsed in IPA and dried with a pressurised nitrogen gas stream before being covered in a protective coating of PMMA ready for dicing and/or storage. The full details of graphene device processing are described in detail in a manual produced by our group [176].

The processed wafers are diced into $\sim 4 \times 4$ mm^2 chips either using a Dynapert Precima scribing system or by diamond saw at the Teledyne UK Limited lab, operated by Dr. Sarah Heywood. The small chips, which typically contain 1-4 devices, are cleaned in hot ($T \sim 65°$C) acetone for 1 h, rinsed with IPA and dried with pressurised nitrogen gas to remove the protective PMMA coating. Devices are annealed in a tube furnace at $T = 300°$C for 3 h in a 5% H$_2$ and 95% Ar
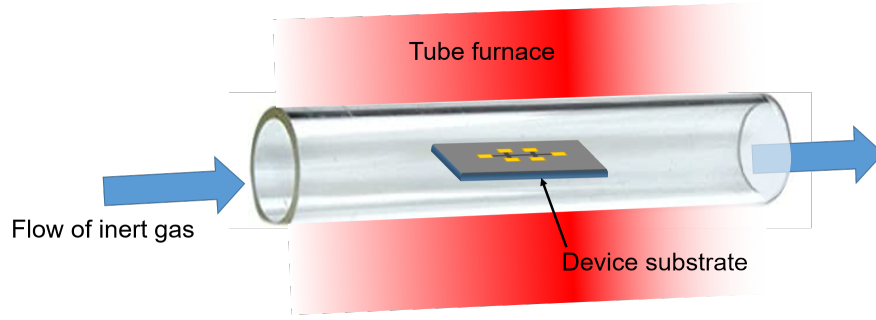
Figure 4.2. Illustration of furnace annealing process

flowing gas atmosphere to remove surface impurities and residues on the graphene (**Figure 4.2**). The mounting and bonding of the chips for electrical characterisation is presented in **Section 4.3**.

4.2 Inkjet-printed graphene FETs

Inkjet-printed devices were fabricated by Dr. Feiran Wang and Mr Jonathan Austin at the Centre for Additive Manufacturing (CfAM), University of Nottingham.

The inkjet printing process of low-dimensional materials is rather complex and requires the optimisation of many parameters for the printer and ink formation (e.g. viscosity, concentration, print height, etc) and so only a simplified process is described here. A commercial graphene-polymer ink from Sigma-Aldrich (product number: 793663 [77]) was used to print the presented devices. The ink consists of liquid exfoliated graphene flakes (average size of 2590 nm^2) mixed with ethyl cellulose (EC) and dispersed in a mixture of cyclohexanone/terpineol (85:15 by volume) to achieve suitable rheological properties for inkjet printing. The graphene ink is deposited onto a glass, Si/SiO$_2$ or flexible substrate using a drop-on-demand (DoD) piezo driven Fujifilm Dimatix DMP-2800 inkjet printer and a 10 pL drop volume cartridge. Typically, a drop spacing of 20 μm is used but was also adjusted depending on device requirements. For multi-layer devices a pause of 30 s between layers is used to allow evaporation of the solvents in order to achieve improved

surface morphology and geometrical precision. The films are then annealed for 2 h in a vacuum oven under 1 mbar vacuum pressure at annealing temperatures from $200 - 400°$C. Contacts are made by jet printing of silver, manual application of silver paste or the film can also be deposited on a pre-patterned $Au/SiO_2/Si$ wafer.

4.3   Mounting and bonding devices

Non-magnetic headers produced in-house are used for mounting samples on (**Figure 4.3a-b**). These have either 12 or 8 pins and can have a copper plate (as seen under the device in **Figure 4.3c**) to help improve electrical contact with the back gate of the Si/SiO_2 substrate. The device is mounted onto the header and held in place using silver conductive paste. The silver paste, once dry, also acts as a conductive bridge between the back gate and one of the pins on the header (**Figure 4.3c-d**). The contact pads on the device are bonded to a pin on the header using 50 μm diameter gold wire and DuPont conductor paste (4929N), as shown in **Figure 4.3c**. A smaller type of header had to be used for compatibility with the equipment at the Laboratoire National des Champs Magnétiques Intenses (LNCMI) in Toulouse for high magnetic field ($B < 60$ T) measurements (**Figure**
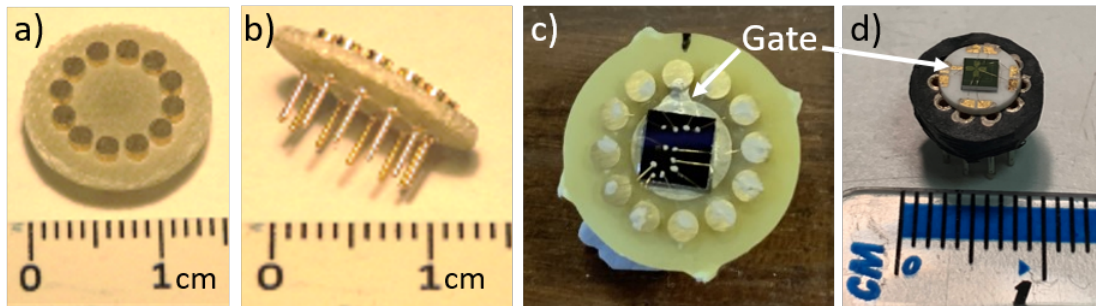
Figure 4.3. a-b) Optical images of 12-pin non-magnetic header. **c)** Optical image of a bonded graphene/SiO_2/Si device mounted on a copper-plated header. **d)** Optical image of non-magnetic header with bonded inkjet-printed graphene/SiO_2/Si used for high magnetic field measurements at LNCMI, Toulouse.

4.3d). These were also bonded using the silver paste and gold wire technique described above, but can also be bonded using a wedge-bonding machine available at the LNCMI facility.

4.4 Perovskite nanocrystal synthesis

The all-inorganic caesium lead halide, $CsPbX_3$ (X = Cl, Br, I or mixed), perovskite nanocrystals (NCs) were synthesised by Dr. Chengxi Zhang at the University of Nottingham (**Figure 4.4a**). The synthesis involved a hot injection method and post-synthesis ligand exchange, which is reported in Ref. [24]. Typically, capping ligands, such as oleic acid (OA) and oleylamine (OLA) are used to passivate the dangling bonds on the surface of the NCs. Briefly, the synthesis requires two precursor solutions; a lead halide (e.g. PbI_2) combined with OA and OLA as well as a Cs-oleate consisting of caesium and OA. The PbI_2-OA-OLA precursor solution is heated to 160°C and the Cs-oleate precursor (heated to 150°C) is quickly injected whilst stirring. After 20s of mixing the solution is cooled on an ice-bath. A post-synthesis ligand exchange reaction is performed to replace OA ligands with bidentate $2, 2'$-iminodibenzoic acid (IDA) to improve the coordi-
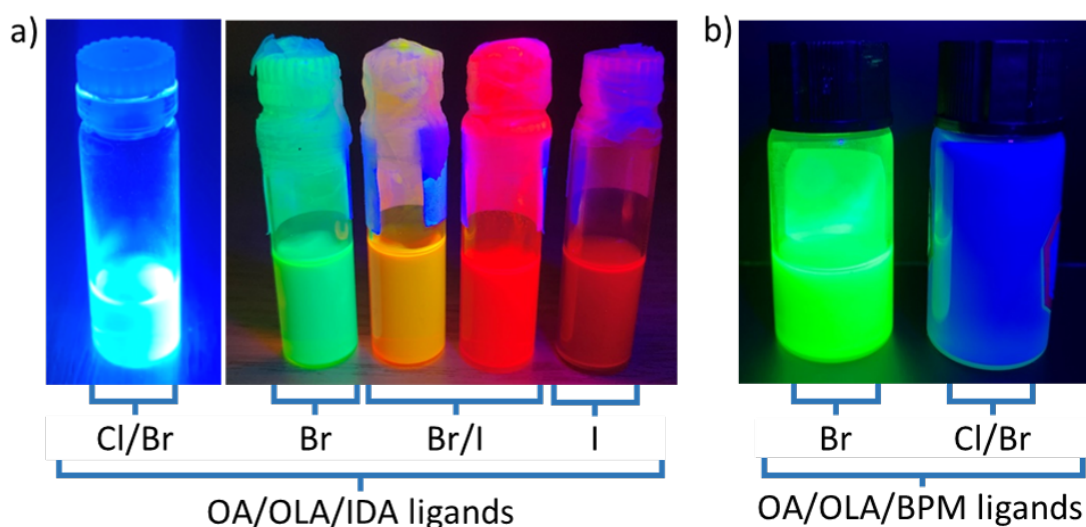
Figure 4.4. Images of the different perovskite NCs (under $\lambda_{ex} = 365$ nm illumination) that were synthesised for use in these studies with labelled halide content using **a)** IDA and **b)** BPM capping ligands.

nation to and passivation of surface defects. IDA is added to the perovskite NC solution and stirred for 6 h at an optimal temperature of 40°C. The solution is left to self-precipitate overnight followed by a series of centrifusion procedures before the final precipitate is collected and dispersed in hexane. The perovskite NC and hexane solution is stored in sealed bottles in a fridge without light to prevent solvent evaporation and capping ligand degradation. Some NCs were also synthesised by Dr. Chengxi Zhang at Shanghai University, with bromophenylmethyl (BPM) ligands instead of IDA in an effort to improve the long-term stability of the NCs (**Figure 4.4b**).

4.5   Morphological and optical characterisation

This section describes the morphological and optical characterisation methods used for studying the properties of perovskite NCs, namely, transmission electron microscopy (TEM), photoluminescence (PL) spectroscopy and time dependent PL spectroscopy.

4.5.1   Transmission electron microscopy

TEM imaging employs a high voltage electron beam in a vacuum column that is focused onto a sample using an electromagnetic lens. The beam passes through the sample, which must be very thin (<100 nm), and is either scattered or transmitted onto a screen. The interaction of the electron beam with the sample depends on the electron density of the matter being imaged. This imaging technique offers magnification up to $1,000,000\times$ and resolution down to ~ 2 Å, hence the structure of individual NCs to be resolved. Perovskite NC samples are prepared for TEM imaging by drop-casting with a syringe onto an ultra thin (<1 nm) graphene oxide support grid. TEM images were recorded on a 200 kV JEOL 2000 FX TEM, operated by Dr. Michael Fay.

4.5.2 Photoluminescence spectroscopy

Photoluminescence (PL) is the process by which light energy incident on a material stimulates the radiative emission of photons. For semiconductors, an excitation laser with photon energy $E_{ex} = h\nu$ greater than the band gap energy (E_g) of the material, i.e. $E_{ex} > E_g$, is focused onto the surface of the material. The photons are absorbed by the material and excite electrons from the valence band (VB) to the conduction band (CB) (**Figure 4.5a**). The PL emission occurs when the excited electron from the CB recombines with a hole in the VB, emitting a photon with energy (E_{ph}) less than the initial excitation energy i.e. $E_{ph} = E_g$.
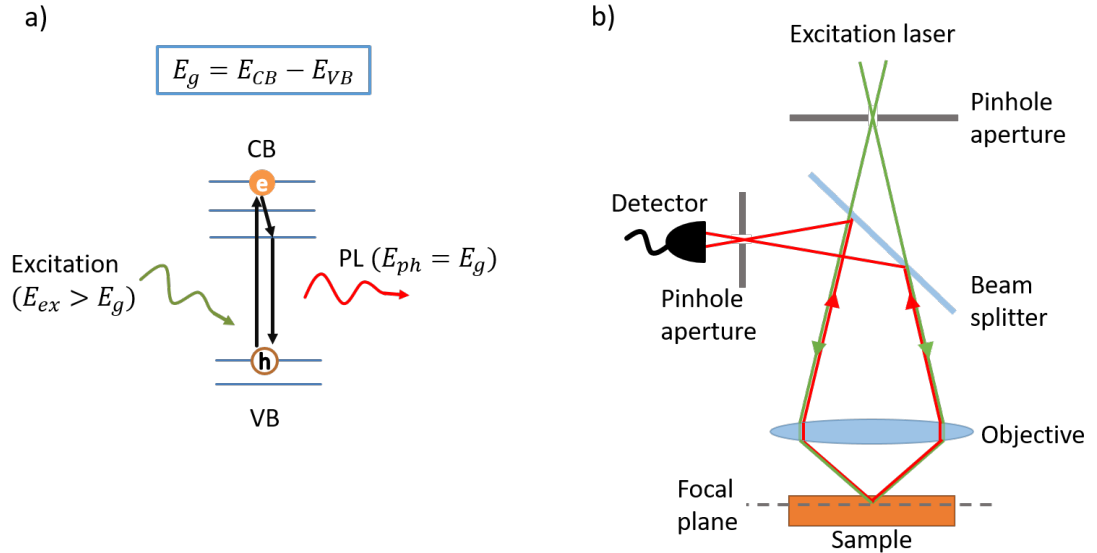
Figure 4.5. **a)** Illustration of photon absorption and radiative emission process involved in PL. **b)** Schematic diagram of the confocal microscope system used for PL spectroscopy studies.

PL studies on perovskite NCs are performed using a Horiba Jobin Yvon micro-PL system equipped with both a He-Ne and frequency doubled Nd:YVO$_4$ laser for excitation with wavelengths $\lambda_{\text{ex}} = 633$ and 532 nm, respectively. A confocal microscope system (**Figure 4.5b**) is used to focus the excitation laser onto the sample with a typical focused spot diameter of $d_{laser} \sim 1$ μm. The optically emitted signal is directed back through the confocal microscope onto a LabRAM HR-UV spectrometer equipped with 150 and 1200 grooves/mm gratings

and a Si charge-coupled device (CCD) for detection in the range $350 - 1100$ nm. This setup is designed with a motorised xy linear positioning stage, which allows the user to perform PL mapping over a 2D area of the sample, with a step size of 0.1 μm. A cold-finger optical cryostat with a 1 mm sapphire window is used in place of the motorised stage for PL measurements in vacuum and temperature (6 K $< T <$ 300 K) dependent PL studies. Temperature is controlled using the method described in **Section 4.7.3**, with cooling power provided by helium flux through a transfer line from a pressurised dewar.

Time dependent PL spectroscopy is performed using the above methods in either continuous wave or pulsed excitation mode whilst acquiring the resultant PL spectra at periodic intervals.

4.6 Functionalisation of graphene with perovskite nanocrystals

The aim of perovskite deposition is to form a thin, evenly distributed layer of NCs covering the whole surface of the graphene device. The perovskite NC solution was deposited by syringe drop-casting. The drop-casting technique comprises of extracting a volume of the perovskite NCs in hexane solution from the storage bottle using a 1 mL syringe with 0.45 mm hypodermic needle (**Figure 4.6a**). The solution is deposited drop-by-drop onto the desired substrate (**Figure 4.6b**) and allowed to dry (~ 2 mins) in ambient conditions. During drying the hexane solvent evaporates and leaves behind the deposited NCs on the substrate in a 'coffee stain' pattern, as shown in **Figure 4.6c**.

For more precise deposition, polytetrafluoroethylene (PTFE) tape was used as a 'paintbrush' (**Figure 4.6d**). The perovskite NCs are first drop-cast onto the end of the PTFE tape and are then 'painted' onto the substrate by bringing the droplet on the tip of the PTFE tape close to the surface. During the transfer from
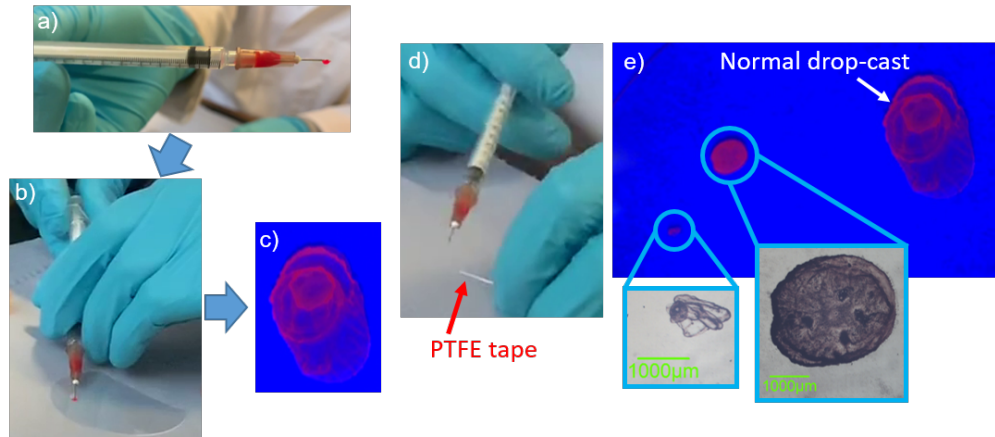
Figure 4.6. a-b) Images illustrating the syringe drop-casting technique. **c)** Image of the coffee stain effect of drop-cast NCs under UV (365 nm) illumination. **d)** Image showing the PTFE tape used as a paintbrush for finer deposition control. **e)** Image of the deposition formation under UV light using the PTFE tape method compared to normal drop-casting with optical microscope image insets.

PTFE 'brush' to the substrate, the solvent partially evaporates (**Figure 4.6e**), resulting in a smaller drop size deposited onto the graphene channel. This process is performed under an optical microscope for improved positional control. The PTFE tape 'brush' was chosen as it is soft and therefore does not damage the graphene surface.

4.7 Transport characterisation

This section outlines the methods for measuring the transport properties of devices including, measurements of electrical conductivity and its dependence on gate voltage, field effect mobility and carrier concentration. The experimental methods for controlling temperature and measuring magneto-resistance and Hall mobility are also detailed.

4.7.1 Electrical measurements

The planar devices that we study are typically field effect transistors consisting of 3 main electrodes: source, drain and gate (**Figure 4.7a**). The source and drain are the contacts either side of the conductive channel (e.g. graphene) and are used to apply voltage or current across the device. The gate contact is used to apply a gate voltage, which leads to an electric field across the dielectric material (typically SiO_2).

Electrical measurements are typically carried out by mounting the device in a homemade vacuum cryostat (**Figure 4.7c**) and a Pfeiffer turbo-molecular vacuum pump is used to create a vacuum pressure of around 10^{-6} mbar. The device is mounted into the cryostat by positioning the pins on the header into the 12-pin socket. The device is now electrically connected through the cryostat into a breakout box with BNC connectors corresponding to the 12 pins on the cryostat socket (see **Figure 4.7c**). Current-voltage (I-V) measurements are performed using a Keithley 2400 direct current (DC) SourceMeter in a two-terminal configuration between source and drain contacts using a ground plug to complete the circuit through the device and back to the Keithley 2400 SourceMeter. The Keithley 2400 can be used to apply a voltage and measure the resulting current simultaneously. It is also possible to ramp the applied voltage between user-defined setpoints to measure current as a function of applied voltage.

Gate voltage measurements are performed using a second Keithley 2400 SourceMeter to apply a voltage to the gate of the device. One Keithley 2400 is used to apply a constant voltage across the source-drain and the second Keithley 2400 is used to slowly sweep the voltage applied (typically ~ 0.1 V/s) to the gate electrode. Sweeping the gate voltage too quickly can cause a build up of reactive current through the gate that can be detrimental to the device. The gate leakage current, I_g, (typically $I_g < 10$ nA) is constantly monitored, and gives an indication
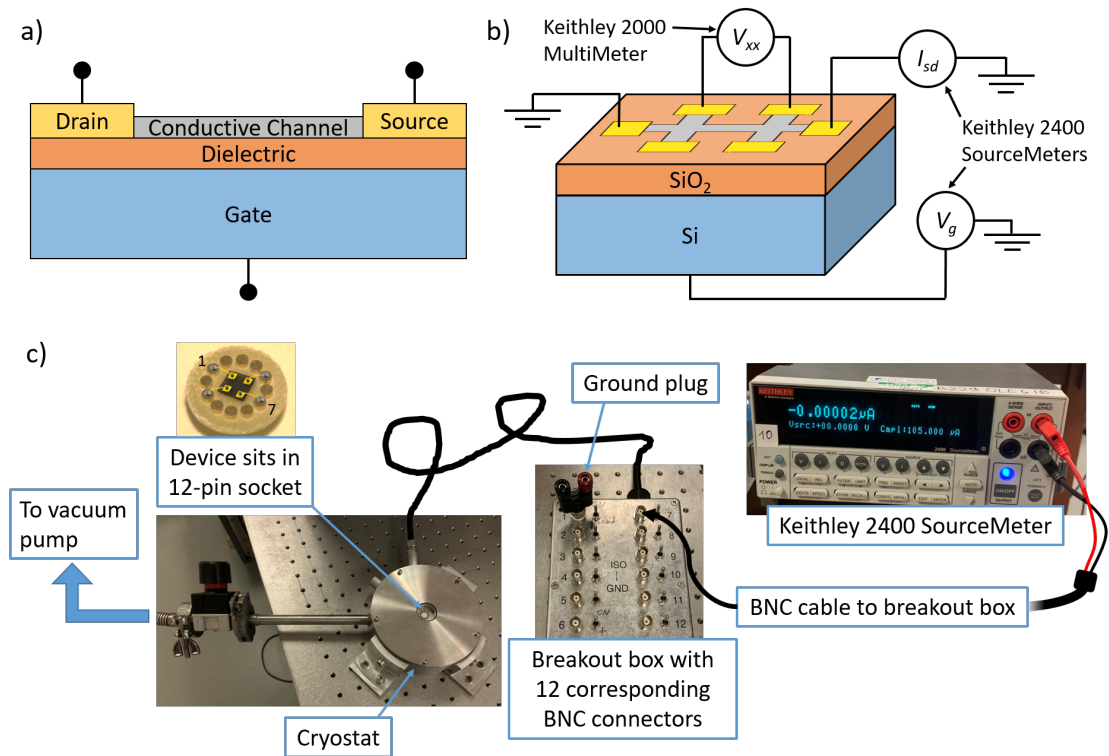
Figure 4.7. **a)** A layer structure diagram showing the basic structure of a FET. **b)** 3D schematic of four-terminal measurement of a Hall bar device. **c)** Schematic diagram with optical images of key components that are used for the electrical measurement of devices (images not to scale).

of the stability of the gate. Excessive leakage ($I_g > 100$ nA) can lead to electrical breakdown of the transistor as conductive pathways are formed between the gate electrode and the conductive channel of the device.

In a four-terminal configuration, resistance is measuremed by introducing a Keithley 2000 MultiMeter to read the voltage between two inner points on the conductive channel (V_{xx}), thus eliminating the lead and contact resistance associated with two-terminal measurements (**Figure 4.7b**). In this configuration one Keithley 2400 is used to apply a constant current (I_{sd}) across the conductive channel, the second Keithley 2400 is used as the back gate voltage source (V_g) and the Keithley 2000 read is used to measure the four-terminal voltage.

4.7.2 Field effect mobility and carrier concentration measurements

The mobility of carriers in a graphene FET device can be calculated from 4-terminal measurements (**Section 4.7.1**) of the voltage, V_{xx}, across a graphene channel of length L and width w using the parallel plate capacitor model (**Section 3.1**). The voltage is first converted into a conductivity,

$$\sigma_{xx} = \frac{1}{\rho_{xx}} = \frac{L}{w}\frac{I_{sd}}{V_{xx}}, \tag{4.1}$$

where ρ_{xx} is the resistivity and I_{sd} is the current applied across the source-drain channel. The carrier concentration is determined by taking the gate voltage position of the resistivity maximum and using **Equation 3.6**. The linear region close to the conductivity versus gate voltage minimum is fit with a linear line of best fit and the resulting gradient is used in **Equation 3.8** to calculate the field effect mobility.

4.7.3 Temperature and magnetic field dependence

To study the properties of devices in a range of temperatures and magnetic fields, specialised equipment was used. Measurements were performed in vacuum or helium atmosphere in the temperature range 1.5 K $< T <$ 500 K and with magnetic field up to $B = 16$ T (persistent field) and $B = 60$ T (pulsed field).

The homemade bench-top cryostats utilise a 100 Ω platinum resistor (Pt100) to measure temperature. A Lakeshore 331, 340 or 350 temperature controller is used to provide PID controlled temperature stabilisation with heating power in the range between 2.5 mW and 25 W. The cryostats are compatible with a homemade copper 'cold-finger' nitrogen bucket (**Figure 4.8a**), which can be filled with liquid nitrogen to provide cooling power. This configuration allows for cooling of the cryostat down to $T \sim 100$ K and heating of up to $T \sim 500$ K. For temper-
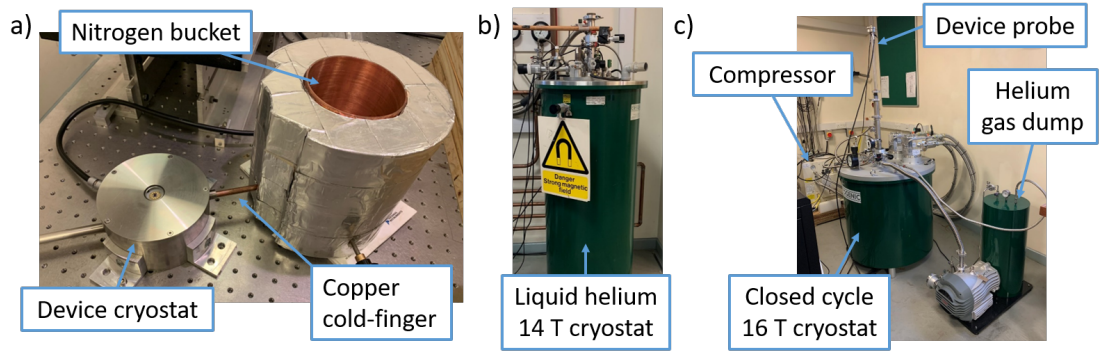
Figure 4.8. **a)** An image of the bench-top microscope cryostat with nitrogen bucket for measurements at $100 < T < 500$ K. **b)** An image of the liquid helium superconducting magnet cryostat system. **c)** An image of the new cryo-free High T Mag system used for low temperature and high magnetic field measurements.

ature dependent studies at $T < 100$ K the samples were mounted into a probe and lowered into a liquid helium cooled cryostat designed for high magnetic field measurements at temperatures down to 4.2 K (**Figure 4.8b**). Measurements at 1.6 K $< T < 400$ K and $B \leq 16$ T were performed in a 'High T Mag' Cryogenics cryo-free closed cycle helium system (**Figure 4.8c**).

4.7.4   Magneto-transport and Hall mobility studies

For magneto-transport measurements, a Hall bar device geometry is used (**Figure 4.9a**). In this device structure, a current, I_{sd}, is applied across the conductive channel and the voltage across the direction of current flow, V_{xx}, is measured. The transverse, or Hall, voltage can be measured in the presence of an externally applied magnetic field (see **Section 3.3**).

The four-terminal method (**Section 4.7.1**) was adapted to measure the Hall voltage. This is achieved by introducing a second Keithley 2000 MultiMeter so that longitudinal voltage, V_{xx}, and Hall voltage, V_{xy}, can be measured simultaneously (**Figure 4.9a**).

The 'High T Mag' system described in **Section 4.7.3** produces a $B \leq$
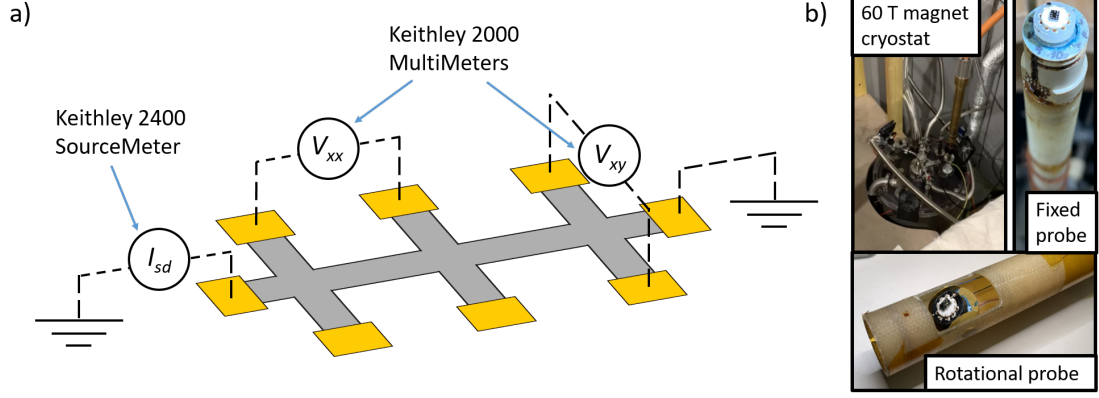
Figure 4.9. **a)** Schematic of the electrical configuration for magneto-transport measurements. **b)** Labelled images of the magnet cryostat, fixed probe and rotational probe used for $(B < 60\text{ T})$ measurements at LNCMI in Toulouse.

16 T persistent field via a superconducting magnetic coil. The superconducting magnet is maintained at $T \approx 3$ K and is decoupled from the sample space, thus magnetic field measurements can be performed in the whole temperature range from $1.6 - 400$ K. The magnetic field can be swept in the range from -16 to $+16$ T at an average rate of ~ 0.283 T/min or held at a persistent field within that range. The device is mounted onto a magneto-transport probe, which positions the device perpendicular to the magnetic field, in centre of the magnet.

High field $(B \leq 60\text{ T})$ measurements were carried out at The Laboratoire National des Champs Magnétiques Intenses (LNCMI) in Toulouse, France. These are non-destructive pulsed magnetic fields that are created by discharging a capacitor through a liquid nitrogen-cooled resistive coil in very short times (~ 100 ms). Hall probes are used for accurate measurements of the device angle with respect to the direction of the applied magnetic field. This allows the magnetic field to be applied perpendicular, angled or parallel to the direction of current flow (**Figure 4.9b**). Twisted pair wiring was also used to reduce the presence of parasitic voltages induced in the wires by the pulsed magnetic fields. Parasitic Eddy currents were compensated via comparative analysis of both the up and down magnetic field ramps, using Python-based data analysis software provided by LNCMI.

4.8 Optoelectronic characterisation

This section describes the experimental procedures used for measurements of the optoelectronic properties of photosensitive devices, including the measurements of photocurrent, response times and device dependence under excitation with laser light of different wavelengths, λ_{ex}, and powers.

4.8.1 Photocurrent measurements

DC photocurrent measurements are performed using a Keithley 2400 Source-Meter to simultaneously apply a bias voltage and measure the current in the device over time. Photocurrent, I_{ph}, is measured as the difference in current across a device in the dark (I_{dark}) versus under illumination (I_{light}):

$$I_{ph} = I_{light} - I_{dark}. \tag{4.2}$$

The device is mounted into an optical cryostat, which has a sapphire window allowing for the light source to be directed through and focused onto the device. The first measurement is the dark state calibration, which gives the base level (I_{dark}) for photocurrent measurements. Then, an unfocused light source (i.e. spot diameter larger than size of device) is used to illuminate the sample whilst continuously measuring the resulting current across the device. The bias voltage or gate voltage applied to the device is adjusted using Keithley 2400 SourceMeters to maximise photocurrent.

Photocurrent is measured at different temperatures using the cold-finger nitrogen bucket attached to the cryostat (**Section 4.7.3**). The following light sources are employed: a 6-wavelength (6λ) fibre-coupled laser system (**Figure 4.10a**) with wavelength outputs of $\lambda_{ex} = 405, 450, 520, 635, 808$ and 1060 nm, full width at half maximum (FWHM) < 2 nm and power output > 30 mW per
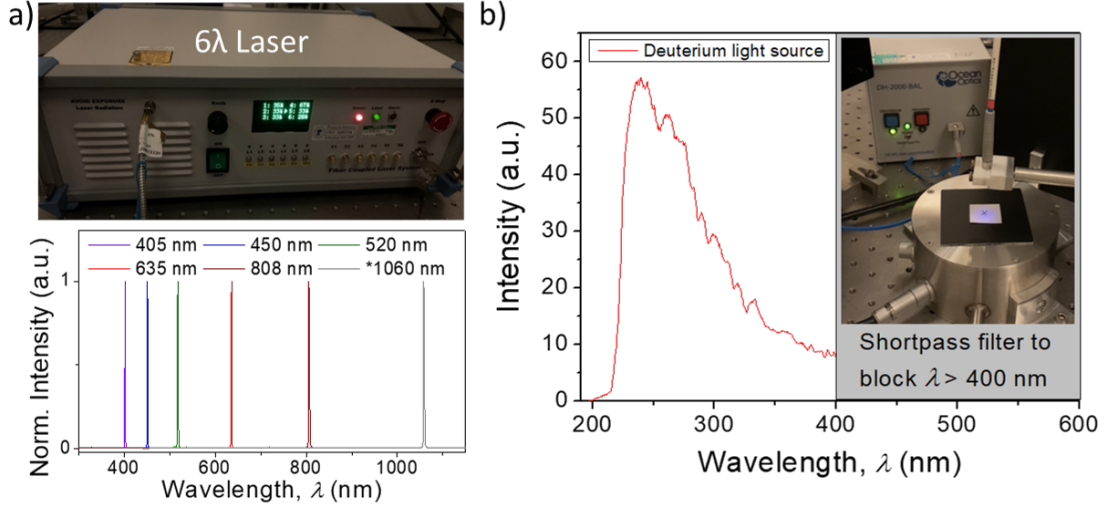
Figure 4.10. a) An image of the 6λ system (top) and corresponding laser output spectra (bottom). *1060 nm spectra is estimated only. **b)** The output spectra of the deuterium lamp source using a 400 nm short-pass filter. Inset: an image of the deuterium lamp in operation. All wavelength spectra was measured with an Ocean Optics FLAME-S-XR1-ES spectrometer.

channel; a deuterium lamp ($\lambda_{ex} \approx 250$ nm) coupled with a 400 nm short-pass filter (**Figure 4.10b**); a $\lambda_{ex} = 405$ nm diode laser; a $\lambda_{ex} = 633$ nm HeNe laser; a UV torch ($\lambda_{ex} = 365$ nm) for qualitative assessment of the UV response; a Spex Industries Minimate monochromator with Newport quartz tungsten halogen lamp; and a Horiba microHR UV-enhanced monochromator with Ushio xenon arc lamp (see **Section 4.8.4** for monochromator operation).

4.8.2 Temporal response

Photocurrent measurements for devices with response time > 1 s are performed using a Keithley 2400 SourceMeter (**Section 4.8.1**). The Keithley 2400 is limited by its data acquisition rate, which can be improved but with the loss of measurement precision. A reasonable data acquisition time for photocurrent measurements in this setup is $100 - 200$ ms. For response time faster than 100 ms a Tektronix DPO 4032 Digital Phosphor Oscilloscope is used to measure the voltage across a resistor that is connected in series with the device, which allows for

much faster ($\sim 10^9$ samples/s) data acquisition. The light source has to be modulated ON and OFF with a frequency less than $1/\tau$, where τ is the response time of the device. The 6λ laser system can be modulated digitally; a TTI TGA1241 arbitrary waveform generator is used to rapidly switch the laser ON and OFF with frequency < 40 MHz. Light sources that cannot be digitally switched are instead modulated mechanically using a Bentham 218F variable frequency optical chopper.

4.8.3   Photoresponsivity

Photoresponsivity measurements of devices are performed using the procedure for photocurrent measurements (**Section 4.8.1**). A fixed wavelength of light is used at different powers to characterise the power dependence. Neutral density filters are used to control the power of the laser, which is measured using a Thorlabs PM100D power meter and S120VC UV-extended ($200 - 1100$ nm) silicon photodiode. For measurements in the UV range, Edmund Optics UV-Vis neutral density filters were acquired. These filters offer a uniform power reduction in the range $250 - 700$ nm.

4.8.4   Spectral response

A Horiba SPEX or Horiba microHR monochromator is used to split white light into a continuous, angle-dependent spectrum, and is therefore a powerful tool for probing the spectral response of a photosensitive device. A high power (Newport quartz tungsten halogen or Ushio xenon arc) lamp is used as a broadband white light source, which is directed into the entrance slit of the monochromator (**Figure 4.11**). The monochromator works initially by collimating the white light source using a collimating mirror and then directing the collimated beam onto a diffraction grating. A diffraction grating with spacing, g, deflects light at discrete
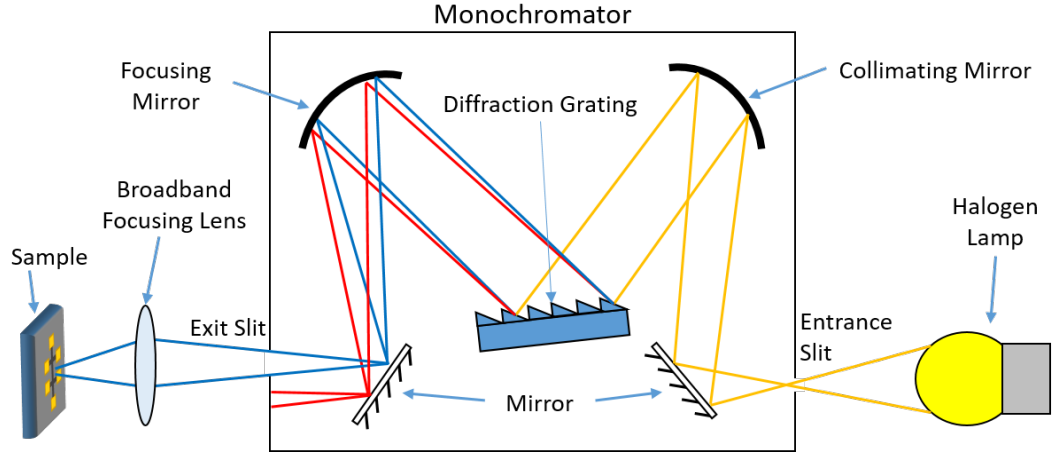
Figure 4.11. Diagram of the inner workings of a monochromator used for wavelength selective photocurrent measurements.

angles, θ, from the surface normal of the grating according to the grating equation,

$$g \sin \theta = n\lambda. \tag{4.3}$$

The angle of deflection is dependent upon the wavelength, λ, and the order of principal maxima, n. Thus, from **Equation 4.3** it is clear that for a given order, n, different wavelengths of light will exit the grating at different angles.

The light continues onto a focusing mirror before it exits the monochromator, where it is focused onto the photosensitive device using a broadband UV-capable focusing lens. A mechanical motor is used to control the angle of the diffraction grating, resulting in precise control of the narrow band wavelength of light emitted out of the exit slit. The width of the exit slit can be changed to control the width of the wavelength range emitted; a narrower slit means a narrower wavelength band of light, but also lower intensity.

5 Hybrid perovskite NC/graphene UV-Vis photodetector

This chapter reports on transport and optoelectronic properties of graphene field effect transistors (FETs) functionalised with all-inorganic perovskite nanocrystals (NCs). Hybrid photon detectors of this type exhibit high photoresponsivity and spectral response tuneable by the band gap of the NCs. Thus, hybrid perovskite NC/graphene devices present a promising route for engineering photodetectors with response in the UV and/or visible range. Transport and optoelectronic characterisation of these hybrid devices were carried out following the procedures described in **Sections 4.7 and 4.8**.

The work included in this chapter is published in *Cottam et al.*, "Defect-Assisted High Photoconductive UV–Visible Gain in Perovskite-Decorated Graphene Transistors" in *ACS Appl. Electron. Mater.*, **2**(1) 147-154 (2020) [120].

5.1 Introduction

Graphene-based photodetectors are highly attractive due to graphene's ultrafast wide-band spectral response throughout the UV-Vis-IR range. However, due to its 2D nature it is limited by intrinsically low absorption ($\sim 2\%$ [177]) and low photoresponsivity on the order of ~ 10 mA/W [141, 152, 178]. Functionalisation of planar graphene FETs is one of many routes being explored with the aim of improving on the limited optical properties of graphene, whilst maintaining its intrinsically high carrier mobility and response times. Previous work includes functionalisation of graphene with II-VI or IV-VI QDs, for example, CdSe, CdS and PbS [79, 144, 145, 179], which achieve high photoresponsivity, $R \approx 10^9$ A/W [79]. This enhanced photoresponsivity is explained by a photoconductive gain effect, whereby charges trapped in the QDs with lifetimes ~ 1 s act as local gates,

generating more carriers in the graphene conductive channel [179]. In more recent literature, this effect has been achieved using organic [147, 151] and inorganic [20] perovskite NCs on graphene, with photoresponsivities of $R \approx 10^9$ A/W [151] and 10^6 A/W [20], respectively.

Here, we study the optoelectronic properties of graphene decorated with a layer of inorganic caesium lead halide NCs (CsPbX$_3$, where X = Br or I). These hybrid devices have electrical and optical properties significantly different from those of pristine graphene or those decorated with traditional colloidal semiconductor NCs [79, 180].

5.2 Perovskite NCs and their optical and electrical properties

Caesium lead halide perovskite NCs capped with a mixture of oleic acid (OA), oleylamine (OLA), and iminodibenzoic acid (IDA) ligands were synthesised following the method outlined in **Section 4.4** (**Figure 5.1a**). The NCs were imaged using transmission electron microscopy (TEM) and high resolution (HR)
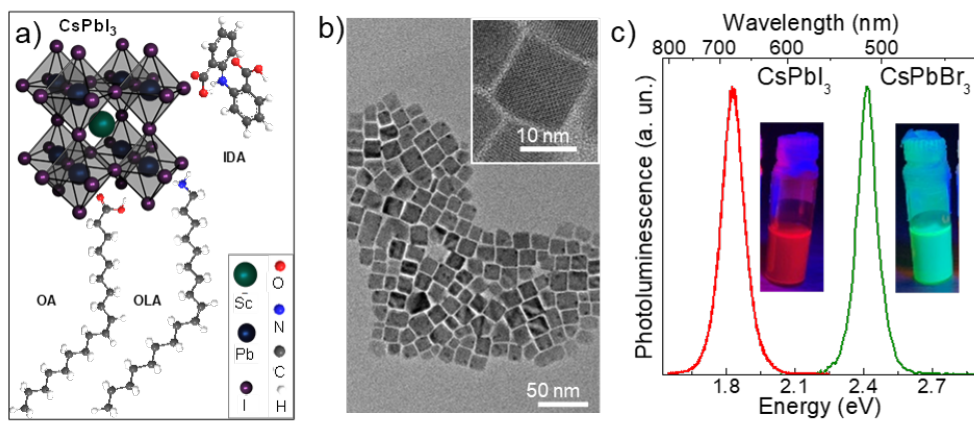
Figure 5.1. **a)** A schematic diagram of the unit cell of CsPbI$_3$ NCs capped with a mixture of OA, OLA and IDA ligands. Credit: Dr. Chengxi Zhang. **b)** Representative TEM and HRTEM images of CsPbI$_3$ NCs. **c)** PL spectra of CsPbBr$_3$ and CsPbI$_3$ perovskite NCs and corresponding images of the NCs excited by unfocused UV light ($\lambda = 365$ nm).

TEM, as described in **Section 4.5.1**, which revealed a cubic shape of the NCs with an average size of 12.9 ± 1.7 nm (**Figure 5.1b**). The composition of the NCs was adjusted to tune their optical properties, such that $CsPbI_3$ and $CsPbBr_3$ NCs emit light at wavelengths of $\lambda = 680$ nm and 515 nm, respectively (**Figure 5.1c**).

The conductivity of the $CsPbI_3$ NC film was investigated before its use in a hybrid photodetector device. The perovskite NC film was deposited on a pre-patterned interdigitated gold contact device with large area and distance of 10 μm between gold contacts (**Figure 5.2a**). The current through the NCs, I_{sd}, was measured as a function of the applied source-drain voltage, V_{sd}, for 3 different gate voltages, $V_g = 0, +60$ and -60 V (**Figure 5.2b**). The resistance of the NCs was
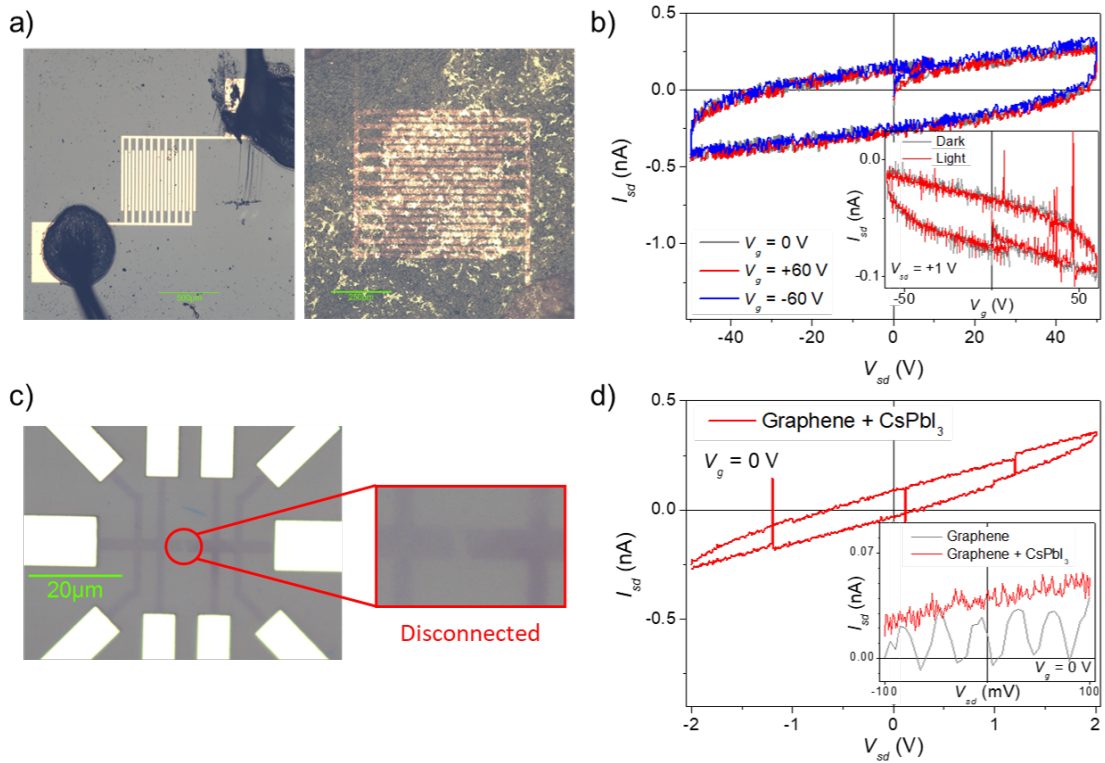
Figure 5.2. a) Optical images of a gold plated 2-terminal device on 300nm SiO_2/Si substrate with contact gap 10 μm before (left) and after (right) perovskite NC deposition. **b)** Source-drain current versus voltage through the 2-terminal device decorated with $CsPbI_3$ NCs at different gate voltages. Inset: current versus gate voltage in the dark and under illumination ($P \sim 10$ mW, $\lambda = 633$ nm). **c)** Optical images of a 'split' Hall bar with gap width ~ 1 μm. **d)** $I_{sd}(V_{sd})$ characteristics of the 'split' Hall bar device before (inset) and after deposition of $CsPbI_3$ NC film.

found to be $R_{NC} > 10$ GΩ. The device was also measured under illumination using a high power red laser ($P \sim 10$ mW, $\lambda_{\mathrm{ex}} = 633$ nm) and no change of resistance was observed (inset of **Figure 5.2b**). To ensure that the contact material was not preventing charge transfer and to reduce the size of the gap between the contacts, we also examined the resistance of the NC film using graphene contacts. A 'split' graphene Hall bar device with ~ 1 μm gap in the centre (**Figure 5.2c**) was used for this test. No significant difference was observed in the $I_{sd}(V_{sd})$ characteristics measured before and after deposition of the perovskite NCs (**Figure 5.2d**), thus, confirming that the resistance of the perovskite NC film is $R_{NC} > 10$ GΩ per square.

Since there are no measurable changes of I_{sd} under illumination ($\lambda = 633$ nm, $P = 10$ mW/mm^2) and under applied gate voltages ($V_g = \pm 60$ V) in either device, we conclude that there is no charge transfer between individual NCs. Hence, we propose that only charge carriers from the layer of NCs directly adjacent to the graphene can be transferred to the graphene channel. For optimised and uniform photon detection performance, it is imperative to fully cover the graphene channel with a uniform single layer of NCs.

5.3 Electrical properties of perovskite decorated graphene transistors

CVD-grown single layer graphene (SLG) from Graphene Supermarket [71] was placed on a hBN/SiO$_2$/Si substrate (285 nm SiO$_2$ layer thickness and mono-layer of hBN) to make a graphene field effect transistor. The structures were processed (see **Section 4.1**) into two device geometries: Hall bars for measurements of carrier concentration and mobility (**Figure 5.3a**) and two-terminal diodes with short (~ 5 μm) channels for optoelectronic characterisation (**Figure 4.1b**). The devices were bonded following the procedures described in **Section 4.3** before
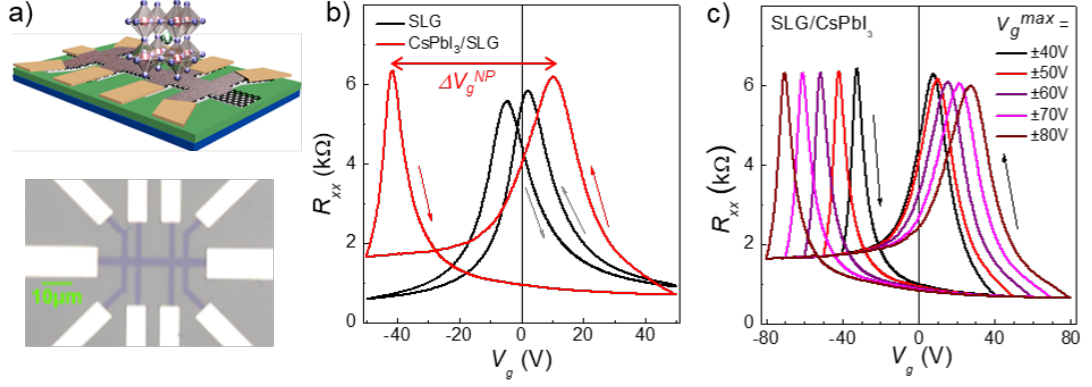
Figure 5.3. a) A schematic diagram of the layer structure (top) and optical microscopy image (bottom) of the Si/SiO$_2$/hBN/graphene/perovskite Hall bar device. **b)** Room temperature dependence of the longitudinal resistance, R_{xx}, on applied gate voltage, V_g, of a pristine graphene device and of the same device after deposition of the CsPbI$_3$ NCs. Arrows indicate directions of the V_g sweeps (sweep rate = 0.3 V/s, T = 295 K). The top horizontal arrow represents the size of the hysteresis ΔV_g^{NP}. **c)** R_{xx} as a function of the maximum applied gate voltage, V_g^{max}, for a series of sequential V_g sweeps with V_g^{max} increasing from 40 to 80 V (sweep rate = 0.3 V/s, T = 295 K).

being mounted in a vacuum cryostat for electrical measurements, as described in **Section 4.7.1**. The vacuum is important for keeping the device in a stable condition by limiting any interaction with air molecules and moisture. High vacuum also improves the stability of the gate meaning that higher gate voltages can be applied without current leakage through the gate. The gate voltage characteristics of pristine graphene and perovskite-decorated graphene devices are compared in **Figure 5.3b**. The pristine SLG device has a resistance maximum $R_{xx} \approx 6$ kΩ close to $V_g = 0$ V and exhibits only a small hysteresis loop, which is quantified in terms of the difference in the gate voltage value at the charge neutrality (Dirac) point, $\Delta V_g^{NP} \approx 5$ V, between the forward (from negative to positive bias) and reverse sweeps of V_g (**Figure 5.3b**). The pristine SLG devices have a low electron carrier concentration of $n \approx 2 \times 10^{11}$ cm^{-2} at $V_g = 0$ V and carrier mobility $\mu_e \approx 6000$ cm^2/Vs at room temperature, as calculated using the field effect model (**Section 3.1**).

The perovskite NCs were deposited onto CVD-grown graphene by drop cast-
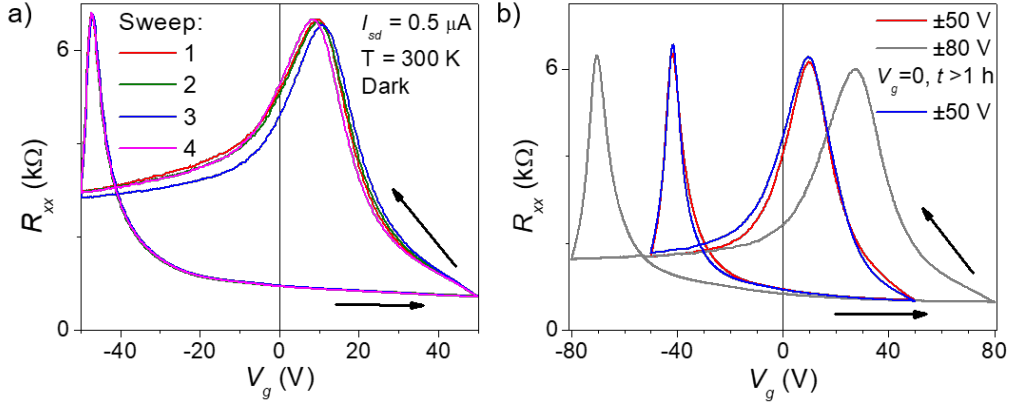
Figure 5.4. **a)** $R_{xx}(V_g)$ dependence of four consecutive gate voltage sweeps from $+50$ V to -50 V and back in the dark ($I_{sd} = 0.5$ μA, $T = 300$ K, sweep rate $= 0.3$ V/s). **b)** Three consecutive voltage sweeps to $V_g^{max} = \pm 50$ V, ± 80 V and ± 50 V with the device kept at $V_g = 0$ V for 1 h between the grey and blue curves.

ing, as described in **Section 4.6**. The deposition of NCs causes a shift in the average position of the Dirac point towards further negative voltages by ~ 15 V and an increase of the hysteresis of the charge neutrality point. We define the average position of the Dirac point as the V_g value that is halfway between the forward and reverse Dirac points. The hysteresis of $R_{xx}(V_g)$ is strongly affected by the maximum applied gate voltage V_g^{max} (**Figure 5.3c**). As shown in **Figure 5.3b** for a representative SLG/CsPbI$_3$ device, a hysteresis of $\Delta V_g^{NP} \approx 60$ V is observed for a gate voltage sweep over the range of $\Delta V_g^{max} = \pm 50$ V, at room temperature. The value of the hysteresis increases with increasing V_g^{max} and reaches unexpectedly high values above 100 V for a sweep range of $V_g^{max} = \pm 80$ V (**Figure 5.3c**). The observed dependence of the ΔV_g^{NP} on V_g^{max} and the large hysteresis indicate that the NC layer is accumulating a significant amount of charge density ($> 8 \times 10^{12}$ cm^{-2}). Due to the large hysteresis, it is not possible to define an exact value of the V_g^{NP} for the perovskite decorated layer; hence change of carrier concentration in the SLG due to surface doping effect of the perovskite NCs cannot be assessed quantitatively using the 1C model (**Section 3.1**). The hysteresis is reproducible across all SLG/perovskite NC devices tested (see **Section 7.3**) and the overall device performance was confirmed to be fully reproducible and reversible, see **Figure**

5.4. The stability of the device over a number of sweeps is shown in **Figure 5.4a** with almost perfect reproducibility for the forward sweep and some small (<3 V) variation of the Dirac point position on the reverse sweep. The reversibility of the device is shown in **Figure 5.4b** as the maximum gate voltage was increased from $V_g^{max} = \pm 50$ V to $V_g^{max} = \pm 80$ V and after 1 h at $V_g = 0$ V the device returned back to the same behaviour for $V_g^{max} = \pm 50$ V, i.e. the blue and red curves have insignificant differences.

5.4 Temperature dependence of charge transfer

The observed ΔV_g^{NP} hysteresis is strongly temperature-dependent (**Figure 5.5a**). The $R_{xx}(V_g)$ dependence of SLG/CsPbI$_3$ Hall bar devices was measured in the range of temperatures from 2 K to 350 K. The size of the hysteresis decreases with decreasing temperature and quenches at $T \approx 200$ K, where the $R_{xx}(V_g)$ characteristics resemble those of pristine graphene, indicating that no charge transfer is taking place at $T < 200$ K. At $T > 320$ K, a significant broadening of the forward/reverse loop is observed. This is likely due to the instability of perovskite NCs at high T, which is also evident in the irreversible decrease of room temperature PL intensity following exposure of the NCs to $T > 400$ K. It is noted that the room temperature optical properties of the NCs, such as PL, are not significantly affected by exposure to temperatures in the range from $2 < T < 400$ K. This leads to the conclusion that the dramatic $\Delta V_g^{NP}(T)$ dependence is related to the charge transfer between the NC layer and the SLG, rather than the temperature-dependent properties of the perovskite NCs.

The dependence of the ΔV_g^{NP} hysteresis on temperature in the range 200 K $< T <$ 300 K has an exponential form and is well described by $\Delta V \approx \exp(-E_x/kT)$, with activation energy of $E_x = 0.3$ eV. This activation energy has the same value for both CsPbI$_3$ and CsPbBr$_3$ NCs (**Figure 5.5c**), suggesting the presence of a common deep energy level defect, see inset of **Figure 5.5c**.
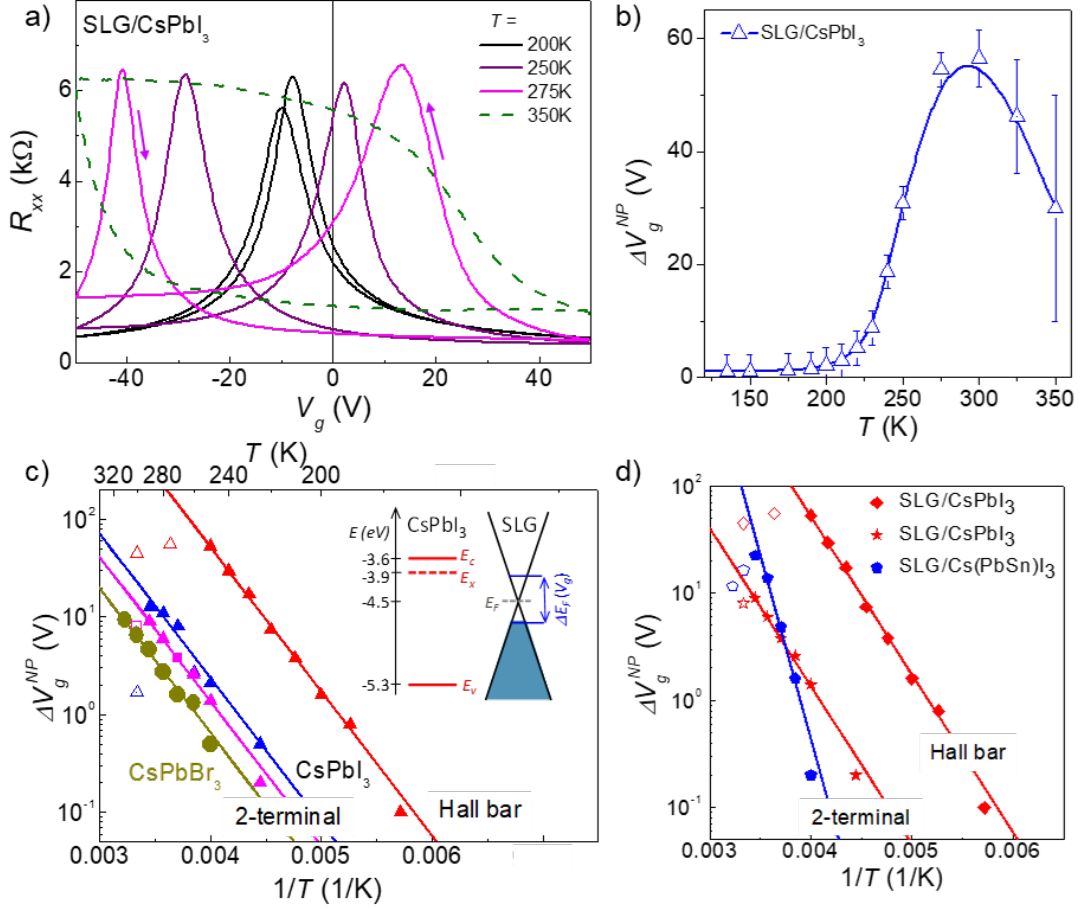
Figure 5.5. **a)** $R_{xx}(V_g)$ dependences of the SLG/CsPbI$_3$ device measured at different temperatures. **b)** Temperature dependence of ΔV_g^{NP} of the SLG/CsPbI$_3$ device in a). **c)** Data points: ΔV_g^{NP} as a function of temperature for a Hall bar CsPbI$_3$/SLG device (red triangles) and three 2-terminal devices: two CsPbI$_3$/SLG devices (blue and magenta triangles) and one CsPbBr$_3$/SLG device (yellow circles). Solid lines represent a fit with $\Delta V_g^{NP} \approx \exp(-E_x/kT)$ with $E_x = 0.3$ eV. Inset: Band diagram of the CsPbI$_3$/SLG heterostructure. The blue arrow indicates a region where graphene Fermi energy, E_F, is changed by the applied gate voltage. The red dashed line denoted E_x represents the energy level of charge trapping defects. **d)** Temperature dependence of ΔV_g^{NP} of representative SLG/CsPbI$_3$ and SLG/Cs(PbSn)I$_3$ devices. The red diamonds represent a Hall bar device and the red stars and blue pentagons represent 2-terminal devices.

However, the activation energy for Cs(Pb$_{0.67}$Sn$_{0.33}$)I$_3$ NCs is significantly larger, $E_x = 0.6$ eV (**Figure 5.5d**). Thus, it is inferred that these defect energy levels correspond to Pb-related defects, which were recently reported to account for PL intermittency in caesium lead halide NCs [116]. In order to understand the nature of the ΔV_g^{NP} hysteresis, the 2C model (see **Section 3.2**) was applied.

5.5 Modelling of charge transfer in perovskite decorated graphene transistor

A small hysteresis of $R_{xx}(V_g)$ is typically observed in gated SLG devices and usually associated with the gate capacitance and/or charging of impurities [27, 181]. In pristine SLG devices, the width of the hysteresis is usually very small (**Figure 5.3b**) and is independent of the V_g sweep range (V_g^{max}). In perovskite-decorated SLG we observe an anomalously large hysteresis, ΔV_g^{NP}, dependent on V_g^{max} and temperature, which is not observed in other hybrid graphene heterostructures [36, 145, 182]. However, a smaller hysteresis in V_g has recently been shown to arise from a ferroelectric memory effect when graphene is coupled to a ferroelectric material such as In_2Se_3 [183], suggesting that the observed effect is not unique to just perovskite NCs. For our system it is thought that the slow V_g-dependent charge transfer between the NCs and SLG results from charge accumulation in the NC layer.

5.5.1 Applying the 2C model

Applying the 2C model introduced in **Section 3.2**, the presence of the top perovskite layer significantly changes the charge distribution of the FET. In this numerical model, the $CsPbI_3/SLG/SiO_2/Si$ device is treated as a double capacitor (2C model): the first capacitor is that of the $Si/SiO_2/SLG$ layers and the second capacitor is the 'effective' capacitance of a layer of perovskite NCs (**Figure 5.6a**). In this case, the electric field penetrates through the graphene layer inducing a charge, Q_{per}, in the perovskite NC layer directly adjacent to the SLG. This charge can drain through the SLG layer following a change of V_g, but is limited by the charge transfer time associated with the perovskite NCs. The perovskite NC layer behaves effectively as an additional capacitor that can hold a high density of charges ($> 10^{12}$ cm^{-2}). This assumption is validated by our measurements of
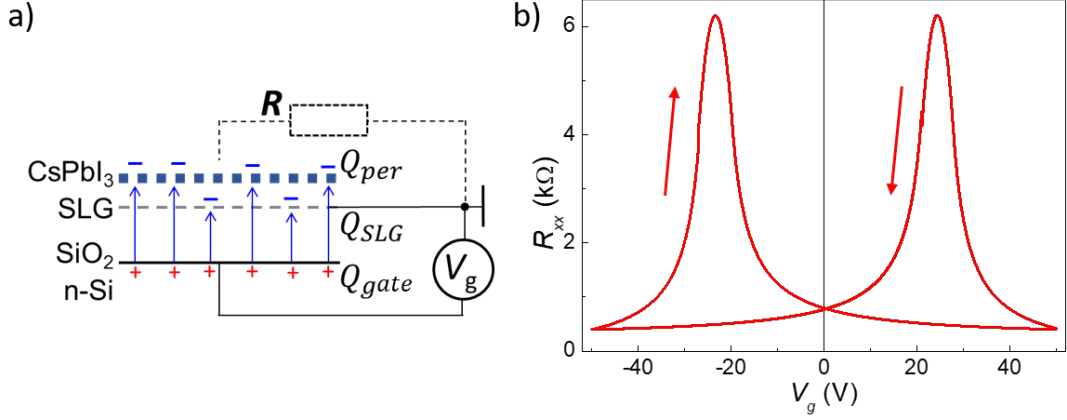
Figure 5.6. **a)** Schematic of the 2C model setup and distribution of charge between the perovskite layer, Q_{per}, the graphene layer, Q_{SLG}, and the gate, Q_{gate}. **b)** Numerical model of the dependence of resistance on gate voltage for graphene functionalised with perovskite NCs (sweep rate 0.3 V/s). Arrows indicate gate voltage sweep direction.

$V_g = \pm 80$ V for the perovskite/graphene device as it appears to be far from the limit of maximum charge storage (see **Figure 5.3c**).

The dynamics of the perovskite layer charging is numerically modelled as described in **Section 3.2** using $C_0 = 115$ μF/m^2 as the capacitance of the Si/SiO$_2$/SLG capacitor; this is for an oxide layer thickness of 285 nm, which is applicable for most of the FETs modelled. The graphene resistance is calculated as,

$$R_{xx} = \frac{1}{Q_{SLG}\mu},\tag{5.1}$$

where the room temperature carrier mobility, $\mu = 6000$ cm^2/Vs, is obtained from field-effect measurements, thus allowing us to plot $R_{xx}(V_g)$ (**Figure 5.6b**). The variation of $R_{xx}(V_g)$ near its maximum at the charge neutrality (Dirac) point, V_g^{NP}, is modelled as a parabola,

$$R_{xx} \approx R_{xx}^{max} - (V_g - V_g^{NP})^2,\tag{5.2}$$

with the maximum $R_{xx}^{max} = 6.2$ kΩ from experimental data (**Figure 5.3b**).

The resistance of the NC layer is very high (>10 GΩ; see **Figure 5.2**) and

charge transfer between neighbouring NCs is negligible. In this model only charge transfer from the layer of NCs adjacent to the SLG is considered; the only fitting parameter is the time constant, τ_{per}, which describes the rate at which the charge in the perovskites changes.

5.5.2   Results of the 2C model fitting

The numerical calculations of the $R_{xx}(V_g)$ hysteresis at different V_g^{max} (**Figure 5.7a**) demonstrate a behaviour similar to that observed experimentally (**Figure 5.3c**). By fitting the measured $\Delta V_g^{NP}(V_g^{max})$ dependences by means of the 2C model (**Figure 5.7b**), we obtain a good agreement between the experimental data and numerical simulations with a value of the fitting parameter $\tau_{per} = 130$ s. However, the symmetric behaviour with respect to positive/negative V_g predicted by this model is not fully consistent with the measured data. The experimental results (**Figure 5.3c**) revealed a weaker hysteresis at positive V_g. This discrepancy is attributed to the assumption used in the model that disregards which capacitor plate, bottom gate or top SLG with NCs plate, has positive/negative polarity. In the real device, the charging of the top plate of the capacitor (SLG
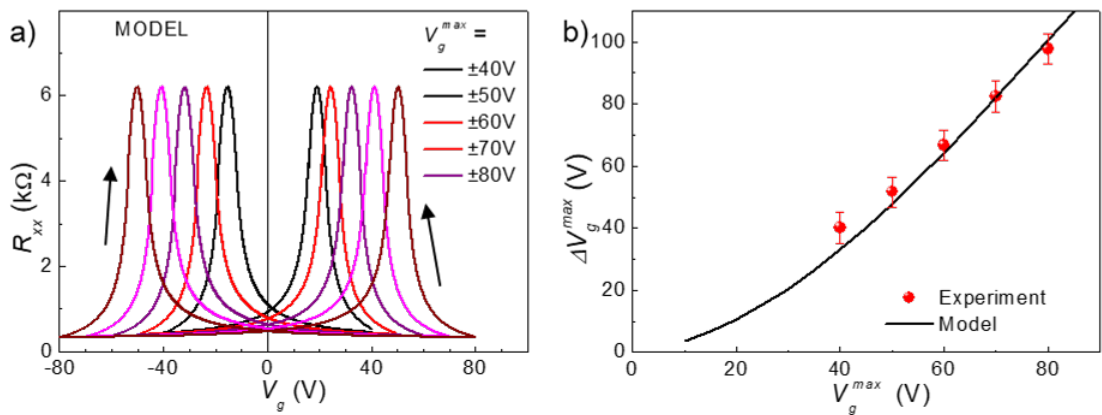
Figure 5.7. a) Results of the numerical simulation using the 2C model of $R_{xx}(V_g)$ with increasing V_g^{max}. The fitting parameter used is $\tau_{per} = 130$ s. Arrows indicate direction of V_g sweep. **b)** Measured values of ΔV_g^{NP} (red data points) as a function of the V_g^{max} from **Figure 5.2c**. The solid line is a fit based on the 2C model with $\tau_{per} = 130$ s.

with NCs) can be dependent on the polarity of the applied gate voltage, as it shifts the Fermi energy in the SLG, over the range ± 0.3 eV for ± 100 V. Note that this energy is similar to the activation energy of the perovskite defect responsible for the temperature behaviour (see **Figure 5.5** and relevant text in **Section 5.4**).

The gate voltage sweep generates an incremental increase in charge $\Delta Q = C\Delta V_g$ on the top of the perovskite/SLG electrode corresponding to the sum of free carrier charge (electrons or holes) in the SLG and the charge bound to the localised states of the NCs, with activation energy, E_x. It is assumed that most of this charge is stored in the NC layer and is slowly released into the SLG (with an effective time constant of ~ 100 s). The charge capacitance of the perovskite NC layer is estimated from the measured position of the SLG neutrality point hysteresis, $\Delta V_g^{NP} > 100$ V, to be greater than 7×10^{12} cm^{-2} (see **Figure 5.3c**). The NC density is estimated to be approximately 4×10^{11} cm^{-2}. This is assuming that the average size of the CsPbI$_3$ NCs with ligands included is $d_{\text{eff}} \approx 15$ nm [24] and the surface filling factor is approximately 1, meaning that the NCs completely cover the SLG surface in an ordered arrangement (see TEM images in **Figure 5.1b**). Hence, the number of individual charges per single NC adjacent to the SLG must be greater than 10. It is estimated that a perovskite NC contains ~ 400 of CsPbX$_3$ unit cells, each containing a single Pb atom, per one side of a NC cube, thus providing an extremely large maximum charge capacity, limited only by Coulomb repulsion of the charges within the perovskite NC.

The electrostatic energy which arises when $N = 10$ electrons are accommodated within a single perovskite NC is estimated using the expression,

$$U = \frac{3}{5}\frac{e^2 N^2}{4\pi\epsilon\epsilon_0 r},\tag{5.3}$$

where $r = 7$ nm is an effective radius of a NC and $\epsilon = 10$ is the dielectric constant of CsPbI$_3$ [184]. The estimated value is $U \approx 0.6$ eV, which is significantly lower than the CsPbI$_3$ work function of ~ 3.6 eV [185]. Accumulation of such a large

amount of charge in a single NC should result in a high internal electric field affecting NC electronic properties and energy states. This effect is explored and discussed in detail in **Chapter 6**.

The large number of charges trapped within a single perovskite NC is responsible for the anomalously large ΔV_g^{NP} hysteresis and slow charge transfer processes. Furthermore, the developed model is in good agreement with the observed dependence of hysteresis ΔV_g^{NP} on the applied gate voltage (**Figure 5.7b**). A similar charge transfer between SLG and an adjacent dielectric layer was recently reported in SiC/SLG [186] and in InSe/graphene [36, 187] heterostructures. In both heterostructures, the Fermi level in SLG is pinned to the energy level of the ionised donor impurities in the adjacent SiC or InSe dielectric layer. However, in contrast to our perovskite-decorated devices, no large temperature or V_g sweep range dependence of the pinning effect was reported for those devices [36, 186, 187]. This suggests that the charge transfer processes in the 0D/2D CsPbI$_3$/SLG hybrid devices are significantly slower than those in 2D/2D heterostructures, likely due to the potential barrier introduced by the ligands surrounding the NCs, which is absent in 2D/2D heterostructures like InSe/graphene [187].

5.6 Light-induced charge transfer and photoresponsivity

The properties of perovskite NC decorated SLG are strongly affected by exposure to light. The shift of V_g^{NP} toward negative values under light illumination (**Figure 5.8a**) indicates a transfer of photoexcited electrons from the perovskite NCs into the graphene (**Figure 5.8b**), similar to that reported previously for quantum dot decorated SLG [79, 144, 180] and other perovskite NC decorated structures [103]. This behaviour is in contrast to the transfer of photoexcited holes suggested for organic-inorganic mixed-cation lead mixed-halide perovskite deposited on similar CVD graphene/SiO$_2$/Si substrates [19]. A significant reduction of the hysteresis under light illumination was observed, with V_g^{NP} shifting to
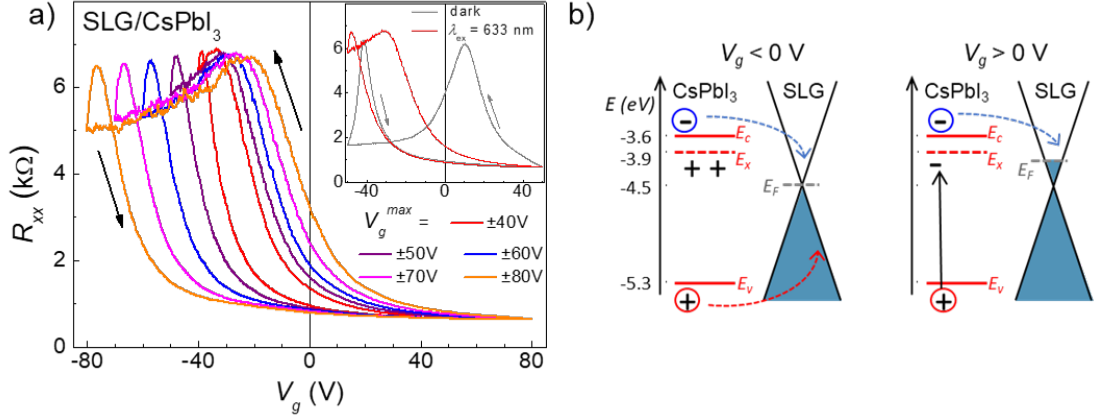
Figure 5.8. **a)** R_{xx} as a function of the applied gate voltage, V_g, for a series of sequential V_g sweeps with V_g^{max} increasing from ± 40 to ± 80 V, under excitation with a HeNe laser ($\lambda_{ex} = 633$ nm, $P = 310$ W/m^2). Inset: comparison of $V_g^{max} = \pm 50$ V sweep in the dark and under laser light. **b)** A schematic diagram of the CsPbI$_3$/SLG band structure. Arrows indicate transfer of photoexcited charges from perovskites to the SLG (dashed blue and red arrows) for negative (left) and positive (right) gate voltages. The vertical black arrow indicates recombination of photo-generated holes with negative charge stored in the perovskite layer.

more negative V_g values. The forward V_g sweep section of the $R_{xx}(V_g)$ curves are similar for both light and dark conditions (inset in **Figure 5.8a**). This is likely due to the fact that we are unable to sweep the gate voltage to larger negative values without significant risk of breaking the SiO$_2$ layer and so the forward sweep V_g^{NP} becomes pinned close to the value of $-V_g^{max}$. The reverse sweep direction was most affected with V_g^{NP} becoming less dependent on the maximum sweep value, V_g^{max}. This behaviour can be explained by the effect of illumination on the charges trapped on the perovskite NCs. The light generates electron–hole pairs in the NCs and the photoexcited electrons are transferred to the SLG, while the less mobile photoexcited holes remain trapped in the NCs. This difference in relaxation times of photoexcited electrons and holes leads to the asymmetry of the $R_{xx}(V_g)$ shown in **Figure 5.8a**. Here it is assumed that photoexcited holes can recombine with gate-induced negative charges in the perovskite NCs (**Figure 5.8b**). The V_g-dependence of the resistance indicates the transfer of both photoexcited electrons and holes for $V_g < 0$ V, and the preferential transfer of photoexcited electrons for $V_g > 0$ V (**Figure 5.8b**).

The macroscopic 2C model (**Section 5.5**) also could be used for these experimental findings. The effect of light on the charge dynamics can be described in terms of a significant reduction of the τ_{per} parameter under illumination at the applied positive V_g. Under negative V_g conditions, photoexcited holes do not interact with positive gate-induced charge, leading to insignificant changes in the $R_{xx}(Vg)$ hysteresis measured under dark and light conditions (see inset of **Figure 5.8a**).

The SLG/perovskite devices are photosensitive over the wavelength range of optical absorption of the used NCs. The photocurrent spectrum, measured using a monochromator as described in **Section 4.8.4**, resembles that of the NC optical absorption (**Figure 5.9a-b**): it follows quite closely that of absorbance. Also, a large photocurrent is observed in the UV region ($\lambda < 400$ nm). Pristine graphene has a small optical absorbance ($\sim 2\%$) and consequently its photoresponsivity is very low ($R < 0.1$ A/W). Hence, the optical response of these SLG/perovskites hybrid devices is predominantly due to the optical absorption of the perovskite NCs and by the charge transfer between the NC layer and graphene. The SLG devices decorated with both types of perovskite NCs ($CsPbBr_3$ and $CsPbI_3$) have very high photoresponsivity of $R > 10^6$ A/W for all excitation wavelengths measured in the UV-Vis range ($250 - 633$ nm) at room temperature (**Figure 5.9c**). The highest photoresponsivity $R \approx 5 \times 10^6$ A/W is observed in the low power limit where the photocurrent approaches the noise equivalent power, NEP $\approx 10^{-14}$ W. The responsivity achieved in our work exceeds that recently reported for SLG devices decorated with similar perovskite NCs [20, 188], particularly in the UV range. With increasing excitation power, the photoresponsivity decreases as $R \sim P^{-x}$, where $x = 0.90 \pm 0.02$ (**Figure 5.9c**), which is similar to that reported for $CsPbCl_3$ [20] and for colloidal quantum dots e.g. PbS [79].
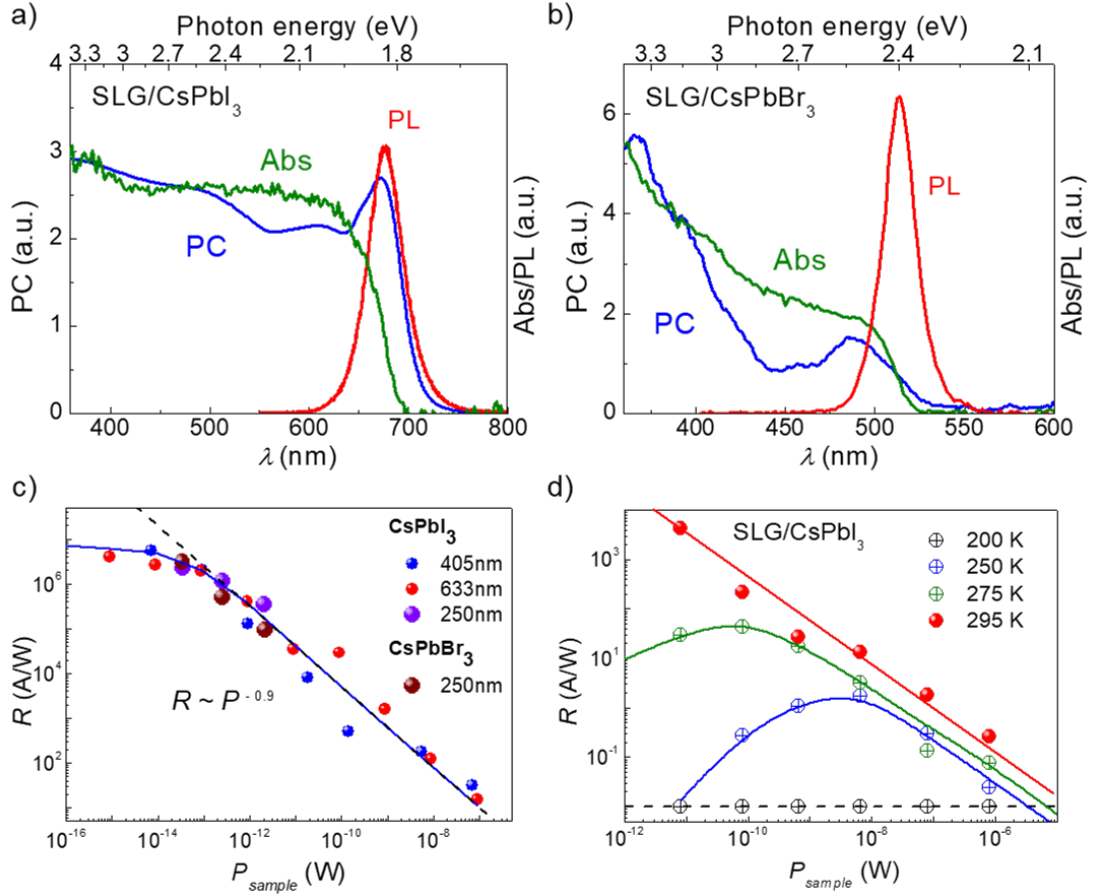
Figure 5.9. Room temperature absorption (Abs) and photoluminescence (PL) spectra of perovskite NCs and photocurrent (PC) measurements of SLG devices decorated with these NCs for **a)** $CsPbI_3$ and **b)** $CsPbBr_3$ NCs. **c)** UV-Vis photoresponsivity of $CsPbI_3$/SLG and $CsPbBr_3$/SLG devices at $\lambda_{ex} = 633, 405$ and 250 nm. The dashed line is a fit using $R \sim P^{-0.9}$. The blue line is a guide to the eye. **d)** Photoresponsivity of $CsPbI_3$/SLG at different temperatures measured in the power range 10^{-11} W $< P < 10^{-6}$ W ($\lambda_{ex} = 633$ nm). The dashed line represents the level of noise.

The temperature dependence of the responsivity power law was examined for power on the sample, $P_{sample} > 10^{-11}$ W. As is shown in **Figure 5.9d**, with decreasing temperature a deviation from the power law dependence is observed. For example, at $T = 250$ K, the power dependence of the responsivity is described by $R \sim P^{-0.9}$ only up to $P = 10^{-9}$ W. At $T = 200$ K, the responsivity decreases, reaching a value of $R < 1$ A/W, which is similar to that of pristine graphene. This observation corroborates the measurements of the temperature dependence of the gate voltage-induced hysteresis ΔV_g^{NP} in **Section 5.3**, where at $T < 200$

64

K, no effect of the NC layer on the electrical properties of graphene was observed (**Figure 5.5a**). The observed temperature dependence of $R(P)$ is attributed to the interplay of two opposing effects: the $R \sim P^{-0.9}$ dependence of $R(P)$ at the high power range and the fast exponential quench of $R(T)$ at low P. The weaker $R(T)$ dependence at large excitation power can be ascribed to the heating of the device. At low excitation powers ($P < 10^{-8}$ W) and low temperatures ($T < 250$ K) charge transfer between the NCs and graphene appears to be blocked. This results in quenching of both the photoresponsivity, R, and the gate voltage hysteresis, ΔV_g^{NP}. Since the NCs are still photoluminescent at $T < 200$ K [106], meaning that electron-hole pairs are generated in the perovskite NCs at any temperature, it is clear that the photoresponse of the NC/SLG device is controlled by the temperature dependent charge transfer between the NCs and SLG.

5.7 Temporal response of perovskite/SLG devices

The temporal response of the device following optical excitation is shown in **Figure 5.10a**. The observed exponential decay of the resistance has characteristic times of ~ 1 s. The relaxation of the charge generated by applied gate voltage has a significantly slower decay time of ~ 100 s (**Figure 5.10b**). This difference is ascribed to the relaxation of fast optically excited, high energy charge carriers compared to slow gate voltage induced charge transfer. Despite significant differences in the values of the relaxation times, the optical responsivity, R, and gate voltage hysteresis, ΔV_g^{NP}, have very similar temperature dependences (**Figure 5.10c**). This suggests that the processes responsible for the ΔV_g^{NP} hysteresis also define the optical responsivity observed in these materials, that is, both light- and gate-induced charge trapping processes are controlled by the same kind of charge traps with an activation energy $E_x \approx 0.3$ eV, see **Section 5.4**.
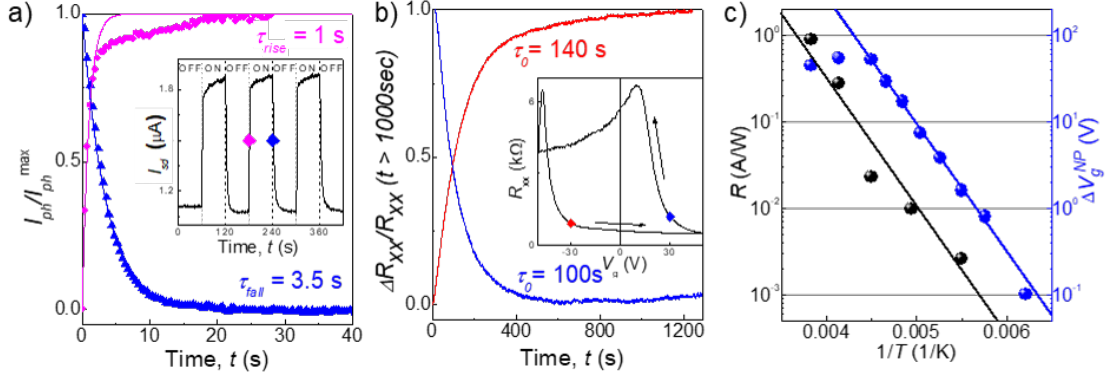
Figure 5.10. **a)** Temporal response of the photocurrent on rising and falling slope (ON/OFF) at point indicated by magenta (ON) and blue (OFF) in the inset for the SLG/CsPbI$_3$ device. Inset: light on/off time dependence of the photocurrent for the SLG/CsPbI$_3$ device at $T = 295$ K ($V_{sd} = 20$ mV, $V_g = 0$ V, $P = 325$ W/m^2, $\lambda_{\text{ex}} = 633$ nm). **b)** Temporal response and (inset) R_{xx} as a function of V_g for CsPbI$_3$/SLG device at the V_g-sweep positions indicated by the red and blue dots (inset), $T = 295$ K, $I_{sd} = 0.5$ μA, sweep rate = 0.3 V/s. **c)** Comparison of $\Delta V_g^{NP}(T)$ (blue) and $R(T)$ (black) dependences of SLG/CsPbI$_3$ device. Solid lines are the fit with $\Delta V \approx \exp(-E_x/kT)$, where $E_x = 0.3$ eV.

The relatively large ratio of the lifetime of photoexcited holes trapped in the NCs, typically $\tau_{NC} > 1$ s, and the electron transit time in the graphene channel, $\tau_e \approx 100$ ns (for $\mu \sim 6000$ cm^2/Vs, $V_{sd} = 20$ mV and channel length, $l = 35$ μm), give rise to high photoresponsivity ($R > 10^6$ A/W at $T = 295$ K) due to high photoconductive gain [20, 79] (see **Section 2.5.2**). The measured response time of ~ 1 s in our devices (**Figure 5.10a**) is comparable to that previously reported for QD-decorated graphene photodetectors [79, 144] and is significantly shorter than that of CsPbCl$_3$/graphene devices without ligand treatment (> 100 s [20]); thus, suggesting that the shorter ligands used in our NCs (IDA replacement described in **Section 4.4**) enable more efficient charge transfer between the NC layer and the SLG, and hence faster response times. The CsPbI$_3$/graphene photodetector reported here has a detectivity, $D^* = 2.3 \times 10^{10}$ Jones, which was calculated using **Equation 2.3** (see **Section 2.5**) for NEP $\approx 10^{-14}$ W, active area, $A = 10^{-10}$ m^2, and response time, $\tau = 3$ s.

5.8 Summary

We have investigated the use of all-inorganic perovskite ($CsPbX_3$) NCs as a photosensitive layer in graphene-based planar photon detectors. These detectors have stable performance and record high photoresponsivity of $R > 10^6$ A/W in the UV–Vis from 250 to 633 nm. The $CsPbX_3$ NC decorated graphene devices exhibit an anomalous charging effect resulting in large hysteresis in the gate voltage dependence of the resistance, $R_{xx}(V_g)$, of ~ 100 V. This hysteresis was described using a developed two-capacitor (2C) model whereby the perovskite NC layer acts as a second capacitor that is able to store charge with an effective RC time, τ_{per}. The model is in good agreement with the observed results for a numerical fitting parameter of $\tau_{per} = 130$ s, which is consistent with the relaxation times measured for the V_g dependence of the device. Later this model was found to be applicable to other material systems, such as graphene functionalised by ferroelectric $CuInP_2S_6$ (CIPS) flakes [172].

The temperature dependence of the optoelectronic and transport properties of these devices have been studied for the first time and reveal a quenching of the device performance in the temperature range below ambient conditions ($T < 250$ K). This phenomenon is consistent with the presence of a deep (~ 0.3 eV) defect level in all $CsPbX_3$ perovskites independent of halide content. The precise nature of this defect level is unknown and requires further studies, but is likely to be associated with the Pb-states as the device consisting of Sn-doped NCs showed a significantly different activation energy (~ 0.6 eV).

We have shown that the photoresponse of $CsPbX_3$/graphene is dominated by the photosensitive layer (perovskite NCs) and as such the absorption range can be controlled through tuning of the band gap of the material used. Thus, these $CsPbX_3$/graphene devices offer a novel route to device engineering the interface properties of hybrid materials and good prospects for the development of

silicon-compatible ultrasensitive UV photon detectors. In particular, these hybrid perovskite/graphene detectors excel in the UV wavelength range with responsivity many orders of magnitude greater than current commercial UV detectors (see **Section 2.5.3**).

6 Fully reversible PL quenching and light-induced Stark effect in perovskite NCs

6.1 Introduction

This chapter reports on the temporal behaviour of the photoluminescence of all-inorganic perovskite NCs under different excitation powers and temperatures. The key result is a fully reversible quenching and red shift of the PL peak position, E_{PL}, of the NCs due to a light-induced Stark effect. The results are modelled using a triangular quantum well (TQW) confinement potential resulting from the electric field created by the accumulation of photo-generated charges onto the surface of the NC. Photoluminescence measurements were performed following the procedures described in **Section 4.5.2**.

Commercial graphene FETs provided by Graphenea [175] were used in this work. The results described in this chapter are published in *Cottam et al.*, "Light-Induced Stark Effect and Reversible Photoluminescence Quenching in Inorganic Perovskite Nanocrystals", *Adv. Opt. Mater.*, **9**, 13, 2100104 (2021) [189].

6.2 Reversible PL quenching in perovskite NCs

In this work we used all-inorganic mixed halide $CsPb(Br:I=2:3)_3$ perovskite NCs with cubic-shape and average size of $l = 14 \pm 3$ nm (**Figure 6.1a,b**), as measured by TEM (**Section 4.5.1**). Similar to the NCs used on the hybrid photodetector in **Chapter 5**, a mixture of OA, OLA, and IDA ligands were used to passivate the NCs, providing high stability and durability. It is generally accepted that the strength of ligand binding and their density on the surface define the quality of passivation of surface defects, which otherwise act as charge traps and reduce quantum yield (QY) [190, 191]. Thus, optimal passivation is required for
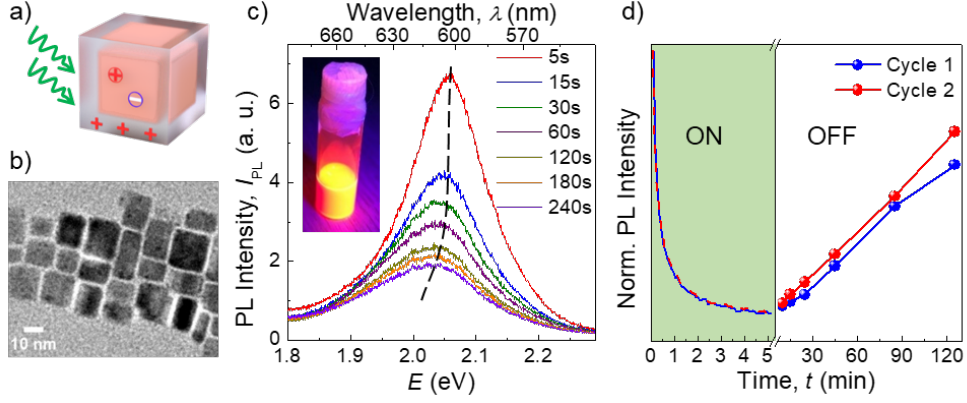
Figure 6.1. a) Sketch illustrating a photoexcited electron and hole pair and positively charged surface defects on a perovskite NC. **b)** A representative TEM image of $CsPb(Br:I = 2:3)_3$ perovskites NCs. **c)** Room temperature PL spectra recorded at different times during sample exposure to laser light ($\lambda_{ex} = 532$ nm, $P = 2$ μW). The dashed line is a guide to the eye and follows the evolution of the PL peak position E_{PL} over time. Inset: optical image of $CsPb(Br:I)_3$ NCs in solution. **d)** Quenching of the PL intensity under continuous excitation power ($P = 2$ μW, exposure time $t < 5$ min) and its recovery, as probed by short laser pulses ($t_{pulse} = 5$ s, $P = 2$ μW, and $t > 5$ min).

improved QY, optical stability and lifetime of the NCs.

The temporal decay of the PL signal was measured, as described in **Section 4.5.2**, by using a continuous wave (CW) laser excitation and recording the PL spectra at regular time intervals, typically every 5 s (i.e. 5 s integration time per spectrum). The recovery of the PL intensity was measured using a pulsed laser mode, whereby the laser was switched on for the minimum time required to acquire the PL spectrum ($t_{pulse} \sim 5$ s). Time intervals of >10 min were used to allow for the PL signal to recover between measurements. For the NC films, upon initial exposure to focused continuous laser light ($\lambda_{ex} = 532$ nm, $P < 2$ mW, laser spot diameter ≈ 5 μm), a slow exponential decay of the PL intensity is observed over time (**Figure 6.1c,d**), with a characteristic decay time, τ_1, of several seconds. The value of τ_1 decreases with the increasing excitation power. We also observe a second, slower temporal decay of the signal with a relaxation time $\tau_2 >> \tau_1$ (see details in **Section 6.3**). The observed PL decay is reversible, although the recovery time is significantly slower (~ 2 hs) (**Figure 6.1d**).

70

6.3 Power dependent evolution of PL emission

The initial PL peak position, E_{PL}, and its full width at half maximum (FWHM) at $t < 10$ s are very similar for all studied laser powers in the range, 20 nW $< P < 200$ μW (**Figure 6.2a**). However, the time evolution of the PL is strongly power dependent and more pronounced for high laser power exposures (**Figure 6.2a** and **Figure 6.3a-c**).
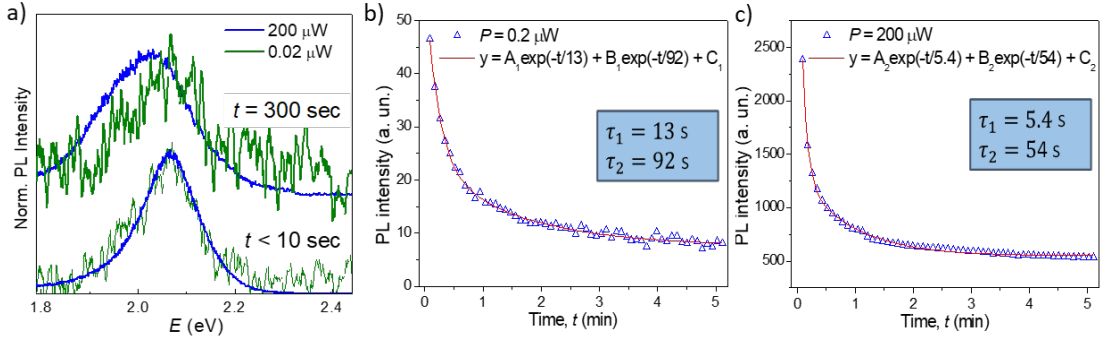
Figure 6.2. a) Representative PL spectra at two different powers taken at $t < 10$ s and $t = 300$ s, recorded at room temperature with PL excitation wavelength, $\lambda_{\mathrm{ex}} = 532$ nm. Bi-exponential fit of the PL decay measured for CsPb(Br:I=2:3)$_3$ NCs at an excitation power of **b)** $P = 0.2$ μW and **c)** $P = 200$ μW.

The measured PL decay can be well fitted using a bi-exponential decay function (**Figure 6.2b,c**),

$$y = A_1 \exp\left(-\frac{t}{\tau_1}\right) + B_1 \exp\left(-\frac{t}{\tau_2}\right) + C_1, \tag{6.1}$$

where τ_1 and τ_2 are characteristic times of two contributing relaxation processes, and A_1, B_1 and C_1 are fitting constants. The bi-exponential nature of PL temporal decay suggests the presence of more than one type of charge traps on the surface of the perovskite NCs or the combination of two different effects. This study focuses on the faster initial PL decay time, τ_1, which was observed to decrease with increasing laser power (inset in **Figure 6.3a**). The observed evolution of the PL intensity is accompanied by a time-dependent red shift of the PL peak position,
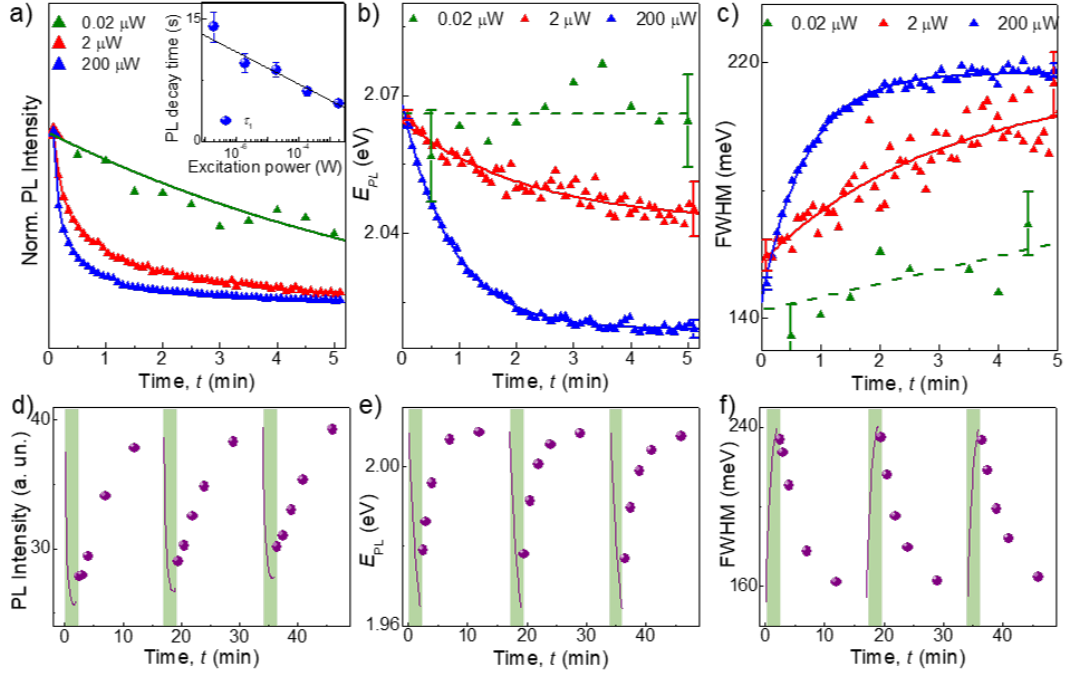
Figure 6.3. a) Temporal response of room temperature PL intensity for CsPb(Br:I=2:3)$_3$ NCs following optical excitation with different powers (λ_{ex} = 532 nm). Inset: dependence of decay time, τ_1, on excitation power, as estimated using a bi-exponential fit of the data in the main figure. The line is a guide to the eye. Dependence of **b)** PL peak position (E_{PL}), and **c)** FWHM on time for continuous exposure of the NCs to laser light at three different powers (λ_{ex} = 532 nm). Lines are guides to the eye. Time-dependence of the **d)** PL intensity, **e)** E_{PL}, and **f)** FWHM during three ON (line)/OFF (spheres) cycles of light exposure. Measurements were performed at room temperature with excitation power $P \approx 0.3~\mu$W at λ_{ex} = 532 nm.

ΔE_{PL}, (**Figure 6.3b**) and broadening of the FWHM (**Figure 6.3c**). Thus, under continuous laser excitation of the NCs, the PL intensity, FWHM, and E_{PL} change over time and the temporal dynamics become faster with increasing laser power. For example at a high power (P = 200 μW), $\tau_1 \approx 5.4$ s, $\Delta E_{PL} \approx 50$meV and FWHM ≈ 60 meV are measured. Whereas for low power (P = 0.02 μW) the measured parameters are $\tau_1 > 100$ s, $\Delta E_{PL} < 10$ meV and FWHM ≈ 10 meV. It is noted that these changes are fully reversible over several cycles of on-off illumination (**Figure 6.3d-f**) and the PL intensity, peak position, and FWHM are fully restored under dark conditions.

6.4 Temperature dependent evolution of PL emission

The photo-induced time-dependent evolution of the PL signal is also affected by temperature and becomes more pronounced with increasing T for $T > 100$ K (**Figure 6.4a–d**). At $T < 100$ K there is no noticeable time-dependent change of PL intensity (**Figure 6.4a**), peak position (**Figure 6.4b**) or FWHM (**Figure 6.4c**). The T-dependence of E_{PL} also depends on the laser exposure time; for initial illumination ($t < 10$ s), a blue shift of E_{PL} is observed with increasing T. In contrast, a red shift is observed for $t = 120$ s (inset in **Figure 6.4d**). In these
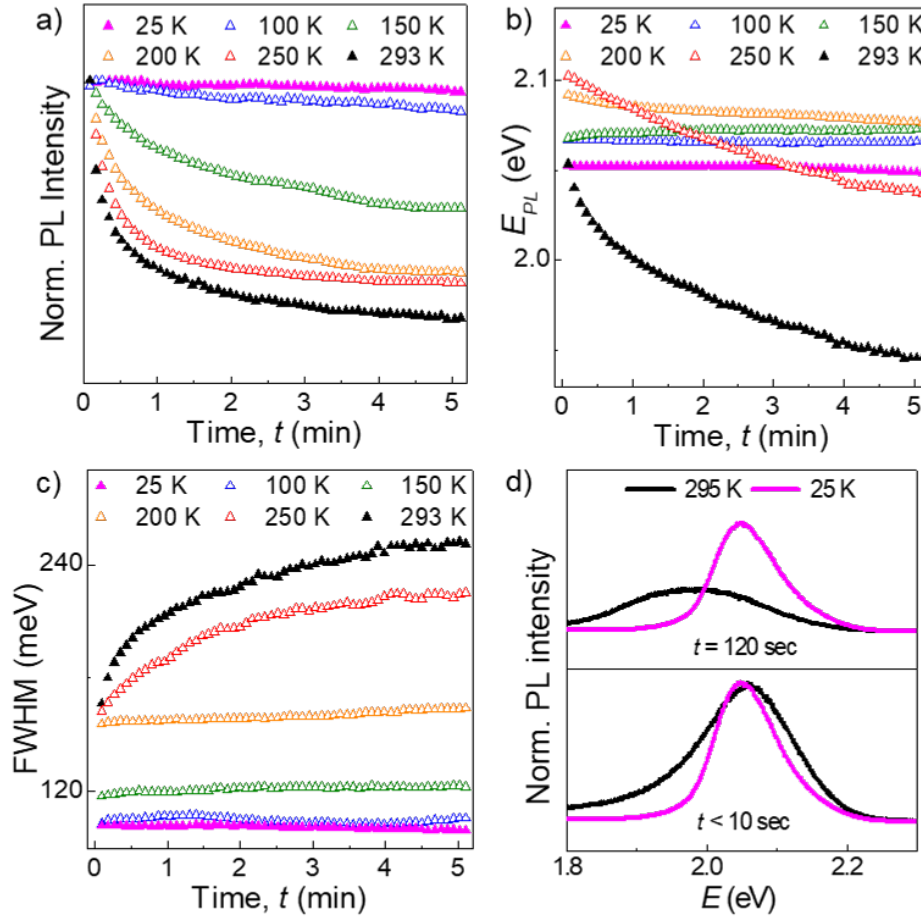
Figure 6.4. Temporal evolution of the **a)** normalised intensity, **b)** peak position, E_{PL}, and **c)** FWHM of the PL spectra of CsPb(Br:I=2:3)$_3$ NCs under continuous illumination ($\lambda_{ex} = 532$ nm, $P = 2$ mW) at different temperatures. **d)** Normalised PL spectra before (bottom) and after (top) 2 min of continuous illumination ($\lambda_{ex} = 532$ nm, $P = 2$ mW) of CsPb(Br:I)$_3$ NCs at $T = 25$ K and $T = 293$ K. PL peak intensity at $t = 120$ s is relative to the normalised PL peak at $t < 10$ s.

studies, a low laser power ($P \approx 2.5$ W/mm^2) is used to avoid irreversible changes of the perovskite crystal structure previously reported for exposure to higher laser powers [106, 112, 115]. We exclude a laser heating effect in our studies as this should cause a blue shift of the PL emission [108, 192], rather than the red shift reported here. Furthermore, the observed strong quenching of PL intensity cannot be explained by the laser heating, as for temperatures in the range 250 to 350 K, our results and those reported in the literature [108, 192] reveal only relatively small changes in PL intensity.

A blue shift of E_{PL} with increasing temperature can arise from the interplay between the electron-phonon renormalisation and thermal lattice expansion. These tend to have opposite effects on the band gap energy of CsPbX$_3$ NCs causing a blue shift of PL with increasing temperature [108, 109]. A different, more complex scenario is observed in our temperature dependent optical experiments, suggesting that additional effects need to be considered. At $T > 150$ K, the optical properties are influenced by both temperature and time dependent phenomena. When $\Delta E_{PL}(t) > \Delta E_{PL}(T)$, a red shift of E_{PL} is observed (**Figure 6.4b**). This can be attributed to a light-induced Stark effect and a trap-assisted recombination of carriers, as discussed in greater detail below. We note that the t-dependent change of the PL peak position and intensity are accompanied by a PL broadening (**Figure 6.4c**), which can arise from inhomogeneity of charge distribution and charging/discharging times for the NCs in the ensemble (see **Section 6.6**).

To briefly summarise these observed results, the temporal and temperature dependent study of the PL signal revealed photo-induced effects that can arise from: (i) the T-dependence of the band gap [106]; (ii) a T-dependence of charge trapping; and (iii) a light-induced Stark effect.

6.5 Probing NC charge dynamics in perovskite/graphene detectors

In order to investigate the origin of the photoinduced time-dependent red shift of E_{PL}, the power dependence of the PL temporal dynamics is examined (**Figure 6.5a**). By taking a snapshot of the PL intensity versus power at different times, we determine the power-dependence of the PL intensity (I_{PL}) at a given time. As shown in **Figure 6.5b**, for $t = 15$ s, I_{PL} follows a power law, $I_{PL} \approx P^\alpha$, where $\alpha = 0.5$. The value of α varies from ~ 0.5 at $t = 15$ s to ~ 0.6 at $t = 300$ s (inset of **Figure 6.5b**). Thus, the dependence of the PL intensity on power becomes stronger with increasing exposure times.
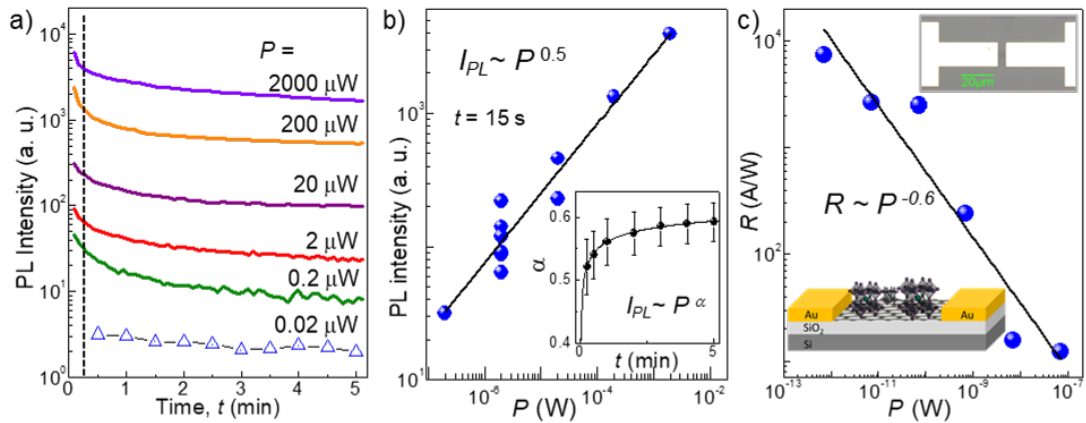
Figure 6.5. a) Dependence of the PL intensity (I_{PL}) of CsPb(Br:I)$_3$ NCs on laser exposure time ($\lambda_{\mathrm{ex}} = 532$ nm) for different excitation powers at room temperature. **b)** PL intensity as a function of power, P, at $t = 15$ s (marked by a vertical line in (a)) with a fit of $I_{PL} \sim P^\alpha$ with $\alpha = 0.5$. Inset: a graph showing the evolution of the coefficient α with increasing exposure time. **c)** Photoresponsivity, R, as a function of power, P, ($\lambda_{\mathrm{ex}} = 405$ nm) and fit of $R \sim P^{-0.6}$ for CsPb(Br:I=2:3)$_3$ NCs deposited on a graphene field effect transistor (FET). Insets: schematic of the device and optical image of a commercial graphene FET [175].

We use graphene field effect transistor (FET) devices decorated with a layer of perovskite NCs to further probe the charge dynamics in this system (see **Chapter 5**) [120, 193]. Interestingly, we find that the power dependence of the photocurrent (I_{ph}) of these devices is similar to the power dependence of I_{PL}. The

photocurrent depends on power as $I_{ph} \propto P^\beta$, leading to a P-dependent photoresponsivity,

$$R = \frac{I_{ph}}{P} \propto P^{\beta-1} \propto P^{-0.6}, \tag{6.2}$$

and $\beta \approx 0.4$ (**Figure 6.5c**). The sublinear power dependences of I_{PL} and I_{ph} are ascribed to the contribution of defects on the NC surface [120].

As discussed in **Section 5.3**, electrical measurements of our perovskite/ graphene devices demonstrate that $CsPbX_3$ NCs act as donors on graphene FETs, transferring electrons into the graphene layer, hence the NCs become positively charged. In these devices, the time-dependence of the photocurrent is slow with a long relaxation time of ~ 100 s, which is comparable to that observed in the PL decay reported here (**Figures 6.3** and **6.4**).

Furthermore, the transfer of photo-generated electrons from the NCs into graphene is a thermally activated process that occurs at temperatures $T > 200$ K. This is ascribed to the thermal ionisation of charged traps on the surface of the NCs with an activation energy $E_x \approx 0.3$ eV (**Section 5.3**) [120]. Thus, the reversible slow PL quenching reported in this work and the previously observed quenching of the photocurrent in $CsPbX_3$/graphene FET devices are likely arising from the same phenomenon, which is a temperature- and time-dependent charging/discharging of the NCs via surface traps.

In summary, the negative photoexcited charges in the NCs are transferred into graphene, leading to accumulation of positive charges at the surface traps of the NCs. These charges build up an internal electric field within the NC leading to a bending of the conduction and valence bands, which affects both photocurrent and PL emission. We develop a model to describe this effect in the following section.

6.6 Modelling the light-induced Stark effect

We assign the reversible decay of the PL intensity to non-radiative recombination of carriers that are trapped on surface defects of the CsPbX$_3$ NCs. Our experimental results indicate that >10 charges can be trapped per NC (see **Section 5.5.2**), resulting in high internal electric field and the separation of photo-generated electron-hole pairs within the NC. The probability of the non-radiative recombination events at the surface of a perovskite NC can be significantly enhanced by a photo-generated internal electric field, which acts to spatially separate photoexcited electrons and holes in the NC, pulling electrons toward the surface. We used an infinite triangular quantum well (TQW) model to explain the effect of this surface charge on the NC electrostatic potential and corresponding electric field [3].

Firstly, in order to confirm that the accumulation of 10 charges is not satisfied through exciton generation/recombination processes alone, we perform a simple estimate for the average number of excitons per NC during continuous illumination. For a laser source with power, P_0, the total power absorbed, P_{abs}, by a NC film of thickness, $w = 300$ nm, is

$$P_{abs} = P_0[1 - \exp\left(-w\alpha_{NC}\right)]. \tag{6.3}$$

where α_{NC} is the absorption coefficient of the NCs, which is $\sim 10^5$ cm^{-1} at $\lambda_{ex} = 532$ nm [137, 194]. Therefore, the number of excitons generated in the NC film per second is $n_{gen} = P_{abs}/E_{ph}$, where $E_{ph} = hc/\lambda_{ex}$ is the photon energy. The exciton recombination time (lifetime) for similar NCs, as measured through TRPL, is $\tau_{PL} \sim 5$ ns [195]. Thus, the maximum number of excitons that can be generated within the exciton lifetime is $N_{gen} = n_{gen}\tau_{PL}$. The total number of NCs (assuming that there is perfect packing) is $N_{NC} = V_{tot}/V_{NC}$, where $V_{tot} = \pi r_l^2 w$ is the total volume illuminated with a circular laser spot of radius, $r_l = 2.5$ μm, and $V_{NC} = l^3$

is the volume of a single cubic NC with side length, $l = 14$ nm. The density of excitons (per NC) is then given by,

$$n_{ex} = \frac{N_{gen}}{N_{NC}} = \frac{n_{gen}\tau_{PL}V_{NC}}{V_{tot}} = \frac{P_{abs}\tau_{PL}l^3}{E_{ph}\pi r_l^2 w},$$ (6.4)

therefore,

$$n_{ex} = \frac{\lambda_{ex}\tau_{PL}l^3}{hc\pi r_l^2 w}P_0[1 - \exp(-w\alpha_{NC})].$$ (6.5)

For a typical PL experiment (**Sections 6.2-6.5**) a power of $P_0 = 200$ μW gives a density of excitons of ~ 1.2 per NC. Therefore, the ~ 10 charges calculated in previous electrical studies of a graphene/perovskite NC device (see **Section 5.5.2**) is not possible by generation/recombination alone. Hence, there must be another mechanism that prolongs the lifetime of photoexcited charges in the NC e.g. trapping or transfer of carriers, which is discussed in **Sections 6.6.1-6.7**. Note that the excitation power used for this calculation is one of the highest experimental values and from **Equation 6.5**, reducing the laser power, P_0, by a factor of 10 further reduces the number of excitons per NC by a factor of 10.

6.6.1 The triangular quantum well potential

To explain the observed temporal evolution of the PL, we consider light induced charge accumulation on the surface of the NC (**Figure 6.6a,b**). A simple band bending diagram shown in **Figure 6.6a** illustrates how the band gap energy of the NCs can be reduced in the presence of an electric field due to charge accumulation. Informed by our previous photocurrent studies on similar CsPbX$_3$ NCs (**Section 5.6**), we infer that the surface traps are positively charged and consider classical electrostatics and the quantum confinement of an electron in the resulting electrostatic potential.

We use a standard TQW (**Figure 6.6c**) [3], with infinite potential at $z = 0$ nm
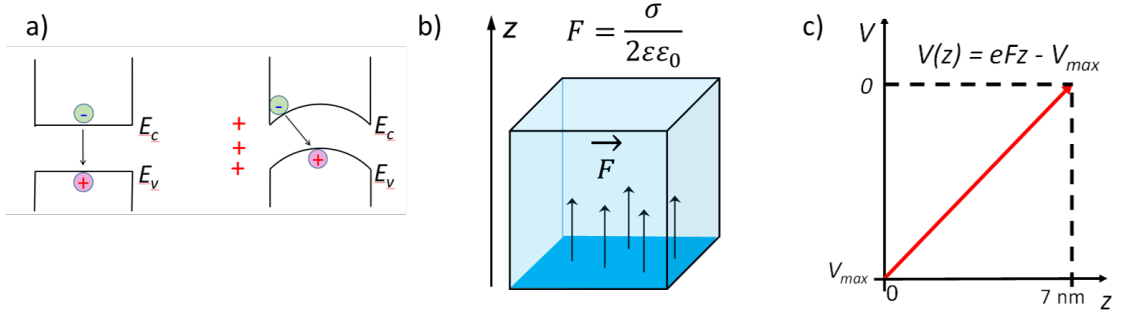
Figure 6.6. **a)** A schematic of the bending of the conduction, E_c, and valence, E_v, bands due to light-induced accumulation of positive charges on the surface of a perovskite NC. **b)** A cubic-shaped NC with 5 positive charges on its bottom surface and resulting electric field F. **c)** TQW potential for perovskite NCs with average side length of 14 nm (7 nm from the surface to the NC centre).

and a linearly increasing potential,

$$V(z) = eFz, \tag{6.6}$$

from $z = 0$ nm to the centre of the NC at $z = 7$ nm, where e is the electron charge and F is the electric field. F can be calculated by assuming an infinite sheet of charge on the NC surface with a density, σ,

$$F = \frac{\sigma}{2\epsilon\epsilon_0} = \frac{eN_e}{2A\epsilon\epsilon_0}, \tag{6.7}$$

where ϵ_0 is the permittivity of free space and $\epsilon = 10$ is the permittivity of the perovskite [184], $A = 14$ nm $\times 14$ nm is the area of one side of the perovskite NC cube and N_e is the number of positive charges per NC (**Figure 6.6b**).

To calculate the electron energies (E_e) and wave functions (ψ) along z, we must solve the one-dimensional Schrödinger equation for the TQW,

$$\left[\frac{-\hbar^2}{2m} \frac{d^2}{dz^2} + eFz \right] \psi(z) = E_e \psi(z), \tag{6.8}$$

where $\hbar$ is the reduced Planck's constant and m is the electron effective mass ($\sim 0.15m_e$ [14], where m_e is the electron mass). The solutions to this equation are

the Airy functions and only one is convergent [3] with energies,

$$E_n = c_n \left[\frac{(eF\hbar)^2}{2m} \right]^{\frac{1}{3}}, \quad n = 1, 2, 3, ... \tag{6.9}$$

The Airy functions oscillate for negative values of z and since there is a an infinite potential at $z = 0$ the only valid solutions are when the Airy functions intersect the z-axis i.e. $\psi(z = 0) = 0$. Hence, c_n is the numerical value for which this boundary condition is met. For the lowest energy level $c_1 = 2.338$.

6.6.2   Triangular quantum well model results

The confinement potential of carriers in the NC is affected by the electrostatic potential generated by surface charges (black line in **Figure 6.7a**) and the quantisation of motion due to the formation of the TQW (dashed blue line in **Figure 6.7a**). Here, it is assumed that the energy of the photoexcited holes in the valence band is not affected by surface charges as they are pushed towards the centre of the NC (inset in **Figure 6.7a**). The model is used to estimate the number of charges, N_e, on the surface of the NC required to achieve the measured red shift of the PL emission, ΔE_{PL} (**Figure 6.7b**). For simplicity, we assume that all photoexcited surface charges are uniformly distributed on one side of the perovskite NC. Different spatial configurations of the surface charges and their spread to other sides of the NC can affect the confinement potential, see **Section 6.6.3** for details. It is important to note that in these macroscopic laser spot (> 1 μm) measurements of the NC ensemble, we do not observe charge related phenomena associated with individual NCs, for example, blinking and single photon emission and relevant photon antibunching [196]. The full recovery of the PL properties observed in our work (**Figure 6.3d-f**) is also well explained by the relaxation/recombination of charges separated by the light-induced Stark effect. This reversibility indicates an electronic effect as opposed to structural effects, such as photobleaching and photoinduced ion migration, which usually lead to
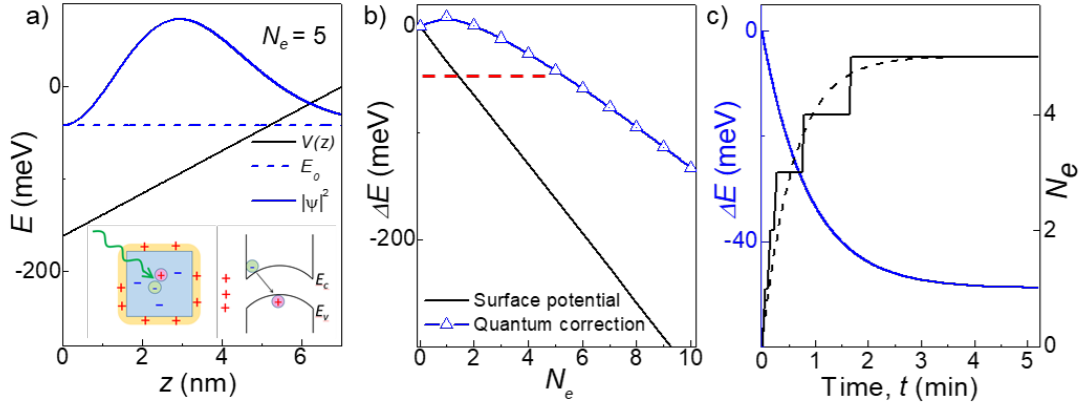
Figure 6.7. a) Spatial profile (black line) of the potential in the NC due to surface charges ($N_e = 5$ elementary charges per NC). z is the distance from the surface to the centre of the NC. Dashed and solid blue lines represent the electron ground state energy, E_0 and its wave function in the TQW, respectively. Inset: schematic of photoexcited charges in a perovskite NC under light, showing electrons being pulled on the surface of the NC due to positively charged surface defects. **b)** Electrostatic potential energy on the surface of the NC (black line) and relevant electron ground state energy calculated using the TQW model (blue line) for different number of surface charges, N_e. The dashed red line shows the measured PL red shift. **c)** Model of the red shift (blue line) over time assuming a charging time constant of 35 s. The solid and dashed black lines represent the relevant number of surface charges; steps on the solid line represent the quantisation of the number of surface charges, N_e.

permanent structural damage (see **Section 6.7** for details).

The generation of light-induced positive charges is evidenced by the shift of the Dirac point to n-type conductivity for graphene decorated with the NCs (see **Section 5.6**). In particular, the time scale for the formation of the defects and/or the lattice deformation is longer than the time for migration of photo-generated electrons towards the surface, resulting in slow temporal dynamics of the PL emission. As the positively charged defect forms, the internal electric field increases, causing a gradual red shift of the PL emission with time. The modelling (**Figure 6.7c**) as well as experimental data (**Figure 6.3**) reveal the saturation of surface charge within a few minutes of the NC exposure to light. The saturation can arise from increasing Coulomb repulsion interactions, which prevents further

accumulation of positive charge on the NC surface.

Figure 6.7b shows the calculated PL shift ($\Delta E = \Delta E_{PL}$) as a function of the number of surface charges N_e. From the TQW model we estimate that 5 charges located on a single side of a cubic CsPbX$_3$ NC are sufficient to account for the measured red shift $\Delta E_{PL} \approx 50$ meV (red line in **Figure 6.7b**). From the energy potential of **Figure 6.7a**, we estimate that the corresponding electric field is $F = 2 \times 10^7$ V/m.

We model the time-dependent charging of the NC surface (**Figure 6.7c**) to show the relationship between the red shift and the number of surface charges, N_e, which is comparable with the experimental data (**Figure 6.3b**). This dependence describes the surface charging process, where the number of trapped charges changes with time as

$$N_e = N_e^{max} \left[1 - \exp\left(\frac{-t}{\tau_c} \right) \right], \tag{6.10}$$

where N_e^{max} is the maximum number of surface charges ($N_e = N_e^{max}$ at $t = \infty$), t is the exposure time, and τ_c is a characteristic charging time. Note that N_e^{max} and τ_c are dependent on the laser power (see **Figure 6.3** for power dependent experimental data). The measured τ_c of ~ 35 s (**Figure 6.7c**) is approximately 10 times larger than the optical relaxation time, $\tau_{rel} = 3.5$ s (**Figure 5.10a**) obtained using electrical measurements on a similar device. We ascribe the difference to the fact that only the perovskite NCs closest to the graphene layer are involved in the charge transfer process presented in **Figure 5.10a** and used to estimate τ_{rel}. Whereas the Stark effect is observed in a thick layer of perovskite NCs with very limited charge transfer between them (see **Section 5.2**). Thus, relaxation of photoinduced charges is about 10 times faster in the vicinity of the graphene layer (**Figure 5.10a**) than within a thick NC layer (**Figure 6.7c**).

These results suggest that the light-induced Stark effect in the NCs can account for both the red shift and reversible time decay of the PL intensity. The slow

dynamics of the PL intensity indicates that the trapping/de-trapping of charges on the NC surface is a process that takes several seconds to minutes, a timescale different from the fast (nanoseconds) dynamics of photoexcited carriers in bulk and NCs based on $CsPbI_3$ [14, 106] or very slow (days) dynamics associated with degradation processes [16, 24].

6.6.3 Beyond the infinitely charged sheet model

The TQW model considers a simple electrostatic potential profile created by an infinite uniformly charged plane (**Equation 6.7**) and therefore does not account for the possible effect of different spatial configurations of charges on the surface of individual perovskite NCs in the ensemble. To examine the effect of different charge configurations on ΔE_{PL}, we perform numerical simulations of different distributions of photoexcited charges and the resulting TQW confining potentials (**Figure 6.8**). For simplicity, we consider a 1D potential along the line going from the centre (at $z = 7$ nm) to the two opposite sides (at $z = 0$ and 14 nm) of the cubic-shaped NC. Also, we place the charges only on the two opposite
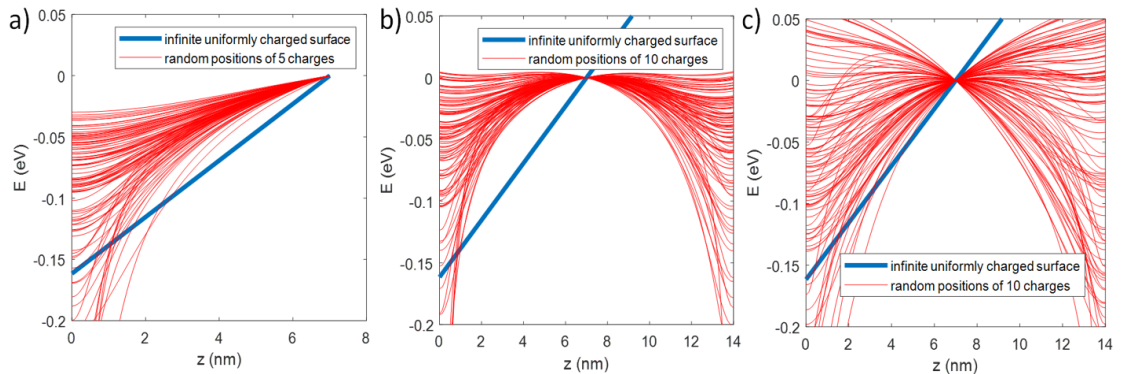
Figure 6.8. a) Electrostatic potential generated by 5 charges randomly distributed on 1 side of a perovskite NC calculated for 100 random configurations of charges (red lines). This is compared with the potential of an infinite uniformly charged plane with the same charge density (blue line). The same calculation done for **b)** 5 charges on each side of the NC and **c)** random number of charges on each side with total number of charges $N_e = 10$. Simulations performed by Miss Joni Wildman and Dr. Oleg Makarovsky.

sides of the cube.

When all the charges are located on one side of the cube (closest to graphene in the FET), the resulting electrostatic potential, calculated using 100 randomly generated configurations of charges (red lines), is qualitatively similar to the potential generated by an infinite uniformly charged plane with the same density of charge (blue line, **Figure 6.8a**). When an equal (**Figure 6.8b**) or random (**Figure 6.8c**) number of charge is placed on opposite sides of the cube, the uncertainty resulting from different charge configurations increases. The main effect of this uncertainty is a reduction of the TQW confining potential, which could lead to a smaller observed PL energy shift for some NCs in the ensemble. Note that the estimated number of perovskite NCs in the ~ 1 μm laser spot is > 1000. Thus, there can be a wide range of different charge configurations present in every experiment resulting in a weaker PL shift as well as an increasing time-dependent broadening of the PL peak observed in our experiments.

6.7   Phenomena affecting charge dynamics

Slow dynamic processes in semiconductor NCs are typically associated with deep surface traps. These are responsible for a number of quantum phenomena such as QD blinking [197]. Blinking (or PL intermittency) is a well-known phenomenon in colloidal QDs and it is also related to non-radiative recombination of carriers on surface charge traps [198], see **Section 2.4.3** for details. Recent findings of a blinking effect in inorganic perovskite NCs [199] demonstrate a similarity between colloidal QDs and perovskite NCs, underlining the importance of probing quantum confinement effects for the understanding of the optical response in these systems [115, 199]. Interestingly, an electrically induced Stark effect was recently reported in $CsPbX_3$ NCs, where it was also accompanied by PL quenching and was explained using the electric field dependence of the PL intermittency effect [117]. Trapping of one type of carrier on the surface of perovskite NCs can result

in the formation of an electrostatic potential, which in turn can strongly affect the performance of optoelectronic devices such as graphene-based FETs [20, 120] and perovskite-based solar cells [22].

Further to surface-related effects, a slow photoresponse can also be caused by bulk properties. For example, another mechanism proposed to explain a reversible PL quenching under light exposure is light-induced segregation of iodine- and bromine-rich regions within the mixed halide perovskite crystal and migration of iodine ions [112–114, 200]. Manifestation of this effect is rather random, with a long (minutes) light exposure leading to a PL intensity decrease [112, 113], and/or increase [114] or redistribution of PL intensity between the PL bands associated with bromine- and iodine- rich NCs [200]. Photoinduced iodine ion migration in $CsPbX_3$ films causing exciton trapping in iodine-rich regions was used to explain a red shift of the PL peak [113, 201] and in NCs the loss of iodine ions through bond breaking was used to explain a blue shift [202]. However, reversible migration of iodine ions has not been observed in individual perovskite NCs [112]. Photodegradation of individual NCs has also been reported and it manifests as an irreversible blue shift and quenching of the PL emission ascribed to a photo-accelerated reaction with water [203]. The complete reversibility of optical properties observed in our work (**Figure 6.3d–f**) allows us to exclude ion migration and NC degradation effects.

The Stark effect model explains our reversible experimental results well, excluding photobleaching, photodegradation and ion migration effects, which in contrast lead to irreversible or partially reversible properties [112–114, 200–203]. The fully reversible effects here are caused by the presence of defects and charge trapping over a time scale longer than the time for migration of photo-generated electrons toward the surface, resulting in a slow temporal dynamic of the PL emission. As the defect forms and electrons accumulate on the surface, the internal electric field increases, causing a gradual red shift of the PL emission with time.

The low excitation power used in our work and full recovery of the PL signal in our experiments allow us to exclude the partially reversible PL decay observed at high excitation laser powers in bulk crystals [112] as well as photodegradation and bleaching effects observed at high excitation power and/or high temperatures ($T > 400$ K) [106, 115].

Another possibility for the observed quenching of PL and red shift of the peak emission is the migration (or diffusion) of excitons between neighbouring NCs [204]. In general energy transfer responsible for exciton migration occurs via three mechanisms [205]: cascade transfer (radiative photon reabsorption); Dexter transfer (electron exchange interactions); and Förster resonance energy transfer (FRET) mediated by Coulomb interactions between a donor and acceptor via dipole-dipole coupling [206–208]. Energy transfer in direct band gap semiconductor NCs is typically described by FRET [209], which requires a spectral overlap of the emission of the donor NC and absorption of the acceptor NC as well as a small ($1 - 10$ nm) spatial separation [205]. We also note that the layer of perovskite NCs in these studies does not conduct in the dark and under light (see **Section 5.2**), thus suggesting that the probability for charge carriers to redistribute within the ensemble of NCs (e.g. via Dexter transfer) should be small even at room temperature. It has been reported in colloidal $CsPbBr_3$ NCs that there is effective energy transfer from smaller to larger NCs, which results in a red shift of emission and increased exciton lifetimes [208]. This leads to a larger number of excitons per NC according to **Equation 6.5**, and also results in an increased probability of non-radiative exciton-exciton annihilation and thus quenching of the PL emission [204, 210]. Whilst our PL measurements, when considered in combination with previous electrical studies of graphene/perovskite NC transistors (**Chapter 5**), suggest a defect state trapping process that leads to a build up of charge in the NC and consequently a Stark effect, we cannot rule out the possibility of exciton migration in these PL studies.

6.8 Summary

Time-dependent optical studies were used to probe the dynamics of photoexcited charges in all-inorganic caesium lead halide $CsPbX_3$ NCs. We have shown that the slow (minutes) formation of positive charges on the surface of the NCs significantly affects the NC optical response. This behaviour is ascribed to a light-induced time-dependent Stark effect and is well described by a simple quantum mechanical model of the confined energy states of a $CsPbX_3$ NC. It is important to emphasise that the presented effect is fully reversible and recoverable. The decay of the PL signal is accompanied by the time-dependent red shift of the PL peak position and broadening of the PL spectrum. The results of optical measurements are supported by the behaviour of photocurrent in $CsPbX_3$/graphene hybrid devices. The similarity of the temporal dynamics are due to the trapping of photo-generated charges on the NC surface defect states. Thus, it is different from previously reported ion migration and other bulk effects causing irreversible or partially reversible lattice modifications.

The combined optical (PL) and transport (photocurrent) studies of photoexcited charges in hybrid low-dimensional devices, such as $CsPbX_3$/graphene, provides a versatile tool for probing the charge dynamics in these systems. This information is essential to improve the performance of perovskite based devices and explain the performance of parameters, such as photoresponsivity and response time.

7 Blue perovskite NCs: UV detection and measurements in high magnetic field

7.1 Introduction

This chapter reports on the use of 'blue' $CsPb(Br/Cl)_3$ perovskite NCs as an optically active layer in hybrid perovskite/graphene UV-specific photodetectors. These devices exhibit high photoresponsivity up to 10^6 A/W in the UV range and an apparent enhancement of the graphene field effect mobility. The role of substrates on graphene photoresponse in the UV spectral range is also investigated. Blue perovskite NCs/graphene FETs were also selected for the study of the effect of strong magnetic fields (up to 60 T) on the charge transport and charge transfer dynamics. A magnetic field induced charging/discharging of perovskite NCs on graphene is reported for the first time and modelled similar to the electric field gating with the 2C model (see **Section 5.5**). Transport and optoelectronic characterisation of these devices were carried out following the procedures described in **Sections 4.7** and **4.8**. A description of the magneto-transport measurements performed is found in **Section 4.7.4**.

High pulsed magnetic field measurements up to 60 T were conducted at the Laboratoire National des Champs Magnétiques Intenses (LNCMI) [211] in collaboration with Dr. Walter Escoffier, Prof. Michel Goiran and Dr. Mathieu Pierre. High quality pristine CVD graphene FETs were provided by collaborators, Dr. Camilla Coletti and Dr. Vaidotas Mišeikis, in the NEST laboratories at the Istituto Italiano di Tecnologia, Pisa, Italy [212].

7.2 Blue perovskite NCs

In order to fabricate a UV-specific photodetector with high responsivity in the UV range, we employed the same hybrid planar graphene FET architecture, as in **Section 5.2**, but with a modified perovskite NC composition (**Figure 7.1a**). The halide content of the NCs was tuned to a mix of bromine and chlorine ions (CsPb(Br/Cl)$_3$), resulting in blue photoluminescence emission (~ 460 nm) under UV excitation (**Figure 7.1b**). The composition of ligands used for passivating the NCs was also changed with bromophenylmethyl (BPM) replacing the previously used IDA ligands to improve the long-term stability of the NCs. The halide-incorporating ligands are known to bind more strongly to the surface of the
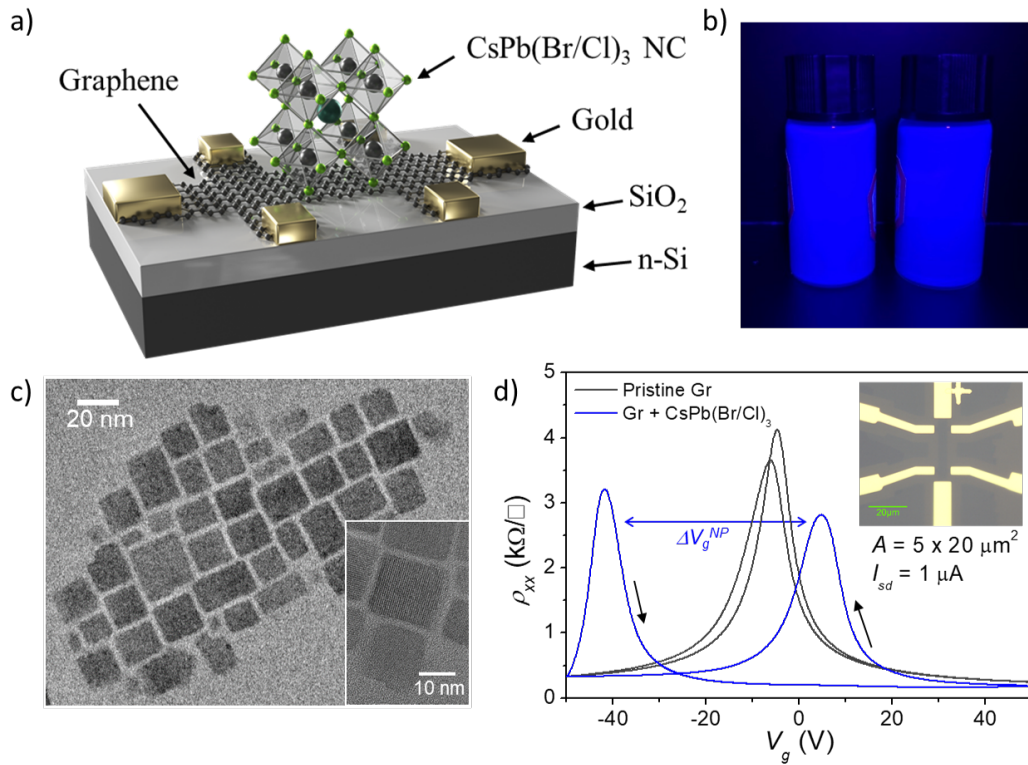
Figure 7.1. **a)** Schematic of the structure of CsPb(Br/Cl)$_3$ perovskite NC and graphene FET photodetector. Credit: Viktoriya Kernytska. **b)** Image of the NCs in hexane solution under UV (λ_{ex} = 365 nm) illumination. **c)** Representative TEM and HRTEM (inset) images of the CsPb(Br/Cl)$_3$ NCs. **d)** Room temperature dependence of the longitudinal resistivity, ρ_{xx}, on applied gate voltage, V_g, of a pristine graphene device before (grey line) and after deposition of the CsPb(Br/Cl)$_3$ NCs (blue line). Black arrows indicate V_g sweep direction. Inset: optical microscope image of short graphene Hall bar.

perovskite crystal [213]. As seen previously with the CsPbX$_3$ NCs (see **Figure 5.1b**), these blue perovskites also form cubic structures, with an average size of 16.4 ± 0.3 nm (**Figure 7.1c**).

Upon deposition of the NCs on a graphene short Hall bar FET (inset of **Figure 7.1d**) there is a n-type shift of the charge neutrality (Dirac) point, V_g^{NP}, and huge anomalous hysteresis, ΔV_g^{NP} between forward (negative to positive V_g) and reverse (positive to negative V_g) sweeps of gate voltage (**Figure 7.1d**). Deposition of the NCs led to the average position of the Dirac point shifting from -5 V to -18 V and the hysteresis increasing from ~ 1 V to 46.5 V for a maximum gate voltage sweep, $V_g^{max} = \pm 50$ V, and sweep rate of 0.2 V/s at room temperature. This is the same phenomenon that was observed in perovskite NCs with iodine and bromine ions (see **Section 5.3**), further confirming the attribution of this effect to Pb-related defect states [120].

7.3 Enhanced field effect mobility of blue perovskite/ graphene FET

A strong dependence of ΔV_g^{NP} on the maximum sweep value, V_g^{max}, is also observed in these devices (**Figure 7.2a**) and is comparable to the effect observed on previous CsPb(Br/I)$_3$/graphene devices (see **Section 5.3**). However, this time instead of increasing the maximum applied gate voltage, V_g^{max}, to maximise the hysteresis we instead reduce V_g^{max} in an attempt to confine the hysteresis within a small V_g range. The reduction of V_g^{max} leads to a strong asymmetry of $\rho_{xx}(V_g)$ for the forward and reverse sweeps. The peak of $\rho_{xx}(V_g)$ near the Dirac point becomes much more narrow for the forward sweep due to its close proximity to the edge of the V_g sweep range (**Figure 7.2a**). This corresponds to an apparent enhancement of the field effect mobility calculated using the maximum slope of $\sigma_{xx}(V_g)$ in the vicinity of the Dirac point (see **Section 3.1**).
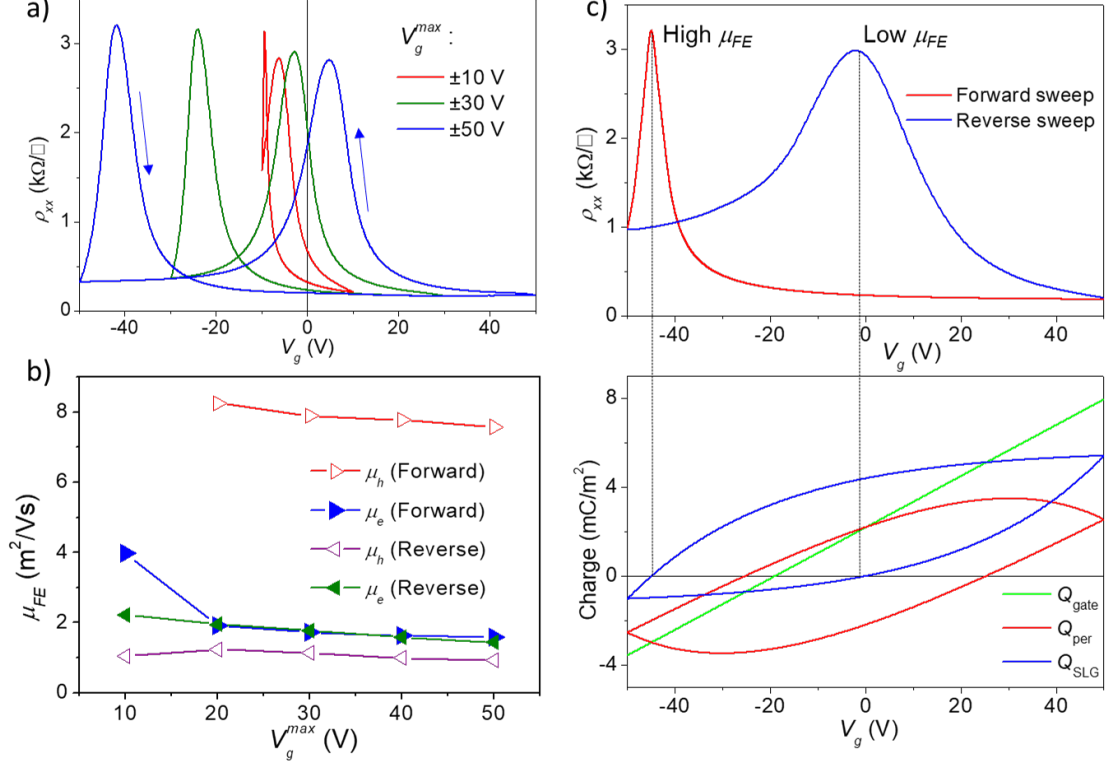
Figure 7.2. **a)** Room temperature dependence of the longitudinal resistivity, ρ_{xx}, on applied gate voltage, V_g, of the hybrid graphene/CsPb(Br/Cl)$_3$ FET for different maximum gate voltage sweep values, V_g^{max}. Arrows indicate sweep direction. **b)** Comparison of the electron and hole field effect mobilities (μ_e and μ_h, respectively) versus the maximum applied gate voltage, V_g^{max}, for both the forward and reverse sweeps. **c)** A model of a $V_g^{max} = \pm 50$ V sweep (top) from (a) and the corresponding charge in the gate (Q_{gate}), graphene (Q_{SLG}) and perovskite (Q_{per}) as calculated using the 2C model (bottom). Vertical dashed lines indicate charge neutrality (Dirac) points at which $Q_{SLG} = 0$ for the forward and reverse V_g sweeps.

In **Figure 7.2b** we plot the calculated electron and hole mobilities, μ_e and μ_h, respectively, for both the forward and reverse sweeps as a function of V_g^{max}. The electron mobility, $\mu_e \sim 20,000$ cm^2/Vs, is the same for both the forward (blue curve) and reverse (green curve) sweeps until $V_g^{max} = 10$ V, where the strong narrowing of the forward sweep Dirac point peak results in a doubling of the electron field effect mobility ($\mu_e \sim 40,000$ cm^2/Vs). The value of the hole mobility is significantly different for the forward and reverse sweeps. The forward sweep is compressed by the maximum negative sweep voltage, whereas the reverse sweep Dirac point is far away from the edge of the V_g sweep range and is therefore

less affected. The hole mobility for the forward sweep is artificially enhanced by the compression and reaches a maximum of $\mu_h \approx 82,600$ cm^2/Vs, which is a record high value for CVD graphene and similar to the mobility of the best exfoliated graphene layers [45]. This hole mobility is $\sim 10\times$ larger than for the reverse sweep and almost $13\times$ larger than the original pristine graphene hole mobility ($\mu_h \approx 6,500$ cm^2/Vs).

This $\rho_{xx}(V_g)$ compression phenomenon can be well explained using the 2C model (see **Section 5.5**) by the difference in gradient of the charge curve for graphene, Q_{SLG}, as it crosses the Dirac point i.e. zero charge carrier density (**Figure 7.2c**). Note that μ_{FE} is calculated using the slope of $\sigma_{xx}(V_g)$ close to the Dirac point, i.e. in the region where $\frac{d\sigma}{dV_g}$ has a maximum (see **Section 3.1** and **Figure 3.1b**). In the case of constant mobility ($\mu_{FE} = const.$) $\sigma(V_g) \propto n(V_g) \propto Q_{SLG}(V_g)$. However, $\frac{dQ_{SLG}}{dV_g}$ changes significantly depending on V_g^{max} and the direction of the V_g sweep, which produces an 'eye'-shaped curve, as shown in **Figure 7.2c**. The 'eye' curve has a larger gradient close to the edge of the sweep range than near the centre of the curve and thus, if the Dirac point ($Q_{SLG} = 0$) is positioned close to the edge, μ_{FE} is larger. This finding explains the large (up to factor of 13) difference of μ_{FE} measured in graphene FETs with a large density of slow charge traps (i.e. perovskite NCs). We envisage that this effect is not exclusive to perovskite/graphene devices and can be observed in other materials with high density of charge traps and slow charging/discharging times leading to large uncertainty in μ_{FE} estimated for these devices. Alternatively, carrier mobility can be determined directly through the Hall effect (discussed in **Section 7.7**).

7.4   UV-specific perovskite/graphene photodetector

To evaluate the potential of CsPb(Br/Cl)$_3$ functionalised graphene devices as a UV-specific photon detector, we examine the wavelength response of the device using a UV-monochromator in a DC photocurrent measurement (see **Section**

4.8.4). A measurable response of the device is recorded at $\lambda_{ex} \sim 460$ nm and extends into the UV range down to $\lambda_{ex} = 300$ (**Figure 7.3a**). We note that the positive photoresponse ($\tau_1 \sim 10$ s) is counteracted by a slow, negative fall of the current ($\tau_2 > 1$ min). Partial recovery of this slow effect is shown in the inset of **Figure 7.3a**. The complete recovery of the device to the initial dark state value was observed after 48 h in the dark. The origin of the slow negative response is yet to be understood and could be due to a secondary effect in the perovskite NCs that causes photogating of the graphene. We exclude a substrate photoresponse as the incident light power density ($P_D \sim 4-5$ nW/mm^2) is lower than that initiating substrate effects (see **Section 7.5**).

The device has high photoresponsivity, $R > 10^6$ A/W, at excitation wavelengths $\lambda_{ex} = 250$, 405 and 450 nm (see **Figure 7.3b**) and a power law dependence of $R \sim P^{-0.56}$. During measurement of the photoresponsivity, the slow secondary effect was noted where the photocurrent changed sign at higher powers. In order to measure this effect in more detail, long exposure times ($t_{ex} = 25$ mins) were used (**Figure 7.3c**). At low power density, $P_D = 0.15$ nW/mm^2, the photocurrent is positive. Since the graphene is n-type in the dark (from **Section 7.3**), positive photocurrent implies a further n-type shift of the Dirac point, suggesting that photoexcited electrons are transferred into graphene, which is similar to the observations for CsPbI$_3$/graphene devices (**Section 5.6**). As the excitation power is increased to $P_D > 1$ nW/mm^2 the photocurrent reaches a maximum positive value and then starts to decrease. The magnitude and the rate of the decrease inversely depend on the laser power. The response times at $P_D = 74$ nW/mm^2 are $\tau_{fast} \sim 8$ s and $\tau_{slow} \sim 64$ s for fast (positive) and slow (negative) components, respectively. The fast initial positive response is $\sim 5\times$ slower than compared to CsPbI$_3$/graphene detectors discussed in **Section 5.7**. The reason for different times could be due to the use of different ligands, which can lead to a difference in potential barriers between the NCs and graphene, possibly leading to different response times. Interestingly, at even higher power ($P_D = 74$ nW/mm^2)
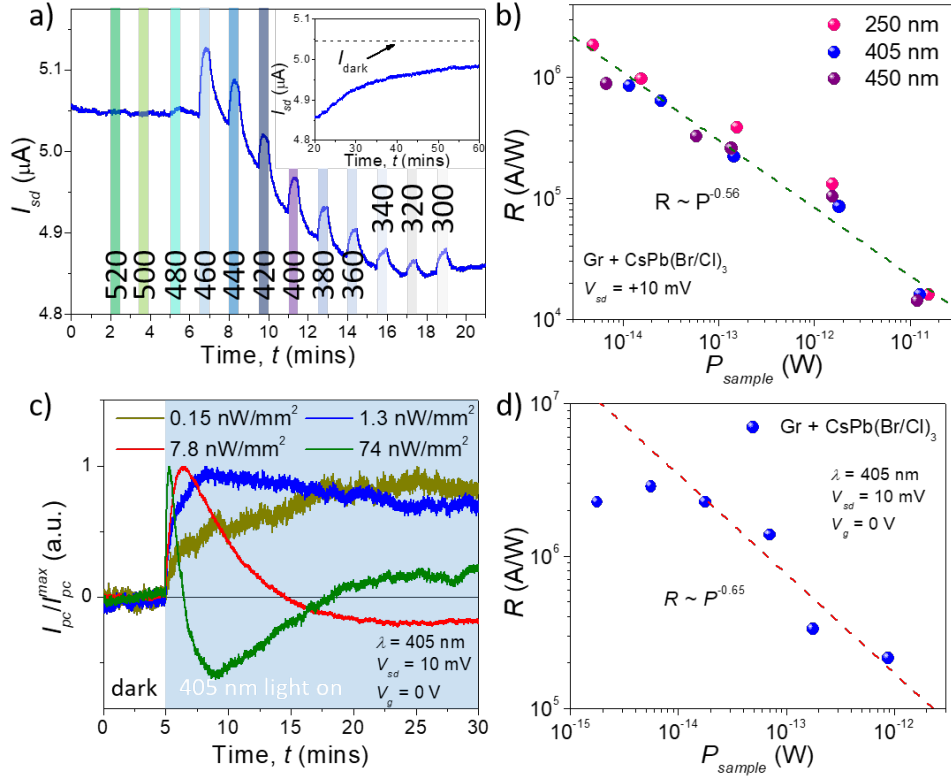
Figure 7.3. **a)** Dependence of source-drain current, I_{sd}, on time for exposure of the $CsPb(Br/Cl)_3$/graphene detector to different excitation wavelengths measured using the UV-enhanced monochromator ($P_D \sim 4 - 5$ nW/mm^2 for all wavelengths). **b)** Photoresponsivity, R, dependence on the incident power on the sample, P_{sample}, for $\lambda_{\text{ex}} = 250, 405$ and 450 nm light sources for fast, positive photocurrent. **c)** Dependence of normalised photocurrent on time under exposure to different powers of excitation at $\lambda_{\text{ex}} = 405$ nm with $t_{ex} = 25$ mins (light ON represented by light blue block). **d)** Dependence of R on P_{sample} for $\lambda_{\text{ex}} = 405$ nm, as calculated from the maximum positive (unnormalised) photoresponse results shown in (c)).

the photocurrent starts to increase again, which could indicate yet another effect and demonstrates the complexity of the behaviour of these devices at high energy excitation. Hence, we are unable to evaluate the device performance at higher powers.

The photoresponsivity calculated from the maximum positive photocurrent reached during the $t_{ex} = 25$ mins exposure is shown in **Figure 7.3d**, corresponding to $R = 2 \times 10^6$ A/W at $\lambda_{\text{ex}} = 405$ nm. The power dependence of the responsivity for the long exposure measurements is described by $R \sim P^{-0.65}$

and is different from the initial power dependence (see **Figure 7.3b**). The results in **Figure 7.3c** clearly show that the power dependence depends on the point at which the value of photocurrent is recorded and is comparable to the power dependence for PL quenching and photocurrent observed in **Section 6.5** for $CsPb(Br:I=2:3)_3$/graphene devices and is ascribed to the Pb-defects on the NC surface [120]. Further studies are required to clarify the mechanisms responsible for the complex temporal behaviour in these devices under exposure to UV light, but is likely due to light-induced activation of deep levels with long carrier trapping/de-trapping times.

7.5   Selecting substrates for UV detection

Silicon substrates, used in graphene FETs, can photogate the device under excitation within the silicon's absorption range [152, 167], as well as possible ionisation of defects within the SiO_2 layer under high energy UV excitation [169, 170]. In order to confirm that the photoresponse of the perovskite/graphene device was due to the perovskites and not a substrate induced effect we attempted to quantify the photoresponse on different graphene FETs.

A very fast ($t < 0.1$ s) response was observed for graphene FET devices on Si/SiO_2 substrates (**Figure 7.4a**) across all wavelengths with $R \approx 0.15$ A/W, which is likely due to the absorption of graphene [138, 139]. However, we also observe a slow ($\tau > 2$ mins) secondary response that is more pronounced at higher energies and becomes dominant at $\lambda_{ex} < 635$ nm. This effect is attributed to the generation and accumulation of photoexcited carriers at the SiO_2/Si interface [167], causing a photogating effect. We also note that UV excitation with high power can cause irreversible bleaching of the device, resulting from the irreversible migration/loss of iodine ions from the NCs [112]. UV bleaching is also observed in typical SiC-grown graphene devices, which were provided to us by Prof. Sergey Kubatkin's group from Chalmers University of Technology, Sweden [214]. These
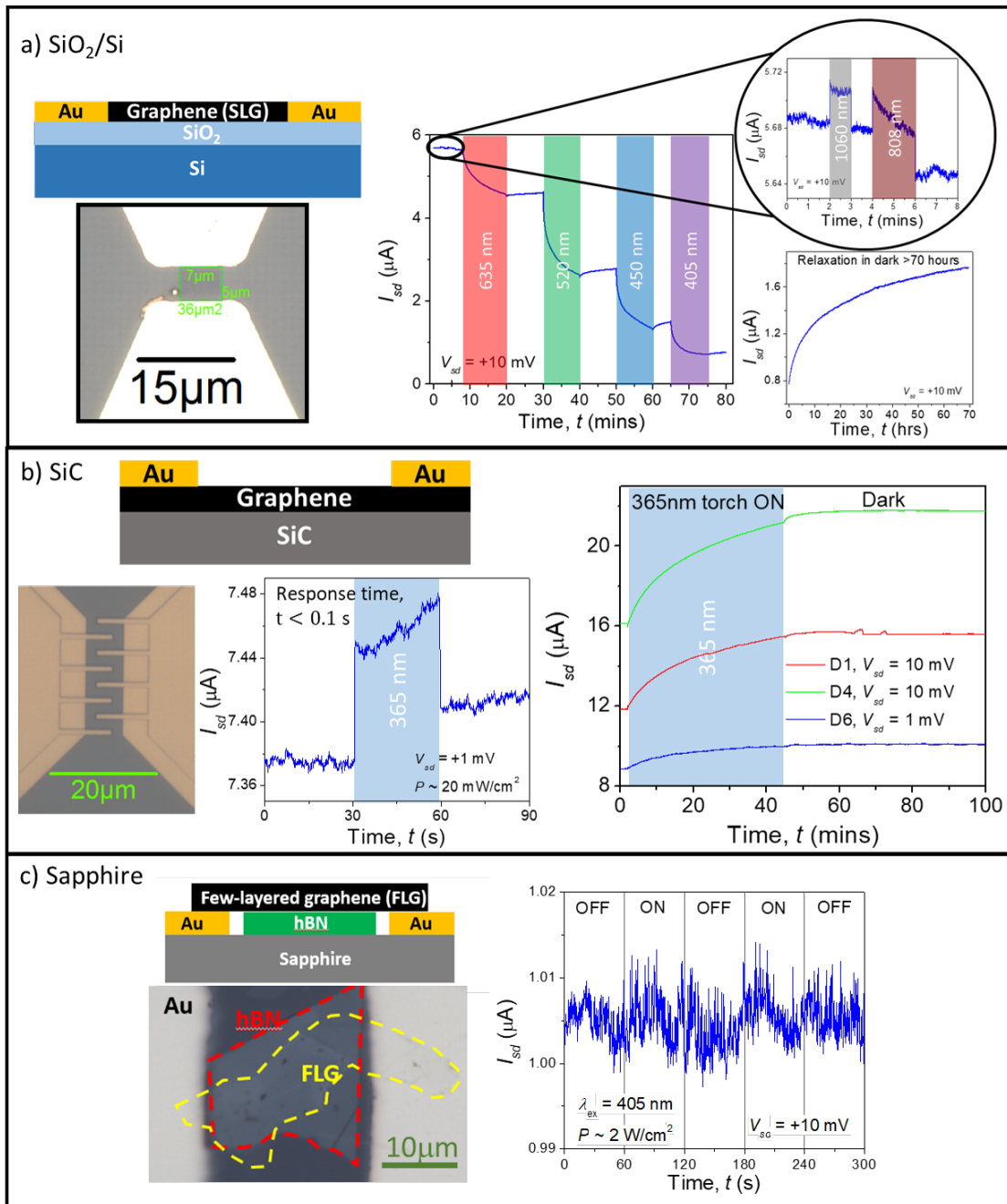
Figure 7.4. **a)** Layer structure (top) and optical image (bottom) of graphene/SiO_2/Si FET and its photocurrent measured under different excitation wavelengths ($P = 0.6$ W/cm^2) with enhanced figure for $\lambda_{\text{ex}} = 808$ and 1060 nm and subsequent relaxation of photoresponse below. **b)** Layer structure and optical image of a SiC graphene detector and fast initial change of I_{sd} under UV excitation ($P \sim 20$ mW/cm^2) and longer response under the same conditions. **c)** Layer structure and optical image of mechanically exfoliated and stamped graphene/hBN/sapphire device (provided by Dr. Zakhar Kudrynski) and corresponding I_{sd} under high power excitation ($P \sim 2$ W/cm^2) at $\lambda_{\text{ex}} = 405$ nm.

devices show a fast ($t < 0.1$ s) response of graphene accompanied by a slow irreversible response (**Figure 7.4b**), which we cannot yet fully explain.

As a potential alternative UV neutral substrate we examine a graphene device on a sapphire (Al_2O_3) substrate. No measurable photocurrent was observed under high excitation power density of $P_D \sim 2$ W/cm^2 at $\lambda_{ex} = 405$ nm (**Figure 7.4c**). Sapphire is a wide gap dielectric with a band gap of ~ 7 eV (180 nm), which can vary depending on the crystalline structure [215], hence it is not optically active under our experimental conditions. For devices using sapphire as a dielectric substrate, a top gate is needed for electrical gating, but for photodetection this isn't necessary.

The substrate related photoresponse discussed here occurs only at relatively high powers ($P_D > 1$ mW/cm^2), which is over 5 orders of magnitude higher power than that corresponding to the maximum sensitivity of the perovskite/graphene devices. Hence, these effects do not contribute to the device performance in experiments below this power threshold ($P_{max} = 1$ mW/cm^2). However, higher power applications would require the use of alternate substrates such as sapphire.

7.6   Magneto-transport of CsPbX$_3$/graphene FETs

We have previously explored the charge transfer behaviour of CsPbX$_3$/graphene FETs in the presence of an electric field and/or under electromagnetic excitation. Here, we explore the effect of an applied magnetic field on charge dynamics. The measurements in high magnetic fields, up to 60 T, were performed at the Laboratoire National des Champs Magnétiques Intenses (LNCMI) in Toulouse and therefore required the device to be mounted onto a non-magnetic header (**Figure 7.5a**). Initial electrical characterisation performed in Nottingham (**Figure 7.5b**) confirmed that the device had very similar properties to the CsPb(Br/Cl)$_3$/graphene device in **Section 7.2**. To ensure the full coverage of the

graphene Hall bar device with perovskite NCs, we deposited a thick layer of NCs (**Figure 7.5a**). The $R(V_g)$ hysteresis was observed at $T > 200$ K and, as expected from previous studies, was not present at lower T, where the device performance is comparable to that of a pristine graphene FET (**Figure 7.5c**). Furthermore, the device demonstrates behaviour expected for pristine graphene in applied high mag-
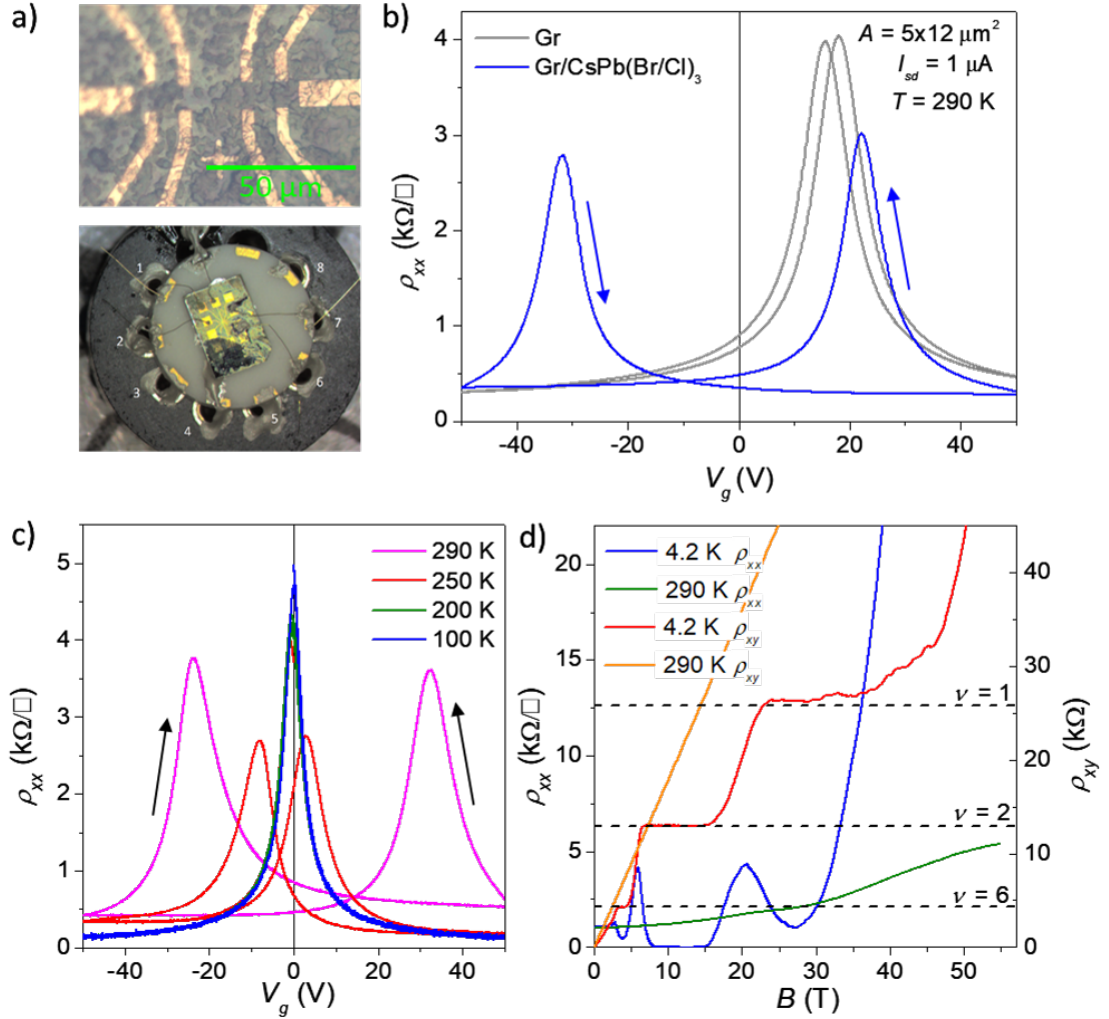
Figure 7.5. **a)** Optical microscopy images of a graphene Hall bar device decorated with CsPb(Br/Cl)$_3$ NCs (top) and mounted onto LNCMI non-magnetic header (bottom). **b)** Room temperature dependence of the longitudinal resistivity, ρ_{xx}, on applied gate voltage, V_g, for a pristine graphene device (grey line) and after deposition of a thick layer of CsPb(Br/Cl)$_3$ NCs (blue line). Area of device in 4-terminal configuration, $A = 5 \times 12$ μm^2. Arrows indicate V_g sweep direction. **c)** $\rho_{xx}(V_g)$ characteristics measured at different temperatures. Arrows indicate V_g sweep direction. **d)** Longitudinal, ρ_{xx}, and transverse, ρ_{xy}, resistivities of the device as a function of applied magnetic field measured at $T = 4.2$ and 290 K. Black dashed lines represent the quantised Landau levels for ρ_{xy} corresponding to the $\nu = 1, 2$ and 6 filling factors.

netic field at low T, revealing defined QHE plateaus in the transverse resistivity, ρ_{xy}, and corresponding minima in the longitudinal resistance, ρ_{xx}, corresponding to $\nu = 1, 2$ and 6 Landau levels (**Figure 7.5d**). At room temperature the QHE plateaus are not observed, instead a linear increase of the classical Hall voltage was measured with increasing B. Also, a $\sim B^2$ increase in ρ_{xx} and weak Shubnikov-de Haas oscillations were observed (**Figure 7.5d**).

It is apparent from these results that there is no perovskite-induced magnetic field related phenomena present under these conditions. However, it is important to note that in pulsed magnetic fields ($B < 60$ T) the device is only exposed to high magnetic fields for very short times (~ 100 ms). Charging of the NCs through electric field gating typically takes > 100 s (**Section 5.7**) and optical charging/discharging has an effective time on the order of ~ 10 s (**Section 7.4**). Thus, it is possible that the pulsed field duration is too short for any perovskite-related effects to be observed. Furthermore, all charge transfer between NCs and graphene measured thus far (electric field- and light-induced) has only been present at high temperatures ($T > 200$ K). However, quantum effects, such as the QHE, are strongly temperature dependent and are typically not observed at $T > 200$ K, with only one report of QHE in graphene at room temperature [216], which was achieved on exfoliated graphene with high mobility ($\mu \approx 10,000$ cm^2/Vs). Hence, the difference in T-range for NC-induced charging effects and quantum effects observed in graphene is likely preventing the observation of NC-induced quantum effects.

The original idea of the $B < 60$ T experiment was to study the possible charge transfer effects in the quantum Hall regime. This effect can lead to a giant QHE $\nu = 2$ plateau and has been observed in SiC-grown graphene [217] as well as CVD graphene/InSe heterostructures [36]. However, the giant QHE plateau is observed only in $T < 200$ K, making it impossible to observe in our devices.

Large uncertainty of carrier concentration, $n(V_g)$, and field effect mobility,
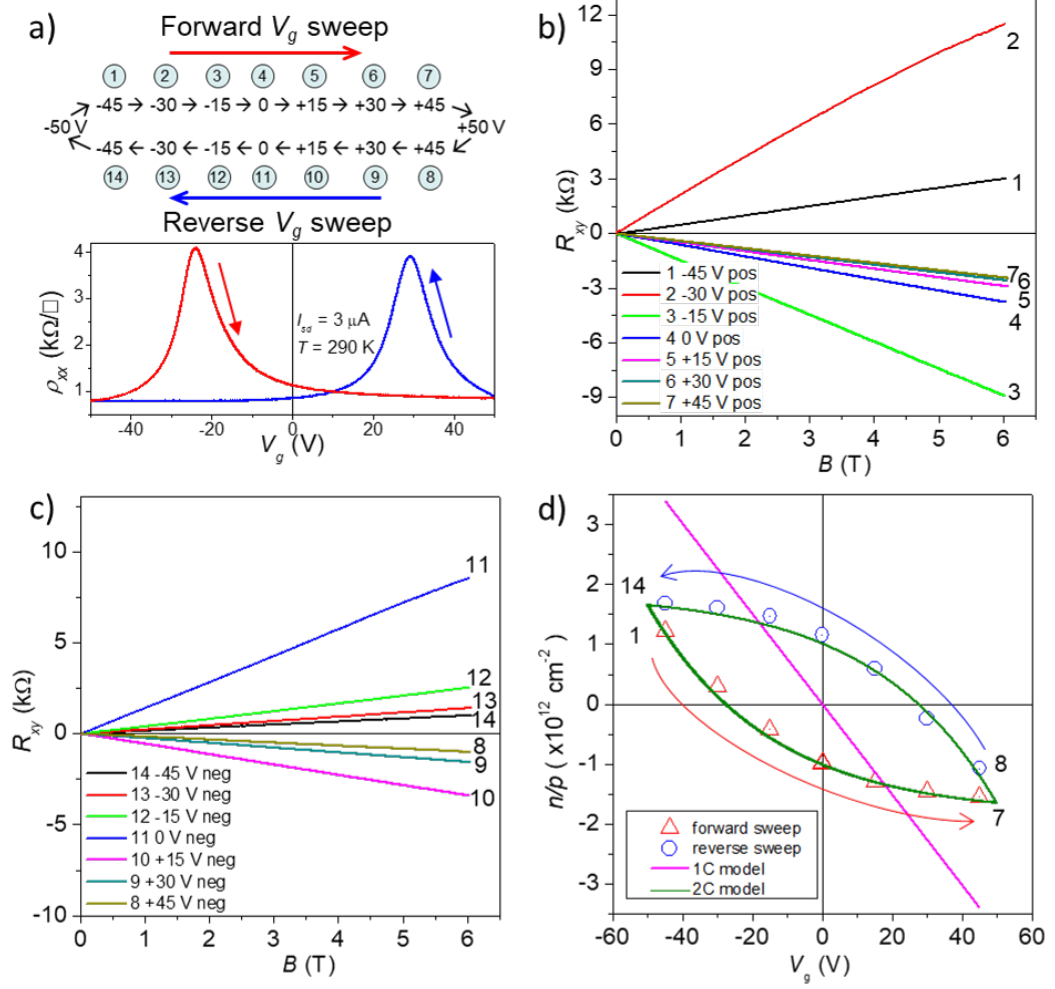
Figure 7.6. **a)** Schematic of the sequence used for pulsed B field measurements (top) for the continuous gate voltage sweep (bottom) with $V_g^{max} = \pm 50V$ (sweep rate 0.1 V/s, $T = 290$ K). Pulsed magnetic field (~ 1000 T/sec) measurements of R_{xy} during uninterrupted V_g sweeps in the **b)** forward direction (V_g changing from -50 V to $+50$ V) and **c)** reverse direction (V_g changing from $+50$ V to -50 V). R_{xy} measurements taken at the same V_g have the same colour in (b) and (c). **d)** Data points represent Hall carrier concentration calculated using R_{xy} data presented in (b) and (c). Arrows indicate forward and reverse direction of the V_g sweep. Solid lines represents the two $n(V_g)$ models: conventional 1C model (magenta) and 2C model (green) with $\tau_{RC} = 350$ s.

$\mu_{FE}(V_g)$, discussed in **Section 7.3** could be eliminated using ultra fast Hall effect measurements. At LNCMI we have developed a novel method of measuring $n(V_g)$ for the perovskite NC/graphene device 'on the run', which consists of continuously sweeping the gate voltage at a constant rate and constant maximum gate voltage so that the system is in a stable hysteresis loop (**Figure 7.6a**). A small magnetic field 'shot' of $B = 6$ T in < 100 ms is then taken at evenly spaced gate voltage

values for both the forward and reverse sweep, as illustrated in **Figure 7.6a**; the numbers in the figure correspond to the linear plots of $R_{xy}(B)$ in the forward sweep (**Figure 7.6b**) and reverse sweep (**Figure 7.6c**). Positive and negative R_{xy} correspond to electron and hole conductivity of graphene, respectively. From the gradient of $R_{xy}(B)$ we get R_H, which is inversely proportional to the carrier concentration (see **Section 3.3**). The data points for carrier concentration are plotted as a function of gate voltage with a comparison of the carrier concentration calculated using the 1C model and 2C model with a time constant $\tau_{RC} = 350$ s (**Figure 7.6d**). According to the 1C model used to describe the behaviour of a graphene FET, the carrier concentration increases linearly with V_g (see **Equation 3.5**). However, the data is better fit using our 2C model, which takes into account the presence of the NCs on graphene. The ultra fast Hall measurements provide an independent proof of the 2C model.

The 'High T mag' system (**Sections 4.7.3** and **4.7.4**) allows slow ($\sim 4\,\mathrm{mT/s}$) ramping of B field ($B \leq 16$ T), as well as continuous B field measurements. In order to confirm the presence of a magnetic field charging effect in the NCs the field was swept to $B = 16$ T and held at constant field for up to 2 h before decreasing B to zero. A measurable hysteresis in R_{xy} is observed at room temperature ($T = 290$ K) and not at $T = 200$ K (**Figure 7.7a**). To quantify the hysteresis we plot the difference in R_{xy} between the up and down sweep, calculated at different T (**Figure 7.7b**) as

$$\Delta R_{xy} = R_{xy}^{up} - R_{xy}^{down}. \tag{7.1}$$

The hysteresis increases with temperature above $T \sim 200$ K. This dependence is analogous to the electric field effect hysteresis (**Section 5.4**) and photocurrent temperature dependence (**Section 5.6**) observed for $CsPbX_3$/graphene devices. These results provide further evidence of the suppression of charge transfer from the NCs into graphene at low ($T < 200$ K) temperatures (**Section 6.4**) and could indicate that the same Pb-defect states are responsible for light, electric
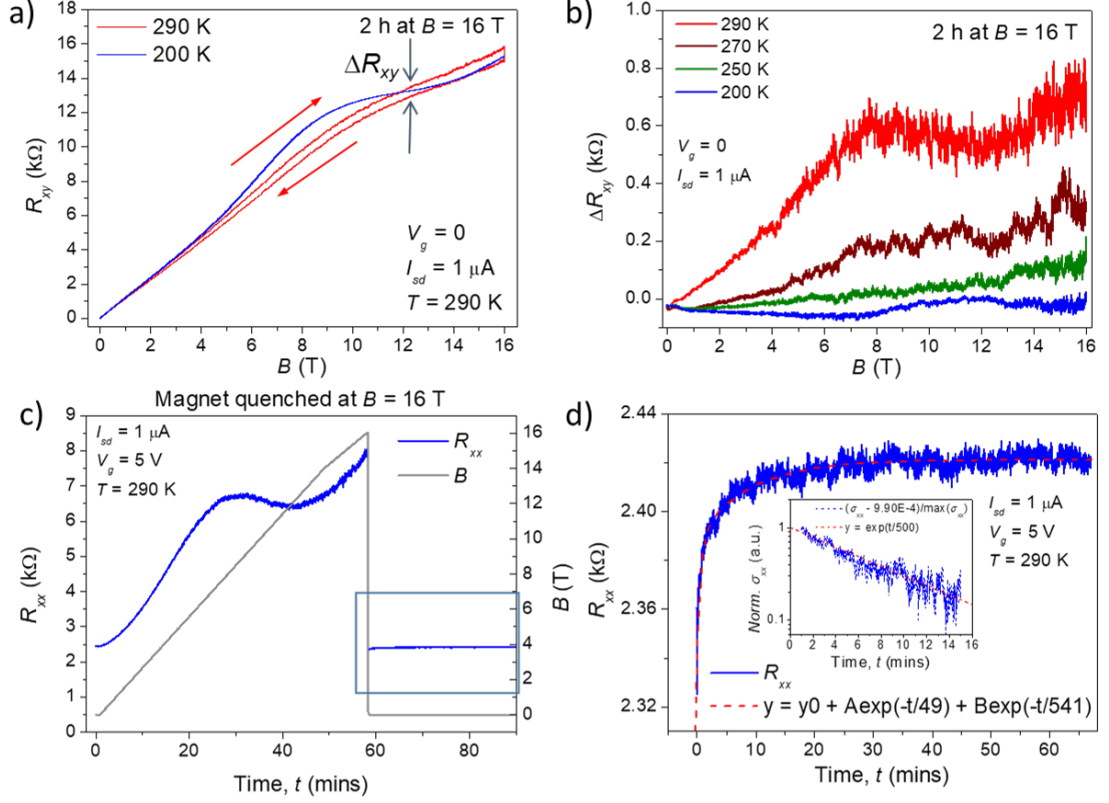
Figure 7.7. **a)** Dependence of the hysteresis of R_{xy} on magnetic field at $T = 200$ K (blue line) and $T = 290$ K (red line) with magnetic field held at $B = 16$ T for 2 h between up and down sweeps. **b)** Difference in resistance, ΔR_{xy} measured for up and down sweeps of B as a function of applied magnetic field at different temperatures. **c)** Temporal change of R_{xx} and B for the magnetic field measurement that quenched at $B = 16$ T. **d)** Change of R_{xx} over time after the magnet quench highlighted by the rectangle in (c) with bi-exponential fit for the time constants. Inset shows a normalised plot of conductivity σ_{xx} versus time for the secondary relaxation time (1 min after quench).

and magnetic field mediated processes.

During one of the magnetic field sweeps a quench of the superconducting magnet was unintentionally triggered causing the field to rapidly decrease ($t_{quench} < 1$ s) from $B = 16$ T to 0 T (**Figure 7.7c**). This gave us a unique opportunity to directly measure the relaxation time of the magnetic field charging effect (**Figure 7.7d**) from the $R_{xx}(t)$ data after the quench (highlighted by rectangle in **Figure 7.7c**). A bi-exponential fit was used to find the time constants associated with magnetic field relaxation revealing an initial fast relaxation $\tau_{mag1} \approx 50$ s and a slower relaxation $\tau_{mag2} \approx 540$ s. To confirm the magnetic time we plot the log of

the normalised conductivity after 1 min to allow time for the system to settle after quenching and obtain a single slow exponential with magnetic time, $\tau_{mag} \approx 500$ s.

7.7   Hall mobility, carrier concentration and the 2C model

The slow charge dynamics that cause the hysteresis of $\sigma_{xx}(V_g)$ observed in the $CsPbX_3$/graphene devices is affected by applied magnetic field (**Figure 7.8a**). In low fields ($B = 1$ T), we observe a small decrease in the hysteresis of the Dirac point, $\Delta V_g^{NP} \sim 2$ V, and a small decrease in the conductivity relative to zero field. However, at $B = 16$ T the $\sigma_{xx}(V_g)$-dependence is shallower, likely due to magnetic field induced confinement of charge carriers. The shape of $\sigma_{xx}(V_g)$ also changed dramatically with extra minima appearing on either side of the Dirac point, where the Fermi level, E_F, is in resonance with the $\nu = 2$ Landau level [216]. The magnetic field effect on ΔV_g^{NP} hysteresis can be seen from the voltage separation between the minima in $\sigma_{xx}(V_g)$ peaks for forward and reverse V_g sweeps (**Figure 7.8a**), which also corresponds to the point at which $R_H = \frac{R_{xy}}{B} = \frac{V_{xy}}{I_{sd}B} = 0$ and the conductivity in graphene changes polarity (**Figure 7.8b**).

Hall mobility, μ_H, was calculated from $\sigma_{xx}(V_g)$ (**Figure 7.8a**) and $R_H(V_g)$ (**Figure 7.8b**) using **Equation 3.16** and plotted as a function of V_g (**Figure 7.8c**). The $\mu_H(V_g)$ has a maximum value of $\mu_H = 31,000$ cm^2/Vs for the forward V_g sweep and $\mu_H = 19,000$ cm^2/Vs for the reverse sweep, which is on average $\sim 2\times$ higher than the field effect mobility calculated using the 1C linearisation model **Figure 7.8d**. This measurement also revealed an asymmetry in carrier mobility near the Dirac point (**Figure 7.8e**). The carrier concentration was extracted from $R_H(V_g)$ and compared to the 2C model (**Figure 7.8f**) with RC times $\tau_{RC} = 350$ s and $\tau_{RC} = 550$ s for $B = 1$ T and $B = 16$ T, respectively, which fits the data well, particularly at negative V_g values. We note that the fitting time for $B = 16$ T is very similar to the measured magnetic relaxation time $\tau_{mag} \sim 540$ s from **Figure 7.7f**. We are not aware of any experimental or theoretical studies of a 'magnetic

time' in graphene FETs and currently do not have a model for this effect.
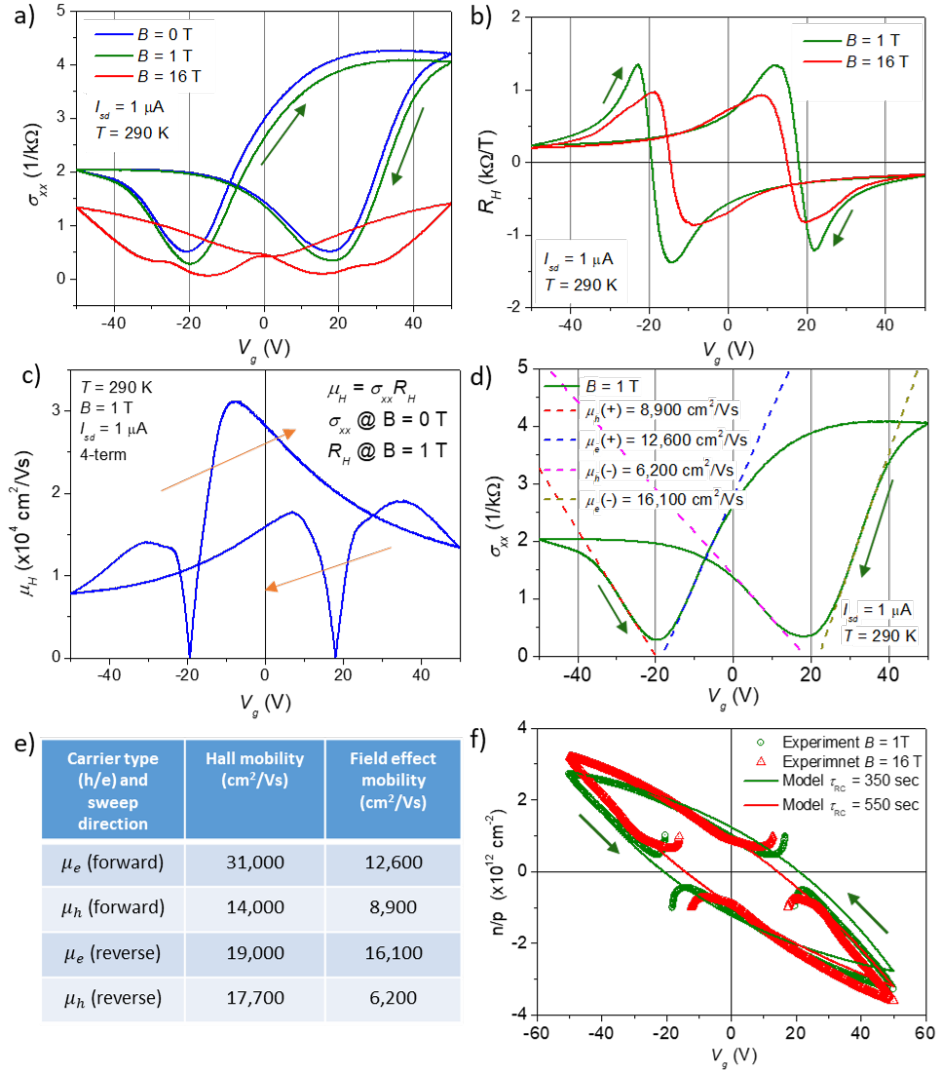
Figure 7.8. **a)** Dependence of σ_{xx} on applied V_g of the hybrid graphene/CsPb(Br/Cl)$_3$ device at $B = 0, 1$ T and 16 T ($T = 290$ K). Arrows indicate direction of V_g sweep. **b)** Hall resistance, R_H, versus V_g at $B = 1$ T and 16 T ($T = 290$ K). Arrows indicate direction of V_g sweep. **c)** Hall mobility, μ_H, as a function of V_g; calculated from the product of the $B = 0$ T longitudinal conductivity and the $B = 1$ T Hall resistance ($T = 290$ K). Arrows indicate direction of V_g sweep. **d)** $\sigma_{xx}(V_g)$ dependence and its linear fits at $B = 1$ T used to calculate field effect mobility of charge carriers near the Dirac point for forward (+) and reverse (-) sweeps (direction indicated by arrows). **e)** Summary of the measured Hall mobility and calculated field effect mobility of electrons and holes. **f)** Carrier concentration versus V_g at $B = 1$ T and 16 T calculated from the Hall effect measurements shown in **(b)** (data points) and calculated using the 2C model (solid lines). Arrows indicate direction of V_g sweep.

104

7.8 Summary

In this chapter we have studied fundamental properties of SLG decorated with $CsPb(Br/Cl)_3$ perovskites and the potential of these hybrid graphene-based structures for UV detection applications. We achieved high responsivity $R \approx 2 \times 10^6$ A/W in the spectral range below the absorption edge of the NCs (~ 460 nm) and deep into the UV (250 nm). However, the photocurrent in the device showed a complex behaviour with an initial increase in photocurrent followed by a fall in the current as the illumination power was increased. Unfortunately, we were unable to determine the cause of this secondary effect, which is reversible.

For the first time, we explored the effect of an applied magnetic field on perovskite/graphene FETs. We found that there is a measurable magnetic field dependent hysteresis in the Hall resistance of graphene fuctionalised with perovskite NCs, which is activated at temperatures above $T \approx 200$ K. We introduced a new characteristic time, namely 'magnetic time', which is relevant to the charge transfer processes in perovskite NC/graphene devices and mediated by the presence of an applied magnetic field; at $B = 16$ T this time was $\tau_{mag} = 500$ s. This effect is analogous to the charging/discharging processes in perovskite NC/graphene systems generated by electric field and light and this behaviour was in good agreement with the used 2C model. Thus, slow charge transfer processes in our perovskite/graphene devices can be associated with three different characteristic times, which are: optical, $\tau_{ph} \approx 10$ s; electric $\tau_{el} \approx 300$ s; and magnetic $\tau_{mag} \approx 500$ s for $CsPb(Br/Cl)_3$ NCs.

Complexity of the studied charge transfer processes and their dependence on electric and magnetic field sweeping rate as well as on the incident light and temperature was mitigated by the developed measurement techniques. For the first time, we used pulsed field ($B < 60$ T) facilities at LNCMI for instantaneous Hall measurements during uninterrupted cyclic sweeping of gate voltage. Mea-

surements in Nottingham in slowly (~ 4 mT/s) changing and constant B fields helped to verify the results obtained and accurately measure the magnetic time, τ_{mag}. Our findings and novel experimental techniques improve the understanding of charge transfer processes in graphene-based low-dimensional heterostructures.

8 Inkjet-printed graphene devices

This chapter reports on the characterisation of inkjet-printed graphene ink (iGraphene) and its use for scalable electronic and optoelectronic device applications. There are 4 main types of printed devices used in these studies: (i) individual printed droplets on patterned gold contacts (**Section 8.2.1**); (ii) multi-layer printed stripe devices (**Section 8.2.2**); (iii) hybrid perovskite/iGraphene devices (**Section 8.3**); and (iv) printed graphene as a contact material for other 2D materials (e.g. InSe) (**Section 8.4**). These 4 types of iGraphene devices demonstrate different transport behaviour, which is discussed throughout this chapter.

Inkjet-printed devices were provided by Dr. Feiran Wang and Mr Jonathan Austin from the Centre for Additive Manufacturing at the University of Nottingham.

8.1 Introduction

Liquid exfoliation offers an alternative method of producing 2D materials [218, 219], which can be formulated into printable inks for additive manufacturing technologies [220]. Inkjet printing offers a scalable route to device fabrication on various substrates, including flexible and/or stretchable substrates [221, 222] and wearable electronics [69, 223]. Of particular interest is the printing of multi-layer heterostructures and mixing of iGraphene with other low-dimensional materials (e.g. $CsPbI_3$ NCs [224]) for printable optoelectronics [69]. A fully inkjet-printed iGraphene/hBN transistor with silver nanoparticle contacts has already been realised with mobility, $\mu \approx 20$ cm^2/Vs [225] and graphene printed directly on a Si/SiO$_2$ substrate has reached $\mu \approx 95$ cm^2/Vs [226]. In general, the printed networks consist of disordered arrays of nanosheets, which show some degree of in-plane alignment [227]. The morphology can vary from closely packed to highly porous and depends on many factors including ink formulation, nanosheet size,

printing droplet size and drying conditions [226–228]. The network morphology determines the nature of the junctions connecting the individual nanosheets and is particularly important when looking at the transport of charge carriers through the network. In iGraphene networks the transport across junctions, referred to as inter-flake transport, is expected to be via quantum tunnelling or hopping across the tunnel barrier between flakes [229]. The transport within the flakes, or intra-flake transport, is likely to be similar to transport within single or few-layer graphene. The combination of the inter- and intra-flake conductivity determines the overall transport properties of the network. However, the transport mechanisms that govern the properties of these iGraphene networks are still largely unknown and to my knowledge a universal transport model has not yet been developed for iGraphene.

8.2 iGraphene FETs

8.2.1 Electrical properties of single- and multi-droplet iGraphene FETs

In this study, graphene inks containing liquid exfoliated few-layer graphene flakes (average size of 2590 nm^2) and ethyl cellulose (EC) dispersed in a cyclohexane/terpineol mixture were used for drop-on-demand inkjet printing (see **Section 4.2**). Where possible, the printed iGraphene devices were annealed at $T = 250$ °C in vacuum for 2 h to evaporate most of the solvent, reduce defect density in the graphitic lattice and improve interlayer organisation [225].

In order to characterise the electrical properties of the type (i) iGraphene a single droplet was printed onto pre-patterned interdigitated gold contacts on Si/SiO$_2$ (OFET) (inset of **Figure 8.1a**). These devices provide an excellent platform for creating electrical contacts to a single droplet and allow measurements of the resistance as a function of gate voltage, $R_{sd}(V_g)$, of the channel, comparable to a standard graphene FET. R_{sd} was calculated from two-terminal measurements
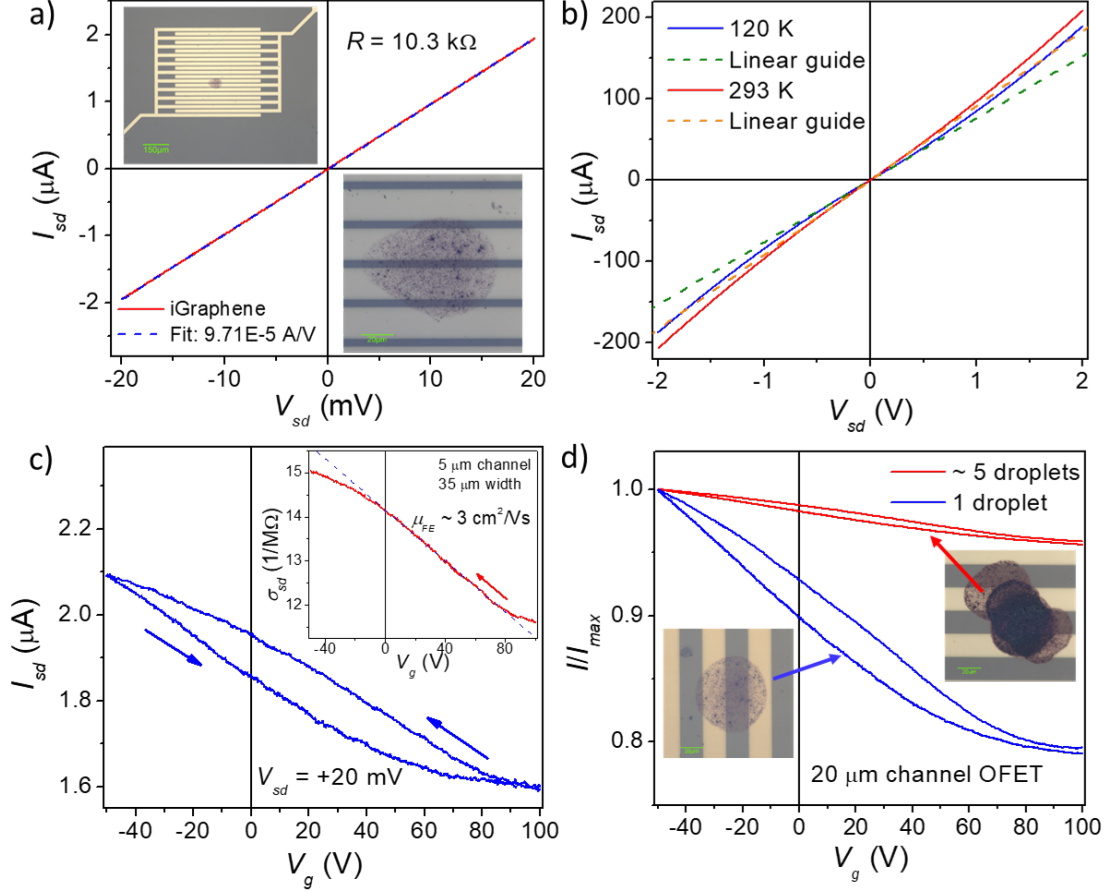
Figure 8.1. **a)** Current versus applied voltage for a single graphene inkjet-printed droplet on 5 μm channel OFET at room temperature ($T =$ 293 K) with calculated resistance, $R = 10.3$ kΩ. Inset: Optical images of the device and higher magnification of the droplet. **b)** Current versus applied voltage for the same device with increased voltage range ($V_{sd} = \pm 2$ V) at $T = 120$ K and $T = 293$ K. **c)** Current versus applied gate voltage for the same device with applied source-drain bias, $V_{sd} = 20$ mV (arrows indicate sweep direction). Inset: conductivity of reverse sweep using smallest channel width ($w = 35$ μm) and calculated field effect mobility, $\mu_{FE} = 3$ cm^2/Vs. **d)** Normalised current versus gate voltage for 1 droplet and ~ 5 droplet devices on 20 μm channel OFETs. Insets: optical images of corresponding inkjet-printed droplet devices.

of I_{sd} and so the resistance could be affected by the contact resistance. For the single droplet deposited onto a 5 μm channel-width OFET the $I_{sd}(V_{sd})$ has a linear dependence for $V_{sd} = \pm 20$ mV and the resistance was $R_{sd} = 10.3$ kΩ at $T = 293$ K (**Figure 8.1a**). However, under larger applied bias, $V_{sd} = \pm 2$ V, the current shows non-Ohmic behaviour with a deviation from linearity of $\sim 14\%$ at $V_{sd} = 2$ V (**Figure 8.1b**). This could be due to the contribution of the inter-flake transport [225, 230, 231]. At lower temperature, $T = 120$ K, the measured current is re-

109

duced and more pronounced non-linearity is observed ($\sim 24\%$ at $V_{sd} = 2$ V). This is likely due to the suppression of inter-flake charge transfer at low temperature.

Effect of applied gate voltage was studied within the linear range of $I_{sd}(V_{sd})$, at $V_{sd} = 20$ mV. The shape of the $I_{sd}(V_g)$ curve for iGraphene resembles that of a CVD graphene FET with a typical conductivity minimum in positive V_g, corresponding to heavy p-doping effects [232]. Note that we observe this behaviour despite iGraphene being a network of many small, randomly oriented flakes (**Figure 8.1c**). There is an indication of hysteresis in the forward and reverse sweep. We assume that the conductivity minimum is analogous to the Dirac point in single layer graphene, hence, we conclude that the graphene is heavily p-type doped ($p > 7 \times 10^{12}$ cm^{-2}). We attribute the doping to the presence of organic residues from the ink. The mobility calculated for this device using the field effect model is $\mu_{FE} \approx 3$ cm^2/Vs, which is of the same order of magnitude with the reported values in literature [69, 226]. Note that this is just a single droplet device, which might not provide an optimal continuous network of graphene flakes. Thus, we examine a device produced with multiple (~ 5) droplets deposited onto a 20 μm channel OFET (**Figure 8.1d**). The 5-droplet device is more likely to have a thickness of 3-4 droplets as there is some uncertainty in the precision of drop deposition (see inset of **Figure 8.1d**). A strong decrease in the effect of applied V_g is observed in the multi-droplet device compared to the single droplet, which can be ascribed to an increase in electric field screening as the density of graphene flakes increases. We envisage that the electric field is likely to be screened by the bottom few layers of iGraphene.

8.2.2 iGraphene stripes

To explore the charge transport through continuous packed iGraphene, the electrical properties of ≥ 5 layer devices (type (ii)) were studied (**Figure 8.2a**). Note that type (ii) iGraphene devices with thickness < 5 printed layers demon-
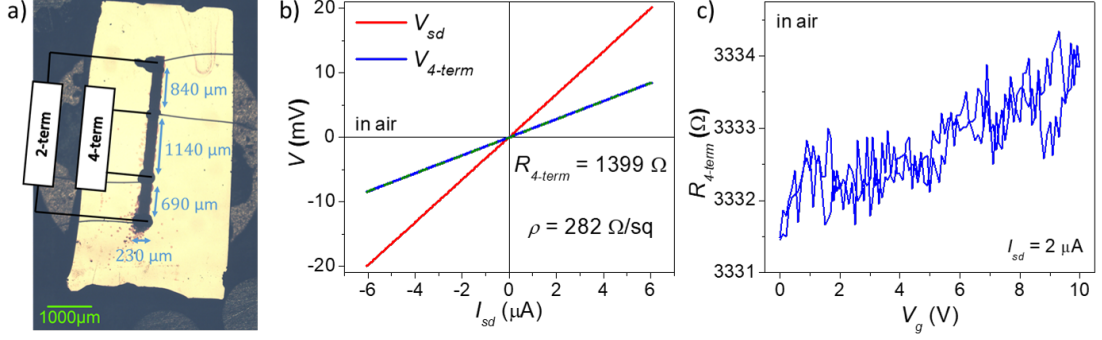
Figure 8.2. a) Optical image of 5-layer inkjet-printed device on Si/SiO$_2$ substrate with measurement scheme and sample dimensions. **b)** Current-voltage dependence measured in 2-terminal and 4-terminal configuration in air ($T = 293$ K) with calculated resistivity, $\rho \approx 280$ Ω/sq. **c)** Dependence of 4-terminal resistance on gate voltage ($I_{sd} = 2$ μA).

strate irreproducible conductivity varying in a very large range (from ~ 100 Ω to >1 MΩ) [225, 233]. The 4-terminal resistance measurements revealed resistivity, $\rho \approx 280$ Ω/sq (**Figure 8.2b**), which is lower than that of a single drop device, suggesting that the packing fraction, or flake density, is higher [225]. This device showed no gate voltage dependence of resistance as the 5-layers are thick enough to screen the electric field completely (**Figure 8.2c**). Note that the density of graphene flakes in the stripe devices is, in general, higher than in droplet devices with the same number of layers, as the stripes are printed in continuous lines with overlapping droplets (drop spacing of 20 μm and droplet size ~ 70 μm). This higher flake density can be the reason for the very low gate voltage dependence and high conductivity in type (ii) iGraphene, see **Figure 8.2c**.

8.2.3   Temperature dependent transport

Preliminary temperature dependent measurements were performed in order to gain insight into the dominant transport mechanisms in iGraphene devices. For the single droplet on 5 μm OFET channel (**Section 8.2.1**), the $I_{sd}(V_g)$ dependence was measured at different temperatures from $T = 105$ K to 350 K (**Figure 8.3a**). Similar to pristine CVD graphene, hysteresis of $I_{sd}(V_g)$ at low temperature is reduced significantly. We ascribe this behaviour to the defect charge trap states
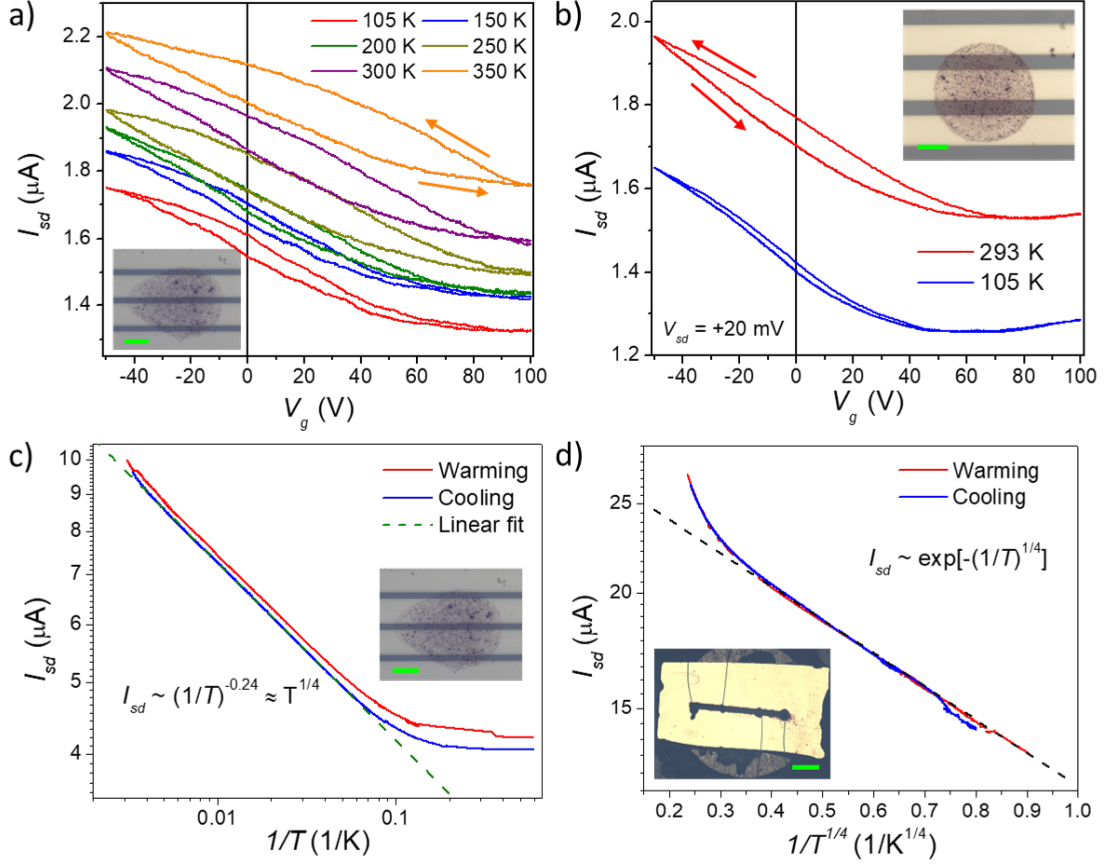
Figure 8.3. a) Dependence of source-drain current, I_{sd}, on applied gate voltage, V_g, of a single iGraphene droplet on 5 μm OFET device at different temperatures from $T = 105$ K to 350 K ($V_{sd} = 20$ mV). Arrows indicate direction of V_g sweep. Inset: optical image of the single droplet printed on an OFET with 5 μm channel width (scale bar: 20 μm). **b)** $I_{sd}(V_g)$ of a single iGraphene droplet on 10 μm OFET device at $T = 293$ K and 105 K ($V_{sd} = 20$ mV). Arrows indicate direction of V_g sweep. Inset: optical image of the single droplet printed on an OFET with 10 μm channel width (scale bar: 20 μm). **c)** Dependence of I_{sd} on $1/T$ of a single droplet on 5 μm OFET device plotted on a log-log scale graph with a linear power law fit $I_{sd} \sim T^{1/4}$. Inset: optical image of the single droplet device measured for reference (scale bar: 20 μm). **d)** I_{sd} plotted against $(1/T)^{1/4}$ of a 5-layer stripe device on a semi-log scale with a linear fit $I_{sd} \sim \exp\left[-(1/T)^{1/4}\right]$ at low temperature. Inset: optical image of the 5-layer stripe device measured for reference (scale bar: 1000 μm).

freezing out as temperature is reduced. However, in single layer graphene the Dirac point position is independent on temperature and $R(V_g)$ becomes narrower at lower temperatures due to increased carrier mobility [234, 235]. In contrast, the Dirac point of the iGraphene FET appears to be shifting towards n-type with decreasing temperature and is accompanied by broadening of the $I_{sd}(V_g)$ curve

112

(**Figure 8.3a,b**). The n-type shift of the Dirac point is more pronounced in a single droplet on 10 μm OFET channel as the Dirac point is at lower V_g and can be fully observed at $T = 293$ K and 105 K (**Figure 8.3b**). Reduced hysteresis is observed at low temperature and accompanied by an n-type shift in the gate voltage of the Dirac point by $\Delta V_g^{NP} \approx 20$ V. It is important to note that the origin of the heavy p-doping effect observed in our iGraphene devices is not yet confirmed. Thus, the decrease of p-doping at low temperatures could be related to freezing of charged defect states in the iGraphene. We plan further studies of this effect using different ink formulations.

The temperature dependence of the current measured for the single droplet is plotted in **Figure 8.3c**. The conductivity is proportional to $\sim T^{1/4}$ in the temperature range from $T = 10$ K to 300 K and remains unchanged for $T < 10$ K. In contrast, for the thick, 5-layer graphene stripe the T-induced change of conductivity occurs at low temperatures $T < 40$ K (**Figure 8.3d**), and can be explained by the Mott variable range hopping model for a strongly disordered 3D system [236, 237]. In this model the conductivity is

$$\sigma \propto \exp\left[-(1/T)^{1/(\beta+1)}\right] \tag{8.1}$$

where $\beta = 3$ is the number of spatial dimensions of the system. The temperature dependence of transport in the iGraphene network is rather complex and work is ongoing to develop a comprehensive theoretical model to describe the observed behaviour. We attribute the difference in $\sigma(T)$ behaviour for a single drop and a 5-layer (bulk) sample to the increased role of inter-flake transport in the low density droplets compared to thick stripes.

8.2.4 iGraphene in high magnetic field

To further unpick the charge transport in iGraphene we also measured the magnetic field dependence of both a single droplet OFET device with 5 μm channel width (**Figure 8.4a**) and the 5-layer stripe device (**Figure 8.4b**). The percentage change of resistance, ΔR, relative to the resistance in zero field, $R_{(B=0)}$, is measured as a function of the externally applied magnetic field perpendicular to the sample surface at different temperatures (**Figure 8.4a,b**).

For both samples in magnetic fields $B < 10$ T we observe negative magnetoresistance behaviour with a distinct weak localisation (WL) peak at $B = 0$ T, similar to that observed in mechanically exfoliated few layer graphene [238, 239] and in 80-layer printed iGraphene [240]. The observation of quantum phenomenon, such as WL, in these disordered flake networks is unexpected. Typically, WL in high quality single layer graphene decreases rapidly in small fields of $B = 10 - 200$ mT [241, 242] and, as the system becomes more disordered and mobility decreases, the localisation peak extends to higher magnetic fields [243]. The much larger ($\times 100$) WL critical magnetic field ($\sim 3 - 15$ T) observed in iGraphene could be due to smaller radius of quantised electron trajectories allowed in iGraphene,
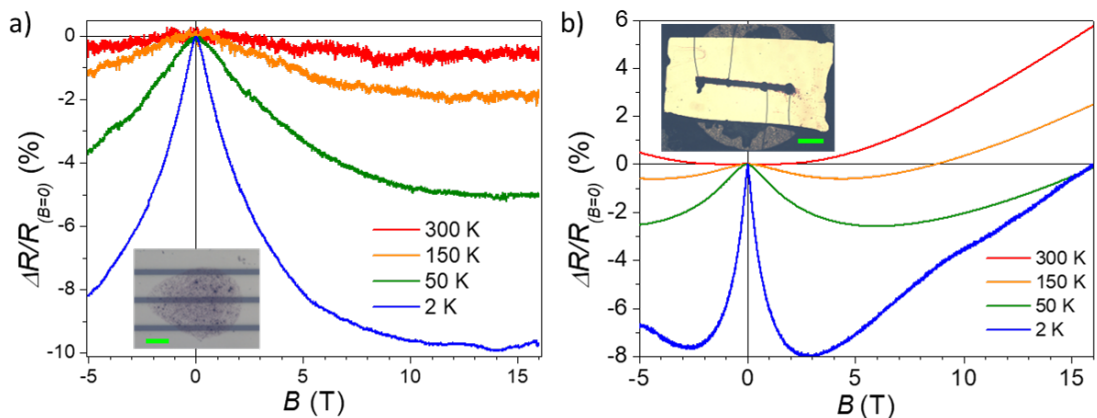
Figure 8.4. Relative change of magnetoresistance, $\Delta R = R - R_{(B=0)}$, in a perpendicularly applied magnetic field, B, as a function of the externally applied magnetic field at different temperatures for **a)** the single droplet (scale bar: 20 μm) and **b)** the 5-layer stripe devices (scale bar: 1000 μm), as shown in the figure insets.

114

required for the observation of quantum effects in such a disordered system. We plan further studies of WL phenomena in iGraphene, which also requires better understanding of carrier transport in this system.

8.3   iGraphene/perovskite photodetector

To demonstrate the potential of iGraphene networks for applications in functional devices we drop-cast perovskite $CsPb(Br:I=2:3)_3$ NCs onto a single inkjet-printed droplet on a 20 μm channel OFET device (**Figure 8.5a**). In this device (type (iii)), the iGraphene droplet is placed only between one pair of contacts, which makes measurements more defined. The orange photoluminescence of the perovskite NCs can be observed on the device under excitation with $\lambda_{ex} = 520$ nm (**Figure 8.5a**). The iGraphene has a Dirac point at $V_g^{NP} \approx 60$ V and mobility, $\mu_{FE} \approx 3$ cm^2/Vs (**Figure 8.5b**). Deposition of the perovskite NCs causes an n-type shift of the Dirac point by $\Delta V_g^{NP} \approx 10$ V (similar to perovskite NCs deposited on CVD graphene (**Section 5.3**)), a small ($\sim 7\%$) reduction in conductivity (by ~ 1.5 MΩ^{-1}) of the device and no noticeable change for the $\mu_{FE} = 3$ cm^2/Vs mobility. This result confirms that semiconductor NCs in hexane solution can be deposited on very low density (single droplet) iGraphene without damaging its integrity and electronic properties.

After deposition the device becomes photoresponsive in the wavelength range below the band edge of the perovskite NCs, $\lambda_{PL} \sim 605$ nm (**Figure 8.5c**). The highest photosensitivity was measured under exposure to green ($\lambda_{ex} = 520$ nm) laser light with maximum photoresponsivity $R \approx 15$ A/W (**Figure 8.5d**). The $\sim 10^4$ drop of the photoresponsivity compared to SLG/perovskite detectors (**Section 5.6**) is likely due to the low mobility of the iGraphene as responsivity is inversely proportional to the transit time of the charge carriers, $1/\tau_{transit}$ (**Equation 2.4**), which is directly proportional to the carrier mobility. Therefore, a factor of $\sim 10^4$ lower mobility can explain the $\sim 10^4$ times lower
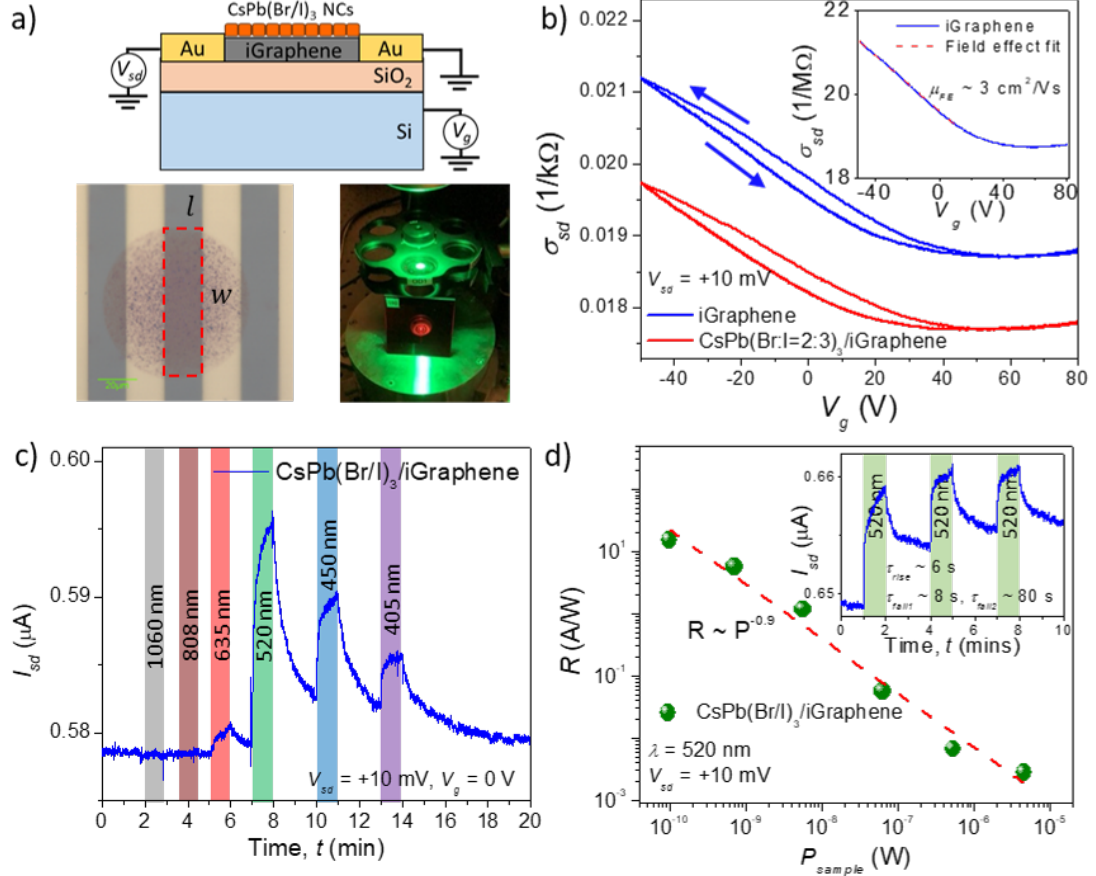
Figure 8.5. **a)** Schematic of CsPb(Br:I=2:3)$_3$/iGraphene FET photodetector (top) with optical images of the iGraphene droplet printed on the OFET device (left) and the same device after deposition of CsPb(Br:I=2:3)$_3$ NCs under illumination with λ_{ex} = 520 nm (right). A longpass filter (λ = 590 nm) is used to observe the orange photoluminescence of the NCs. **b)** Conductivity before (blue curve) and after (red curve) deposition of CsPb(Br:I=2:3)$_3$ NCs. Arrows indicate direction of V_g sweep. Inset: Gate voltage dependence of conductivity and its linear fit, used for field effect mobility ($\mu_{FE} \sim 3$ cm^2/Vs). **c)** Temporal dependence of I_{sd} of CsPb(Br:I=2:3)$_3$/iGraphene photodetector under illumination with different laser wavelengths (P = 0.56 mW/mm^2). **d)** Photoresponsivity as a function of the power on the sample (λ_{ex} = 520 nm). Inset: temporal response of device under ON-OFF cycles of illumination (λ_{ex} = 520 nm, P = 5.6 mW/mm^2).

responsivity in the iGraphene/perovskite detector. However, response time of iGraphene/perovskite ($\tau_{rise} \sim 6$ s and $\tau_{fall} \sim 8$ s) is similar to SLG/perovskite devices ($\tau_{rise} \sim 1$ s and $\tau_{fall} \sim 3.5$ s, see **Figure 5.10a**). The response time is likely dominated by the charge trapping time in the NCs and the transfer time of photoexcited charges into the conductive channel [244, 245]. These are both prop-

erties of the NCs themselves and thus, response time is comparable for iGraphene and SLG. This finding opens interesting prospects for the use of iGraphene in large scale fully printed photon detectors.
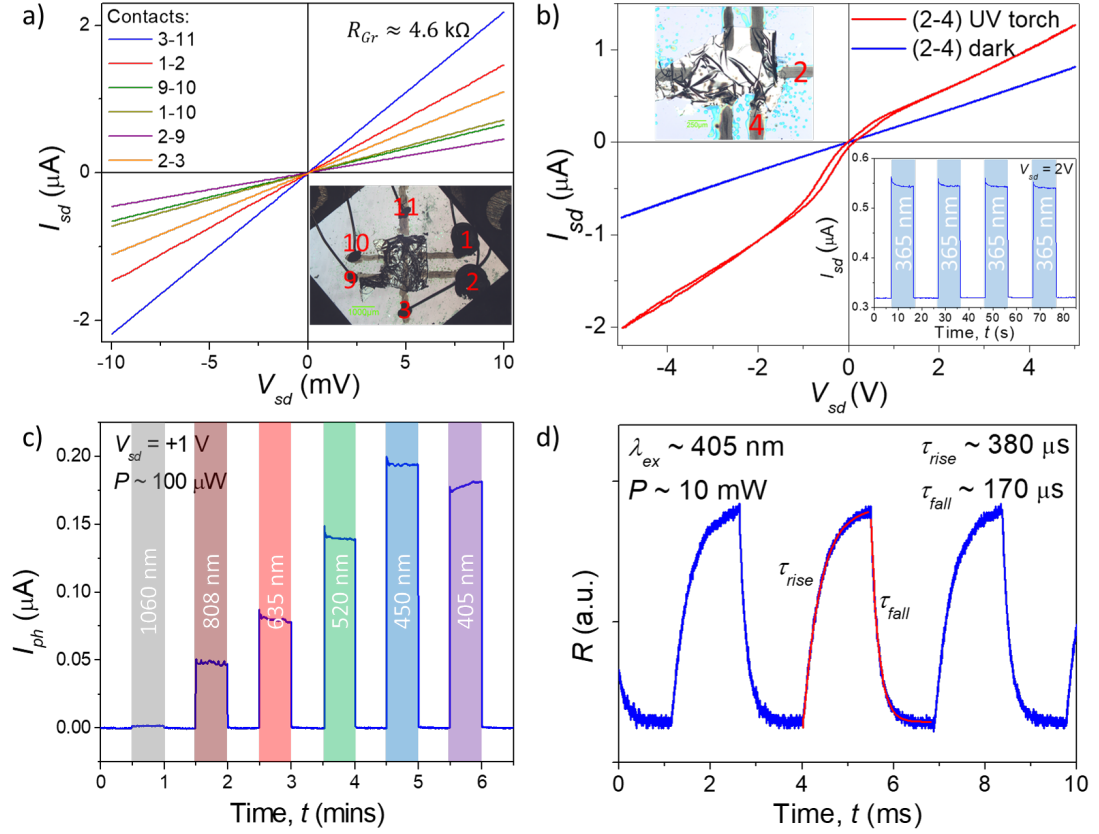
Figure 8.6. a) Linear current-voltage measurements for different combinations of iGraphene contacts on bulk InSe. Inset: optical image of the device with contact numbers. **b)** Current-voltage measurements of a similar iGraphene/InSe device (optical image in top inset) in the dark and under UV ($\lambda_{ex} = 365$ nm) excitation. Bottom inset: Reproducibility of current between contacts 2 and 4 under ON-OFF UV ($\lambda_{ex} = 365$ nm) excitation cycles. Light ON represented by blue blocks. **c)** Photocurrent, I_{ph}, against time under ON-OFF illumination with different excitation wavelengths denoted by coloured blocks. **d)** Fast oscilloscope measurement of response time of the iGraphene/InSe detector using high power ($P = 10$ mW) $\lambda_{ex} = 405$ nm excitation with digital ON-OFF switching frequency, $f = 348$ Hz.

8.4 iGraphene contacts to InSe photodetector

Finally, we demonstrate the use of iGraphene as an electrical contact material for different devices (type (iv)). Here, we use a bulk flake of InSe (Area ~ 1 mm^2, thickness > 1 μm) and contacted it with iGraphene in a Hall bar style configuration (inset of **Figure 8.6a**). The iGraphene makes good Ohmic (linear I-V) contacts to the InSe flake (**Figure 8.6a,b**). Note that it is rather difficult to make an Ohmic contact to InSe flakes using conventional 3D materials, such as metal films [246]. A similar device was used for optical measurements and shows a linear I-V relationship in the dark, but becomes non-linear under illumination with a UV ($\lambda_{ex} = 365$ nm) torch. The absorption edge of bulk InSe at room temperature is ~ 1.1 eV (≈ 1130 nm) [247] and the device is responsive at wavelengths below this value (**Figure 8.6c**). The photocurrent in the device, I_{ph}, increases at lower wavelengths due to the increased absorption of InSe at higher energies. Response times in this device geometry are much faster than hybrid planar devices (e.g. perovskite/graphene) with rise and fall times of $\tau_{rise} = 380$ μs and $\tau_{fall} = 170$ μs, respectively (**Figure 8.6d**). These times are similar to previously reported values for single layer graphene/InSe devices [78]. Fast optical response times were measured using an oscilloscope and digitally modulated laser ($\lambda_{ex} = 405$ nm), as described in **Section 4.8.2**.

8.5 Summary

In this chapter we have performed preliminary investigations of the transport properties of iGraphene and demonstrated some potential applications from photodetectors to electrical contacts to other 2D materials. The network of small few-layer graphene flakes formed by inkjet-printing of the graphene ink creates a conductive channel and displays gate controllable source-drain current and a dip in conductivity similar to the Dirac point in SLG. However, iGraphene has very

low charge carrier mobility $\mu_{FE} \sim 3 \ \mathrm{cm}^2/\mathrm{Vs}$ due to the vastly increased scattering introduced by the network of randomly orientated flakes and potential barriers introduced by gaps between flakes.

The iGraphene FET was used to make a hybrid perovskite NC/iGraphene photodetector with relatively low responsivity, $R \approx 15$ A/W and response time $\tau \sim 8$ s similar to SLG-based detectors of the same geometry. iGraphene can also be used to make Ohmic contacts with other materials. Here, we demonstrated its use as contacts to bulk InSe in a fast ($\tau < 1$ ms) UV-Vis photodetector.

The dominant transport mechanisms involved in the network of flakes for iGraphene is still a topic that is up for debate. We showed that the device can behave very differently depending on the density of flakes and the deposition technique (individual droplets or stripes). We also observed a strong negative magnetoresistance in an externally applied magnetic field and a quantum weak localisation effect.

It is important to note that we are at an early stage of iGraphene development. There is still a number of open questions, such as the dominating type of conductivity and its temperature dependence, which is in good agreement with variable range hopping model in stripe devices, but very different in the droplet ones. Preliminary results presented here demonstrate that iGraphene is a novel material with pronounced quantum behaviour and potential for a large number of possible applications.

9 Conclusions and outlook

The primary objectives of this PhD thesis were to investigate the functionalisation of graphene field effect transistors with perovskite NCs and demonstrate their potential for UV-Vis photodetection applications. However, the scope of the project has widened and adapted considerably as a number of new phenomena, such as the 'giant' $R(V_g)$ hysteresis of perovskite/graphene devices and the optically-induced Stark effect associated with perovskite NCs were uncovered during in-depth material and device studies. We also significantly expanded the breadth of studied low-dimensional materials and fabrication techniques from conventional lithography, exfoliation and CVD towards additive manufacturing and inkjet printing. These novel materials and devices required a new approach to their modelling, leading to the development of a 2C model for perovskite/graphene FETs and new transport models (still under development) for iGraphene. The key findings that I consider the most important and prospective for future studies are summarised below:

(i) We found that graphene functionalised with all-inorganic halide perovskite NCs shows high photoresponsivity ($R > 10^7$ A/W) in the UV-Vis range and we were able to tune the spectral range of the detectors through the halide content of the perovskite NCs. The $CsPb(Br/Cl)_3$ NC/graphene device provides an almost UV-specific silicon-compatible photodetector and with some more composition engineering of the perovskites a UV-only detector is just over the horizon. However, silicon-compatible UV-detection might not be the best route to take as throughout these studies we found parasitic photocurrent caused by Si/SiO_2 substrates detrimental to device performance under high illumination powers. Thus, further investigations into graphene/perovskite device performance on other substrates, such as sapphire, would be beneficial for high sensitivity UV detectors.

(ii) We discovered that planar perovskite/graphene devices exhibit anomolously

large $R(V_g)$ hysteresis and through temperature dependence studies of the hysteresis we uncovered an activation energy of ~ 0.3 eV. The activation energy was found to be consistent for all $CsPbX_3$ NCs measured and independent of the halide composition. This result coupled with measurements of a device with Sn-doped NCs, which showed a significantly different activation energy of ~ 0.6 eV, led us to believe that the deep defect level was associated with Pb-related states in the NCs. The $R(V_g)$ hysteresis present in these devices required us to rethink the charge dynamics within the graphene FET and motivated the development of the 2C model. This model has become a powerful tool in describing the behaviour of graphene functionalised with not just perovskite NCs, but other materials such as the ferroelectric CIPS. Further studies on charge dynamics at the graphene/perovskite interface, such as the effects of different ligands on the charging/discharging time could allow further development of the model to determine the roots of the RC fitting parameter. In turn, perhaps the 2C model can then be used to predict the behaviour of various 2D systems with slow charge traps and thus can be used for engineering of hybrid functionalised graphene devices.

(iii) High magnetic field measurements allowed us to complete the picture in terms of perovskite charging/discharging times. In this thesis I have determined 3 characteristic times for perovskite NC/graphene systems: optical (~ 10 s); electrical (~ 300 s); and magnetic (~ 500 s). This approach provides versatile tools for experimental studies of complicated charge dynamics responsible for the performance of these novel materials and devices.

(iv) Another key result from these studies is the fully reversible optically induced Stark effect observed in $CsPbX_3$ NCs. This effect is caused by the formation of positive charges on the surface of the NCs and results in a quenching of the PL signal that is accompanied by a red shift of the PL peak position. This effect is supported by the behaviour of photocurrent in perovskite/graphene hybrid devices and provides another tool for probing the charge dynamics of these sys-

tems. Further investigations including simultaneous microPL and photocurrent measurements on a single layer of perovskite NCs on graphene or a single NC on a narrow (~ 20 nm) graphene strip would help to deepen our understanding of how the charge dynamics in the NC affects the hybrid device. This would give a method of directly comparing the possible relationship between PL quenching of the NCs and photocurrent in the graphene, as well as enabling an investigation of the effects of gate voltage on the extraction of charges from individual NCs.

(v) We have presented an additive manufacturing approach to device fabrication using inkjet-printed iGraphene. Characterisation of iGraphene FETs found a comparable gate voltage dependence of resistance to SLG, which is strongly affected by the layer thickness of iGraphene. In the iGraphene networks the $\sim 10^4$ times lower charge carrier mobility compared to CVD graphene can be explained by the increased resistance due to the combination of inter- and intra-flake transport within the network of flakes. These systems are still in their infancy and a comprehensive transport model has not yet been developed. Nonetheless, we successfully produced a hybrid perovskite NC/iGraphene photodetector with similar properties to the perovskite/SLG devices, albeit with low responsivity (~ 15 A/W) due to the low iGraphene mobility. We also showed that iGraphene can be used as an Ohmic contact for other materials such as exfoliated InSe, which has fast photoresponse ($\tau < 1$ ms) in the UV-Vis range. Interestingly, we also found that iGraphene exhibits strong negative magnetoresistance with a distinct peak at zero magnetic field that is described in literature as weak localisation. There are many possible routes for further studies with these iGraphene devices. More in-depth and rigorous temperature studies are required to help determine the dominant transport mechanisms in order to develop a model for these flake network systems, which could direct efforts into better quality graphene inks that can emulate single or few layer graphene. Another avenue is to incorporate perovskite NCs into the iGraphene ink to make a hybrid photosensitive ink that can be printed on flexible or wearable substrates. The possibility of quantum effects

such as weak localisation in the iGraphene networks is also intriguing and further magnetic field studies to probe the intra-flake transport could be key to understanding this effect.

Overall, the studies presented in this thesis have helped to deepen our understanding of functionalised graphene systems and graphene-based UV-Vis photodetection. These hybrid perovskite NC/graphene devices display complex charge dynamics and we have attempted to unravel and model their behaviour under excitation with optical, electrical and magnetic fields. They offer great potential for photon detection with already excellent optoelectronic properties including high photoresponsivity and tunable spectral response. With further development of the perovskite/graphene interface through perovskite composition, ligand engineering and the new possibilities of inkjet printing, who knows what the future holds?

References

1. M. Y. Li, S. K. Su, H. S. Wong, L. J. Li, *Nature 2021 567:7747* **567**, 169–170, ISSN: 14764687, (https://www.nature.com/articles/d41586-019-00793-8) (Mar. 2019).

2. S. Sze, K. K. Ng, *Physics of Semiconductor Devices* (John Wiley & Sons, Inc., Hoboken, NJ, USA, Oct. 2006), ISBN: 9780470068328.

3. J. H. Davies, *The Physics of Low-dimensional Semiconductors* (Cambridge University Press, New York, NY, USA, 1998).

4. L. Redaelli *et al.*, *Applied Physics Letters* **105**, 131105, ISSN: 0003-6951 (Sept. 2014).

5. K. S. Novoselov *et al.*, *Science* **306**, 666–669, ISSN: 0036-8075 (Oct. 2004).

6. P. Avouris, T. F. Heinz, T. Low, *2D Materials: Properties and Devices*, 1–504, (https://www.cambridge.org/core/books/2d-materials/A87B3521C3A8A5885319F58E6F387830) (Jan. 2017).

7. P. Ajayan, P. Kim, K. Banerjee, *Physics Today* **69**, 38, ISSN: 0031-9228, (https://physicstoday.scitation.org/doi/abs/10.1063/PT.3.3297) (Aug. 2016).

8. A. K. Geim, I. V. Grigorieva, *Nature* **499**, 419–425, ISSN: 0028-0836 (July 2013).

9. Y. Liu *et al.*, *Nature Reviews Materials* **1**, 16042, ISSN: 2058-8437 (Sept. 2016).

10. K. S. Novoselov, A. Mishchenko, A. Carvalho, A. H. Castro Neto, *Science* **353**, ISSN: 0036-8075 (July 2016).

11. C. Li, P. Zhou, D. W. Zhang, *Journal of Semiconductors* **38**, 031005, ISSN: 1674-4926 (Mar. 2017).

12. Y. Zhao, K. Zhu, *Chemical Society Reviews* **45**, 655–689, ISSN: 0306-0012 (2016).

13. Q. Chen *et al.*, *Nano Today* **10**, 355–396, ISSN: 17480132 (June 2015).

14. L. Protesescu *et al.*, *Nano Lett* **15**, 3692–3696, ISSN: 1530-6992 (Electronic) 1530-6984 (Linking), (https://www.ncbi.nlm.nih.gov/pubmed/25633588) (2015).

15. B. Li *et al.*, *Nat Commun* **9**, 1076, ISSN: 2041-1723 (Electronic) 2041-1723 (Linking), (https://www.ncbi.nlm.nih.gov/pubmed/29540764) (2018).

16. Z. Lin *et al.*, *Advanced Functional Materials* **28**, 1805214, ISSN: 1616-301X, (https://onlinelibrary.wiley.com/doi/abs/10.1002/adfm.201805214) (2018).

17. J. Lu *et al.*, *Adv Mater* **29**, ISSN: 1521-4095 (Electronic) 0935-9648 (Linking), (https://www.ncbi.nlm.nih.gov/pubmed/28370588) (2017).

18. C. Zhang *et al.*, *Advanced Functional Materials* **30**, 1910582, ISSN: 1616-301X, (https://onlinelibrary.wiley.com/doi/abs/10.1002/adfm.201910582) (2020).

19. V. V. Brus *et al.*, *Advanced Materials Interfaces* **5**, 1800826, ISSN: 2196-7350, (https://onlinelibrary.wiley.com/doi/abs/10.1002/admi.201800826) (2018).

20. M. Gong *et al.*, *ACS Nano* **13**, 1772–1783, ISSN: 1936-086X (Electronic) 1936-0851 (Linking), (https://www.ncbi.nlm.nih.gov/pubmed/30689349) (2019).

21. J. He *et al.*, *The Journal of Physical Chemistry C* **123**, 7158–7165, ISSN: 1932-7447, (https://doi.org/10.1021/acs.jpcc.8b12350) (2019).

22. J. Wang *et al.*, *Nat Commun* **11**, 177, ISSN: 2041-1723 (Electronic) 2041-1723 (Linking), (https://www.ncbi.nlm.nih.gov/pubmed/31924773) (2020).

23. M. Cao *et al.*, *Journal of Materials Chemistry C* **7**, 14412–14440, ISSN: 2050-7526, (http://dx.doi.org/10.1039/C9TC03978C) (2019).

24. C. Zhang *et al.*, *Nanoscale* **11**, 13450–13457, ISSN: 2040-3364, (http://dx.doi.org/10.1039/C9NR03707A) (2019).

25. S. Wu, L. Cheng, Q. Wang, *Materials Research Express* **4**, 085017, ISSN: 2053-1591 (Aug. 2017).

26. G. Iannaccone, F. Bonaccorso, L. Colombo, G. Fiori, *Nature Nanotechnology* **13**, 183–191, ISSN: 1748-3387 (Mar. 2018).

27. H. Wang, Y. Wu, C. Cong, J. Shang, T. Yu, *ACS Nano* **4**, 7221–7228, ISSN: 19360851 (Dec. 2010).

28. V. W. Brar, M. C. Sherrott, D. Jariwala, *Chemical Society Reviews* **47**, 6824–6844, ISSN: 0306-0012 (2018).

29. K. Roy *et al.*, *Nature Nanotechnology* **8**, 826–830, ISSN: 1748-3387 (Nov. 2013).

30. L. Britnell *et al.*, *Science* **340**, 1311–1314, ISSN: 0036-8075 (June 2013).

31. R. Cheng *et al.*, *Nano Letters* **14**, 5590–5597, ISSN: 1530-6984 (Oct. 2014).

32. F. Withers *et al.*, *Nano Letters* **15**, 8223–8228, ISSN: 1530-6984 (Dec. 2015).

33. Z. R. Kudrynskyi *et al.*, *Communications Physics* **3**, 16, ISSN: 2399-3650 (Dec. 2020).

34. M. Yankowitz *et al.*, *Nature Physics* **8**, 382–386, ISSN: 1745-2473 (May 2012).

35. L. J. McGilly *et al.*, *Nature Nanotechnology* **15**, 580–584, ISSN: 1748-3387 (July 2020).

36. Z. R. Kudrynskyi *et al.*, *Physical Review Letters* **119**, 157701, ISSN: 10797114, (https://journals.aps.org/prl/abstract/10.1103/PhysRevLett.119.157701) (Oct. 2017).

37. Y. Cao *et al.*, *Nature* **556**, 43–50, ISSN: 0028-0836 (Apr. 2018).

38. M. Wojtaszek, H. Jonkman, (https://www.researchgate.net/publication/267771896_Graphene_a_two_type_charge_carrier_system) (July 2009).

39. Ponor, *Graphene - sigma and pi bonds*, July 2020, (https://commons.wikimedia.org/w/index.php?curid=92461297).

40. A. K. Geim, K. S. Novoselov, *Nature Materials* **6**, 183–191, ISSN: 1476-1122 (Mar. 2007).

41. Y. Zhu *et al.*, *Advanced Materials* **22**, 3906–3924, ISSN: 09359648 (Sept. 2010).

42. J.-H. Chen, C. Jang, S. Xiao, M. Ishigami, M. S. Fuhrer, *Nature Nanotechnology* **3**, 206–209, ISSN: 1748-3387 (Apr. 2008).

43. M. Sang, J. Shin, K. Kim, K. Yu, *Nanomaterials* **9**, 374, ISSN: 2079-4991 (Mar. 2019).

44. A. H. Castro Neto, F. Guinea, N. M. R. Peres, K. S. Novoselov, A. K. Geim, *Reviews of Modern Physics* **81**, 109–162, ISSN: 0034-6861 (Jan. 2009).

45. S. V. Morozov *et al.*, *Physical Review Letters* **100**, 016602, ISSN: 0031-9007 (Jan. 2008).

46. A. Van Bommel, J. Crombeen, A. Van Tooren, *Surface Science* **48**, 463–472, ISSN: 00396028 (Mar. 1975).

47. C. Berger *et al.*, *The Journal of Physical Chemistry B* **108**, 19912–19916, ISSN: 1520-6106 (Dec. 2004).

48. W. A. de Heer *et al.*, *Proceedings of the National Academy of Sciences* **108**, 16900–16905, ISSN: 0027-8424 (Oct. 2011).

49. L. Gao *et al.*, *Applied Physics Letters* **97**, 183109, ISSN: 0003-6951 (Nov. 2010).

50. Z. Cai, B. Liu, X. Zou, H.-M. Cheng, *Chemical Reviews* **118**, 6091–6133, ISSN: 0009-2665 (July 2018).

51. S. Xu, L. Zhang, B. Wang, R. S. Ruoff, *Cell Reports Physical Science* **2**, 100372, ISSN: 26663864 (Mar. 2021).

52. J. D. Albar *et al.*, *Scientific Reports* **7**, 6598, ISSN: 2045-2322 (Dec. 2017).

53. A. Summerfield *et al.*, *Scientific Reports* **6**, 22440, ISSN: 2045-2322 (Mar. 2016).

54. D. J. Finn *et al.*, *J. Mater. Chem. C* **2**, 925–932, ISSN: 2050-7526 (2014).

55. J. Phiri, P. Gane, T. C. Maloney, *Journal of Materials Science* **52**, 8321–8337, ISSN: 0022-2461 (July 2017).

56. Y. Xu, H. Cao, Y. Xue, B. Li, W. Cai, *Nanomaterials* **8**, 942, ISSN: 2079-4991 (Nov. 2018).

57. A. S. Mayorov *et al.*, *Nano Letters* **12**, 4629–4634, ISSN: 1530-6984 (Sept. 2012).

58. C. R. Dean *et al.*, *Nature Nanotechnology* **5**, 722–726, ISSN: 1748-3387 (Oct. 2010).

59. M. Ishigami, J. H. Chen, W. G. Cullen, M. S. Fuhrer, E. D. Williams, *Nano Letters* **7**, 1643–1648, ISSN: 1530-6984 (June 2007).

60. M. Katsnelson, A. Geim, *Philosophical Transactions of the Royal Society A: Mathematical, Physical and Engineering Sciences* **366**, 195–204, ISSN: 1364-503X (Jan. 2008).

61. N. Mishra, J. Boeckl, N. Motta, F. Iacopi, *physica status solidi (a)* **213**, 2277–2289, ISSN: 1862-6300 (Sept. 2016).

62. G. R. Yazdi *et al.*, *Carbon* **57**, 477–484, ISSN: 00086223 (June 2013).

63. J. L. Tedesco *et al.*, *Applied Physics Letters* **95**, 122102, ISSN: 0003-6951 (Sept. 2009).

64. E. Pallecchi *et al.*, *Scientific Reports* **4**, 4558, ISSN: 2045-2322 (May 2015).

65. A. Tzalenchuk *et al.*, *Nature Nanotechnology* **5**, 186–189, ISSN: 1748-3387 (Mar. 2010).

66. R. Ribeiro-Palau *et al.*, *Nature Nanotechnology* **10**, 965–971, ISSN: 1748-3387 (Nov. 2015).

67. C. Hill, *Partnership supports switch to energy efficient tech – Griffith News*, 2021, (`https://news.griffith.edu.au/2021/06/16/partnership-supports-switch-to-energy-efficient-tech/`).

68. A. Tyagi *et al.*, *Nanoscale* **14**, 2167–2176, ISSN: 2040-3372, (`https://pubs.rsc.org/en/content/articlehtml/2022/nr/d1nr05904a%20https://pubs.rsc.org/en/content/articlelanding/2022/nr/d1nr05904a`) (Feb. 2022).

69. T. Carey *et al.*, *Nature Communications 2017 8:1* **8**, 1–11, ISSN: 2041-1723, (`https://www.nature.com/articles/s41467-017-01210-2`) (Oct. 2017).

70. Graphenea, *CVD graphene*, (`https://www.graphenea.com/`).

71. Graphene Supermarket, *CVD graphene*, (`https://www.graphene-supermarket.com/`).

72. H. C. Lee *et al.*, *RSC Advances* **7**, 15644–15693, ISSN: 2046-2069 (2017).

73. M. Lotya, P. J. King, U. Khan, S. De, J. N. Coleman, *ACS Nano* **4**, 3155–3162, ISSN: 19360851, (`https://pubs.acs.org/doi/full/10.1021/nn1005304`) (June 2010).

74. X. Chen, J. F. Dobson, C. L. Raston, *Chemical Communications* **48**, 3703–3705, ISSN: 1364548X, (`https://pubs.rsc.org/en/content/articlehtml/2012/cc/c2cc17611d%20https://pubs.rsc.org/en/content/articlelanding/2012/cc/c2cc17611d`) (Mar. 2012).

75. K. R. Paton *et al.*, *Nature Materials 2014 13:6* **13**, 624–630, ISSN: 1476-4660, (`https://www.nature.com/articles/nmat3944`) (Apr. 2014).

76. P. G. Karagiannidis *et al.*, *ACS Nano* **11**, 2742–2755, ISSN: 1936086X, (`https://pubs.acs.org/doi/full/10.1021/acsnano.6b07735`) (Mar. 2017).

77. Sigma-Aldrich, *Graphene ink*, 2022, (`https://www.sigmaaldrich.com/GB/en/product/aldrich/793663`).

78. G. W. Mudd *et al.*, *Advanced Materials* **27**, 3760–3766, ISSN: 1521-4095, (`https://onlinelibrary.wiley.com/doi/full/10.1002/adma.201500889%20https://onlinelibrary.wiley.com/doi/abs/10.1002/adma.201500889%20https://onlinelibrary.wiley.com/doi/10.1002/adma.201500889`) (July 2015).

79. L. Turyanska *et al.*, *Advanced Electronic Materials* **1**, 1500062, ISSN: 2199-160X (July 2015).

80. A. Kojima, K. Teshima, Y. Shirai, T. Miyasaka, *Journal of the American Chemical Society* **131**, 6050–6051, ISSN: 0002-7863 (May 2009).

81. L. A. Frolova *et al.*, *The Journal of Physical Chemistry Letters* **11**, 6772–6778, ISSN: 1948-7185 (Aug. 2020).

82. M. Grätzel, *Nature Materials* **13**, 838–842, ISSN: 1476-1122 (Sept. 2014).

83. J. Y. Kim, J.-W. Lee, H. S. Jung, H. Shin, N.-G. Park, *Chemical Reviews* **120**, 7867–7918, ISSN: 0009-2665 (Aug. 2020).

84. J. Jeong *et al.*, *Nature* **592**, 381–385, ISSN: 0028-0836 (Apr. 2021).

85. T. Niu *et al.*, *Energy & Environmental Science* **11**, 3358–3366, ISSN: 1754-5692 (2018).

86. J.-P. Correa-Baena *et al.*, *Science* **358**, 739–744, ISSN: 0036-8075 (Nov. 2017).

87. NREL, *Photovoltaic Research*, (`https://www.nrel.gov/pv/cell-efficiency.html`).

88. E. J. Juarez-Perez *et al.*, *Journal of Materials Chemistry A* **6**, 9604–9612, ISSN: 2050-7488 (2018).

89. J. Bisquert, E. J. Juarez-Perez, *The Journal of Physical Chemistry Letters* **10**, 5889–5891, ISSN: 1948-7185 (Oct. 2019).

90. B. Conings *et al.*, *Advanced Energy Materials* **5**, 1500477, ISSN: 16146832 (Aug. 2015).

91. R. Wang *et al.*, *Advanced Functional Materials* **29**, 1808843, ISSN: 1616-301X (Nov. 2019).

92. J.-K. Wang, H.-Y. Hou, Y.-Q. Li, J.-X. Tang, *Nanoscale* **12**, 17149–17164, ISSN: 2040-3364 (2020).

93. Y. Wang *et al.*, *Science* **365**, 591–595, ISSN: 0036-8075 (Aug. 2019).

94. Q. Zhang, Y. Yin, *ACS Central Science* **4**, 668–679, ISSN: 2374-7943 (June 2018).

95. C. R. Kagan, L. C. Bassett, C. B. Murray, S. M. Thompson, *Chemical Reviews* **121**, 3186–3233, ISSN: 0009-2665, (`https://pubs.acs.org/doi/10.1021/acs.chemrev.0c00831`) (Mar. 2021).

96. M. Baranowski *et al.*, *Photonics Research* **8**, A50, ISSN: 2327-9125 (Oct. 2020).

97. M. Baranowski, P. Plochocka, *Advanced Energy Materials* **10**, 1903659, ISSN: 1614-6832 (July 2020).

98. F. Liu *et al.*, *ACS Nano* **11**, 10373–10383, ISSN: 1936-0851 (Oct. 2017).

99. P. Wang *et al.*, *Nature Communications* **9**, 2225, ISSN: 2041-1723 (Dec. 2018).

100. K. Lin *et al.*, *Nature* **562**, 245–248, ISSN: 0028-0836 (Oct. 2018).

101. Y. Wang, X. Li, V. Nalla, H. Zeng, H. Sun, *Advanced Functional Materials* **27**, 1605088, ISSN: 1616301X (Apr. 2017).

102. C. Bao *et al.*, *Advanced Materials* **30**, 1803422, ISSN: 09359648 (Sept. 2018).

103. J. Miao, F. Zhang, *Journal of Materials Chemistry C* **7**, 1741–1791, ISSN: 2050-7526 (2019).

104. H.-P. Wang *et al.*, *Advanced Materials* **33**, 2003309, ISSN: 1521-4095, (`https://onlinelibrary.wiley.com/doi/full/10.1002/adma.202003309%20https://onlinelibrary.wiley.com/doi/abs/10.1002/adma.202003309%20https://onlinelibrary.wiley.com/doi/10.1002/adma.202003309`) (Feb. 2021).

105. D. Yang, X. Li, H. Zeng, *Advanced Materials Interfaces* **5**, 1701662, ISSN: 2196-7350 (Apr. 2018).

106. B. T. Diroll, G. Nedelcu, M. V. Kovalenko, R. D. Schaller, *Advanced Functional Materials* **27**, 1606750, ISSN: 1616-301X, (`https://onlinelibrary.wiley.com/doi/abs/10.1002/adfm.201606750`) (2017).

107. K. Wei *et al.*, *Optics Letters* **41**, 3821, ISSN: 0146-9592 (Aug. 2016).

108. Q. Han, W. Wu, W. Liu, Q. Yang, Y. Yang, *Journal of Luminescence* **198**, 350–356 (2018).

109. S. M. Lee *et al.*, *The Journal of Physical Chemistry C* **121**, 26054–26062, ISSN: 1932-7447, (`https://doi.org/10.1021/acs.jpcc.7b06301`) (2017).

110. J. S. Manser, J. A. Christians, P. V. Kamat, *Chemical Reviews* **116**, 12956–13008, ISSN: 0009-2665 (Nov. 2016).

111. J. Kang, L.-W. Wang, *The Journal of Physical Chemistry Letters* **8**, 489–493, ISSN: 1948-7185 (Jan. 2017).

112. H. Zhang *et al.*, *Nat Commun* **10**, 1088, ISSN: 2041-1723 (Electronic) 2041-1723 (Linking), (`https://www.ncbi.nlm.nih.gov/pubmed/30842434`) (2019).

113. S. Draguta *et al.*, *Nat Commun* **8**, 200, ISSN: 2041-1723 (Electronic) 2041-1723 (Linking), (`https://www.ncbi.nlm.nih.gov/pubmed/28779144`) (2017).

114. D. W. deQuilettes *et al.*, *Nat Commun* **7**, 11683, ISSN: 2041-1723 (Electronic) 2041-1723 (Linking), (`https://www.ncbi.nlm.nih.gov/pubmed/27216703`) (2016).

115. Y. S. Park, S. Guo, N. S. Makarov, V. I. Klimov, *ACS Nano* **9**, 10386–10393, ISSN: 1936-086X (Electronic) 1936-0851 (Linking), (`https://www.ncbi.nlm.nih.gov/pubmed/26312994`) (2015).

116. L. Hou *et al.*, *Nanoscale* **12**, 6795–6802, ISSN: 2040-3372 (Electronic) 2040-3364 (Linking), (`https://www.ncbi.nlm.nih.gov/pubmed/32181469`) (2020).

117. D. K. Sharma, S. Hirata, V. Biju, M. Vacha, *ACS Nano* **13**, 624–632, ISSN: 1936-086X (Electronic) 1936-0851 (Linking), (`https://www.ncbi.nlm.nih.gov/pubmed/30616355`) (2019).

118. A. L. Efros, M. Rosen, *Physical Review Letters* **78**, 1110–1113, ISSN: 0031-9007 (Feb. 1997).

119. A. L. Efros, *Nature Materials* **7**, 612–613, ISSN: 1476-1122 (Aug. 2008).

120. N. D. Cottam *et al.*, *ACS Applied Electronic Materials* **2**, 147–154, (`https://doi.org/10.1021/acsaelm.9b00664`) (2020).

121. H. Huang, M. I. Bodnarchuk, S. V. Kershaw, M. V. Kovalenko, A. L. Rogach, *ACS Energy Letters* **2**, 2071–2083, (`https://doi.org/10.1021/acsenergylett.7b00547`) (2017).

122. Q. A. Akkerman, G. Raino, M. V. Kovalenko, L. Manna, *Nat Mater* **17**, 394–405, ISSN: 1476-1122 (Print) 1476-1122 (Linking), (`https://www.ncbi.nlm.nih.gov/pubmed/29459748`) (2018).

123. Thorlabs, *Photodiodes*, (`https://www.thorlabs.com/newgrouppage9.cfm?objectgroup_id=285`).

124. L. Mei *et al.*, *Advanced Optical Materials* **10**, 2102656, ISSN: 2195-1071 (May 2022).

125. Y. Li *et al.*, *Advanced Materials Interfaces* **6**, 1900188, ISSN: 2196-7350 (May 2019).

126. M. Furchi *et al.*, *Nano Letters* **12**, 2773–2777, ISSN: 1530-6984 (June 2012).

127. E. Monroy *et al.*, *Semiconductor Science and Technology* **13**, 1042–1046, ISSN: 0268-1242 (Sept. 1998).

128. R. Korde, J. Geist, *Applied Optics* **26**, 5284, ISSN: 0003-6935 (Dec. 1987).

129. A. Chaves *et al.*, *npj 2D Materials and Applications* **4**, 29, ISSN: 2397-7132 (Dec. 2020).

130. W. Yang *et al.*, *Advanced Functional Materials* **29**, 1808182, ISSN: 1616-301X (May 2019).

131. W. N. Ye, Y. Xiong, *Journal of Modern Optics* **60**, 1299–1320, ISSN: 0950-0340 (Sept. 2013).

132. F. E. Ejeckam *et al.*, *Applied Physics Letters* **67**, 3936–3938, ISSN: 0003-6951 (Dec. 1995).

133. P. Wang *et al.*, *Small* **15**, 1904396, ISSN: 1613-6810 (Nov. 2019).

134. M. Chhowalla *et al.*, *Nature Chemistry* **5**, 263–275, ISSN: 1755-4330 (Apr. 2013).

135. G. W. Mudd *et al.*, *Scientific Reports* **6**, 39619, ISSN: 2045-2322 (Dec. 2016).

136. C. R. Kagan, E. Lifshitz, E. H. Sargent, D. V. Talapin, *Science* **353**, ISSN: 0036-8075 (Aug. 2016).

137. J. Maes *et al.*, *The Journal of Physical Chemistry Letters* **9**, 3093–3097, ISSN: 1948-7185 (June 2018).

138. J. M. Dawlaty *et al.*, *Applied Physics Letters* **93**, 131905, ISSN: 0003-6951 (Sept. 2008).

139. A. R. Wright, J. C. Cao, C. Zhang, *Physical Review Letters* **103**, 207401, ISSN: 0031-9007 (Nov. 2009).

140. F. Xia, T. Mueller, Y.-m. Lin, A. Valdes-Garcia, P. Avouris, *Nature Nanotechnology* **4**, 839–843, ISSN: 1748-3387 (Dec. 2009).

141. F. H. L. Koppens *et al.*, *Nature Nanotechnology* **9**, 780–793, ISSN: 1748-3387 (Oct. 2014).

142. A. De Sanctis, J. D. Mehew, M. F. Craciun, S. Russo, *Materials 2018, Vol. 11, Page 1762* **11**, 1762, ISSN: 1996-1944, (https://www.mdpi.com/1996-1944/11/9/1762/htm%20https://www.mdpi.com/1996-1944/11/9/1762) (Sept. 2018).

143. Y. Liu, S. Zhang, J. He, Z. M. Wang, Z. Liu, *Nano-Micro Letters 2019 11:1* **11**, 1–24, ISSN: 2150-5551, (https://link.springer.com/article/10.1007/s40820-019-0245-5) (Feb. 2019).

144. A. C. Ferrari *et al.*, *Nanoscale* **7**, 4598–4810, ISSN: 2040-3364 (2015).

145. J. Cheng, C. Wang, X. Zou, L. Liao, *Advanced Optical Materials* **7**, 1800441, ISSN: 21951071 (Jan. 2019).

146. R. Saran, R. J. Curry, *Nature Photonics* **10**, 81–92, ISSN: 1749-4885 (Feb. 2016).

147. Y. Lee *et al.*, *Advanced Materials* **27**, 41–46, ISSN: 09359648 (Jan. 2015).

148. F. Mei *et al.*, *Advances in Physics: X* **4**, 1592709, ISSN: 2374-6149 (Jan. 2019).

149. A. M. Alamri, S. Leung, M. Vaseem, A. Shamim, J.-H. He, *IEEE Transactions on Electron Devices* **66**, 2657–2661, ISSN: 0018-9383 (June 2019).

150. C. Fang *et al.*, *ACS Applied Materials and Interfaces* **11**, 8419–8427, ISSN: 19448252 (Feb. 2019).

151. D.-H. Kwak, D.-H. Lim, H.-S. Ra, P. Ramasamy, J.-S. Lee, *RSC Advances* **6**, 65252–65256, ISSN: 2046-2069 (2016).

152. H. Fang, W. Hu, *Advanced Science* **4**, 1700323, ISSN: 21983844 (Dec. 2017).

153. C. Xie *et al.*, *Advanced Functional Materials* **29**, 1806006, ISSN: 1616301X (Feb. 2019).

154. P. E. Glaser, *Science* **162**, 857–861, ISSN: 0036-8075 (Nov. 1968).

155. H. Chen, K. Liu, L. Hu, A. A. Al-Ghamdi, X. Fang, *Materials Today* **18**, 493–502, ISSN: 13697021 (Nov. 2015).

156. M. Razeghi, A. Rogalski, *Journal of Applied Physics* **79**, 7433–7473, ISSN: 0021-8979 (May 1996).

157. A. Ahmad, T. Azam, in *Bottled and Packaged Water* (Elsevier, 2019), pp. 83–120.

158. J. M. Boyce, *Antimicrobial Resistance & Infection Control* **5**, 10, ISSN: 2047-2994 (Dec. 2016).

159. T. Oshima *et al.*, *Japanese Journal of Applied Physics* **48**, 011605, ISSN: 0021-4922 (Jan. 2009).

160. L. Su, W. Yang, J. Cai, H. Chen, X. Fang, *Small* **13**, 1701687, ISSN: 16136810 (Dec. 2017).

161. F. Omnès, E. Monroy, E. Muñoz, J.-L. Reverchon, presented at the, ed. by H. Morkoc, C. W. Litton, 64730E.

162. Edmund Optics, *UV enhanced silicon detector*, 2022, (`https://www.edmundoptics.co.uk/p/uv-enhanced-response-500mmsup2sup-silicon-%20detector/10741`).

163. OSI Optoelectronics, *UV enhanced photodiodes*, Mar. 2022, (`http://www.osioptoelectronics.com/standard-products/silicon-photodiodes/uv-%20enhanced-photodiodes/uv-enhanced-photodiodes-overview.aspx`).

164. A. Aldalbahi *et al.*, *Scientific Reports* **6**, 23457, ISSN: 2045-2322 (Mar. 2016).

165. E. Muñoz *et al.*, *Journal of Physics: Condensed Matter* **13**, 7115–7137, ISSN: 0953-8984 (Aug. 2001).

166. M. Razeghi, M. Henini, 575 (2004).

167. F. Luo *et al.*, *AIP Advances* **8**, 115106, ISSN: 2158-3226 (Nov. 2018).

168. R. Salh, in *Crystalline Silicon - Properties and Uses* (InTech, July 2011).

169. G. Imamura, K. Saiki, *ACS Applied Materials & Interfaces* **7**, 2439–2443, ISSN: 1944-8244 (Feb. 2015).

170. Z. Luo, N. J. Pinto, Y. Davila, A. T. Charlie Johnson, *Applied Physics Letters* **100**, 253108, ISSN: 0003-6951 (June 2012).

171. L. Britnell *et al.*, *Science* **335**, 947–950, ISSN: 0036-8075 (Feb. 2012).

172. A. Dey *et al.*, *2D Materials* **9**, 035003, ISSN: 2053-1583 (July 2022).

173. T. J. Janssen, A. Tzalenchuk, S. Lara-Avila, S. Kubatkin, V. I. Fal'Ko, *Reports on Progress in Physics* **76**, 104501, ISSN: 0034-4885, (`https://iopscience.iop.org/article/10.1088/0034-4885/76/10/104501%20https://iopscience.iop.org/article/10.1088/0034-4885/76/10/104501/meta`) (Oct. 2013).

174. K. v. Klitzing, G. Dorda, M. Pepper, *Physical Review Letters* **45**, 494–497, ISSN: 0031-9007 (Aug. 1980).

175. Graphenea, *GFET-S10 for sensing applications*, (`www.graphenea.com/products/gfet-s10-for-sensing-applications-10-mm-x-10-mm`).

176. Z. Kudrynskyi, D. Mazumder, N. Cottam, "Protocols for material processing and device fabrication", tech. rep.

177. R. R. Nair *et al.*, *Science* **320**, 1308–1308, ISSN: 0036-8075 (June 2008).

178. M. Buscema *et al.*, *Chemical Society Reviews* **44**, 3691–3718, ISSN: 0306-0012 (2015).

179. G. Konstantatos *et al.*, *Nature Nanotechnology* **7**, 363–368, ISSN: 1748-3387 (June 2012).

180. L. Turyanska, O. Makarovsky, L. Eaves, A. Patanè, N. Mori, *2D Materials* **4**, 025026, ISSN: 2053-1583 (Feb. 2017).

181. J. Mohrmann, K. Watanabe, T. Taniguchi, R. Danneau, *Nanotechnology* **26**, 015202, ISSN: 0957-4484 (Jan. 2015).

182. S. Goossens *et al.*, *Nature Photonics* **11**, 366–371, ISSN: 1749-4885 (June 2017).

183. S. Wan *et al.*, *Advanced Functional Materials* **29**, 1808606, ISSN: 1616-301X (May 2019).

184. Z. Yang *et al.*, *ACS Energy Letters* **2**, 1621–1627, ISSN: 23808195 (July 2017).

185. T. Zhang *et al.*, *Advanced Optical Materials* **6**, 1701341, ISSN: 21951071 (July 2018).

186. J. A. Alexander-Webber *et al.*, *Scientific Reports* **6**, 30296, ISSN: 2045-2322 (July 2016).

187. M. A. Bhuiyan *et al.*, *Advanced Functional Materials* **29**, 1805491, ISSN: 1616301X (Jan. 2019).

188. A. Surendran *et al.*, *ACS Applied Materials and Interfaces* **11**, 27064–27072, ISSN: 19448252 (July 2019).

189. N. D. Cottam *et al.*, *Advanced Optical Materials* **9**, ISSN: 21951071 (July 2021).

190. G. J. Wetzelaer *et al.*, *Adv Mater* **27**, 1837–1841, ISSN: 1521-4095 (Electronic) 0935-9648 (Linking), (https://www.ncbi.nlm.nih.gov/pubmed/25648930) (2015).

191. C. Giansante, I. Infante, *The Journal of Physical Chemistry Letters* **8**, 5209–5215, ISSN: 1948-7185 (Oct. 2017).

192. B. T. Diroll, H. Zhou, R. D. Schaller, *Advanced Functional Materials* **28**, 1800945, ISSN: 1616-301X (July 2018).

193. J. H. Gosling *et al.*, *Communications Physics* **4**, 30, ISSN: 2399-3650 (Dec. 2021).

194. J. De Roo *et al.*, *ACS Nano* **10**, 2071–2081, ISSN: 1936086X, (https://pubs.acs.org/doi/full/10.1021/acsnano.5b06295) (Feb. 2016).

195. Z. Ma *et al.*, *ACS Applied Nano Materials* **4**, 8383–8389, ISSN: 25740970, (https://pubs.acs.org/doi/full/10.1021/acsanm.1c01604) (Aug. 2021).

196. N. Yarita *et al.*, *Physical Review Materials* **2**, 116003, ISSN: 2475-9953 (Nov. 2018).

197. M. Nirmal *et al.*, *Nature* **383**, 802–804, ISSN: 0028-0836 (Oct. 1996).

198. A. L. Efros, D. J. Nesbitt, *Nat Nanotechnol* **11**, 661–671, ISSN: 1748-3395 (Electronic) 1748-3387 (Linking), (https://www.ncbi.nlm.nih.gov/pubmed/27485584) (2016).

199. N. A. Gibson, B. A. Koscher, A. P. Alivisatos, S. R. Leone, *The Journal of Physical Chemistry C* **122**, 12106–12113, ISSN: 1932-7447, (https://doi.org/10.1021/acs.jpcc.8b03206) (2018).

200. C. G. Bischak *et al.*, *Nano Lett* **17**, 1028–1033, ISSN: 1530-6992 (Electronic) 1530-6984 (Linking), (https://www.ncbi.nlm.nih.gov/pubmed/28134530) (2017).

201. D. J. Slotcavage, H. I. Karunadasa, M. D. McGehee, *ACS Energy Letters* **1**, 1199–1205, ISSN: 2380-8195 (Dec. 2016).

202. I. Karimata, Y. Kobori, T. Tachikawa, *The Journal of Physical Chemistry Letters* **8**, 1724–1728, ISSN: 1948-7185 (Apr. 2017).

203. G. Yuan *et al.*, *The Journal of Physical Chemistry C* **122**, 13407–13415, ISSN: 1932-7447 (June 2018).

204. R. Ahumada-Lazo *et al.*, *Journal of Physics: Photonics* **3**, 021002, ISSN: 2515-7647, (https://iopscience.iop.org/article/10.1088/2515-7647/abedd0%20https://iopscience.iop.org/article/10.1088/2515-7647/abedd0/meta) (Apr. 2021).

205. S. M. Menke, R. J. Holmes, *Energy & Environmental Science* **7**, 499–512, ISSN: 17545706, (https://pubs.rsc.org/en/content/articlehtml/2014/ee/c3ee42444h%20https://pubs.rsc.org/en/content/articlelanding/2014/ee/c3ee42444h) (Jan. 2014).

206. W. Zheng *et al.*, *Nature Communications 2018 9:1* **9**, 1–9, ISSN: 2041-1723, (https://www.nature.com/articles/s41467-018-05947-2) (Aug. 2018).

207. M. Zeng *et al.*, *Journal of Materials Chemistry C* **7**, 2014–2021, ISSN: 20507526, (https://pubs.rsc.org/en/content/articlehtml/2019/tc/c8tc06063k%20https://pubs.rsc.org/en/content/articlelanding/2019/tc/c8tc06063k) (Feb. 2019).

208. C. De Weerd *et al.*, *Journal of Physical Chemistry C* **120**, 13310–13315, ISSN: 19327455, (https://pubs.acs.org/doi/full/10.1021/acs.jpcc.6b04768) (June 2016).

209. G. Allan, C. Delerue, *Physical Review B - Condensed Matter and Materials Physics* **75**, 195311, ISSN: 10980121, (https://journals.aps.org/prb/abstract/10.1103/PhysRevB.75.195311) (May 2007).

210. K. Wei, X. Zheng, X. Cheng, C. Shen, T. Jiang, *Advanced Optical Materials* **4**, 1993–1997, ISSN: 2195-1071, (https://onlinelibrary.wiley.com/doi/full/10.1002/adom.201600352%20https://onlinelibrary.wiley.com/doi/abs/10.1002/adom.201600352%20https://onlinelibrary.wiley.com/doi/10.1002/adom.201600352) (Dec. 2016).

211. W. Escoffier, M. Gorian, M. Pierre, *LNCMI*, (http://lncmi.cnrs.fr/en/welcome/).

212. C. Coletti, V. Miseikis, *CNI@NEST*, (https://www.iit.it/web/center-for-nanotechnology-innovation).

213. Y. Huang, W. Luan, M. Liu, L. Turyanska, *Journal of Materials Chemistry C* **8**, 2381–2387, ISSN: 2050-7526 (2020).

214. O. Makarovsky *et al.*, *2D Materials* **4**, 031001, ISSN: 2053-1583, (https://iopscience.iop.org/article/10.1088/2053-1583/aa76bb%20https://iopscience.iop.org/article/10.1088/2053-1583/aa76bb/meta) (June 2017).

215. E. O. Filatova, A. S. Konashuk, *The Journal of Physical Chemistry C* **119**, 20755–20761, ISSN: 1932-7447 (Sept. 2015).

216. K. S. Novoselov *et al.*, *Science* **315**, 1379–1379, ISSN: 0036-8075 (Mar. 2007).

217. M. Yang *et al.*, *Physical Review Letters* **117**, 237702, ISSN: 0031-9007 (Dec. 2016).

218. J. N. Coleman *et al.*, *Science* **331**, 568–571, ISSN: 00368075, (`https://www.science.org/doi/full/10.1126/science.1194975`) (Feb. 2011).

219. J. N. Coleman, *Accounts of Chemical Research* **46**, 14–22, ISSN: 00014842, (`https://pubs.acs.org/doi/full/10.1021/ar300009f`) (Jan. 2013).

220. E. Jabari *et al.*, *2D Materials* **6**, 042004, ISSN: 2053-1583, (`https://iopscience.iop.org/article/10.1088/2053-1583/ab29b2%20https://iopscience.iop.org/article/10.1088/2053-1583/ab29b2/meta`) (Aug. 2019).

221. Y. S. Rim, S. H. Bae, H. Chen, N. De Marco, Y. Yang, *Advanced Materials* **28**, 4415–4440, ISSN: 1521-4095, (`https://onlinelibrary.wiley.com/doi/full/10.1002/adma.201505118%20https://onlinelibrary.wiley.com/doi/abs/10.1002/adma.201505118%20https://onlinelibrary.wiley.com/doi/10.1002/adma.201505118`) (June 2016).

222. H. Guo, R. Lv, S. Bai, *Nano Materials Science* **1**, 101–115, ISSN: 2589-9651 (June 2019).

223. B. Wang, A. Facchetti, B. Wang, A. Facchetti, *Advanced Materials* **31**, 1901408, ISSN: 1521-4095, (`https://onlinelibrary.wiley.com/doi/full/10.1002/adma.201901408%20https://onlinelibrary.wiley.com/doi/abs/10.1002/adma.201901408%20https://onlinelibrary.wiley.com/doi/10.1002/adma.201901408`) (July 2019).

224. Q. Zhang *et al.*, *Journal of Materials Chemistry C* **7**, 6795–6804, ISSN: 2050-7534, (`https://pubs.rsc.org/en/content/articlehtml/2019/tc/c9tc01012b%20https://pubs.rsc.org/en/content/articlelanding/2019/tc/c9tc01012b`) (June 2019).

225. F. Wang *et al.*, *Advanced Functional Materials* **31**, 2007478, ISSN: 1616-301X (Jan. 2021).

226. F. Torrisi *et al.*, *ACS Nano* **6**, 2992–3006, ISSN: 1936-0851 (Apr. 2012).

227. S. Barwich *et al.*, *Carbon* **171**, 306–319, ISSN: 00086223 (Jan. 2021).

228. M. Singh, H. M. Haverinen, P. Dhagat, G. E. Jabbour, *Advanced Materials* **22**, 673–685, ISSN: 09359648 (Feb. 2010).

229. A. G. Kelly *et al.*, *Science* **356**, 69–73, ISSN: 10959203, (`https://www.science.org/doi/full/10.1126/science.aal4062`) (Apr. 2017).

230. C. S. Lau, J. A. Mol, J. H. Warner, G. A. Briggs, *Physical Chemistry Chemical Physics* **16**, 20398–20401, ISSN: 14639076, (`https://pubs.rsc.org/en/content/articlehtml/2014/cp/c4cp03257h%20https://pubs.rsc.org/en/content/articlelanding/2014/cp/c4cp03257h`) (Sept. 2014).

231. K. Ullmann *et al.*, *Nano Letters* **15**, 3512–3518, ISSN: 15306992, (`https://pubs.acs.org/doi/full/10.1021/acs.nanolett.5b00877`) (May 2015).

232. S. Goniszewski *et al.*, *Scientific Reports 2016 6:1* **6**, 1–9, ISSN: 2045-2322, (https://www.nature.com/articles/srep22858) (Mar. 2016).

233. S. De, P. J. King, P. E. Lyons, U. Khan, J. N. Coleman, *ACS Nano* **4**, 7064–7072, ISSN: 1936-0851 (Dec. 2010).

234. Y.-W. Tan, Y. Zhang, H. L. Stormer, P. Kim, *The European Physical Journal Special Topics* **148**, 15–18, ISSN: 1951-6355 (Sept. 2007).

235. K. I. Bolotin, K. J. Sikes, J. Hone, H. L. Stormer, P. Kim, *Physical Review Letters* **101**, 096802, ISSN: 0031-9007 (Aug. 2008).

236. N. F. Mott, *Philosophical Magazine* **19**, 835–852, ISSN: 0031-8086 (Apr. 1969).

237. R. M. Hill, *Physica Status Solidi (a)* **34**, 601–613, ISSN: 00318965 (Apr. 1976).

238. E. McCann *et al.*, *Physical Review Letters* **97**, 146805, ISSN: 0031-9007 (Oct. 2006).

239. Y. Liu, W. S. Lew, L. Sun, *Physical Chemistry Chemical Physics* **13**, 20208–20214, ISSN: 14639076, (https://pubs.rsc.org/en/content/articlehtml/2011/cp/c1cp22250c%20https://pubs.rsc.org/en/content/articlelanding/2011/cp/c1cp22250c) (Nov. 2011).

240. G. Calabrese *et al.*, *Nanoscale* **12**, 6708–6716, ISSN: 2040-3364 (2020).

241. H. Cao *et al.*, *Applied Physics Letters* **96**, 122106, ISSN: 0003-6951 (Mar. 2010).

242. S. Pezzini, C. Cobaleda, E. Diez, V. Bellani, *Physical Review B* **85**, 165451, ISSN: 1098-0121 (Apr. 2012).

243. M. Hilke, M. Massicotte, E. Whiteway, V. Yu, *Scientific World Journal* **2014**, ISSN: 1537744X, (https://arxiv.org/abs/1212.5334v1) (Dec. 2012).

244. A. Maulu *et al.*, *Nanomaterials* **8**, 677, ISSN: 2079-4991 (Aug. 2018).

245. M. J. Grotevent *et al.*, *ACS Applied Materials and Interfaces* **13**, 848–856, ISSN: 19448252 (Jan. 2021).

246. Y.-T. Huang *et al.*, *ACS Applied Materials & Interfaces* **10**, 33450–33456, ISSN: 1944-8244 (Oct. 2018).

247. G. W. Mudd *et al.*, *Advanced Materials* **25**, 5714–5718, ISSN: 09359648 (Oct. 2013).